

FLUID-STRUCTURE INTERACTIONS AND ACTIVE  
CONTROL IN HIGH-PERFORMANCE THUNNIFORM  
SWIMMING

---

QIANG ZHONG

A DISSERTATION  
PRESENTED TO THE FACULTY  
OF UNIVERSITY OF VIRGINIA  
IN CANDIDACY FOR THE DEGREE  
OF DOCTOR OF PHILOSOPHY

RECOMMENDED FOR ACCEPTANCE  
BY THE DEPARTMENT OF  
MECHANICAL AND AEROSPACE ENGINEERING  
ADVISOR: DANIEL B. QUINN

University of Virginia

May 2021

Copyright © Qiang Zhong 2021

All rights reserved.

# Abstract

In terms of bulk swimming metrics such as speed, efficiency, maneuverability, and stealth, fishes vastly outperform man-made underwater vehicles. Motivated by this performance gap, this thesis uses both idealized models of propulsors and reduced order three-dimensional robotic platforms to distill the essential physics and design features of high performance swimming.

A unique wireless experimental system was developed at the beginning as the foundation of this thesis. This experimental system has the ability to perform automatic direct force measurements and dynamic position tracking, which creates a bridge between traditional tethered tests and autonomous platforms. The modularized design allows us to configure the experimental system with different hardware add-ons and software for various studies. Together with the newly developed Three-Dimensional Particle Image Velocimetry (3D PIV) system, this experimental system is able to couple hydrodynamic features with performance measurements, thereby offering a powerful tool for studies in this thesis.

When fishes/robots swim near the substrate or near each other, they introduce unsteady interactions with the boundary. Both dynamic position tracking and direct force measurements reveal that unsteady steady ground effect leads to asymmetric lift generation and a boost in thrust without efficiency loss. For the first time, we proved the existence of equilibrium altitudes. When close to the ground, the time-averaged lift is zero at certain altitudes and acts to return the foil to these equilibria. When the foil moves very close to the ground ( $d/c \leq 0.35$ ), there exists another unstable equilibrium altitude that pushes the foil

away from or towards the ground. In all cases, the stable equilibrium altitudes move higher with increasing Strouhal number, or with decreasing reduced frequency, but the unstable equilibrium altitudes are less sensitive. Increasing aspect ratio leads to stronger unsteady effects, including a stronger thrust boost, a larger asymmetric force, and a higher stable equilibrium altitude. The inviscid nature of these phenomena indicate that similar effects might exist when swimming near another out-of-phase swimmer.

Besides high efficiency steady swimming, fishes are highly maneuverable compared to man-made underwater vehicles. Maneuvers are inherently transient, so they are often studied via observations of fish and fish-like robots, where their dynamics cannot be recorded directly. In the case of the fish-inspired maneuver study, we present a set of experiments in which a semi-autonomous hydrofoil performs repeatable in-plane maneuvers in a water tunnel. We show that modulating the hydrofoil's frequency, amplitude, pitch bias, and stroke speed ratio produces streamwise and lateral maneuvers with mixed effectiveness. Our findings provide a framework for considering in-plane maneuvers and streamwise/lateral trajectory corrections in fish and fish-inspired robots.

Most fishes are equipped with multiple fins that can be used for manipulating unsteady three-dimensional interactions. In the case of multi-fin interactions during fish swimming, our study revealed the importance of dorsal fin shape on swimming performance enhancement and its role in multi-fin interactions. In particular, we used a tuna-inspired fish model with variable fin sharpness to study the interaction between elongated dorsal/anal fins and caudal fins. We found that the performance enhancement is stronger than previously thought (15% increase in swimming speed and 50% increase in swimming economy) and is governed by a three-dimensional dorsal-fin-induced cross-flow that lowers the angle of attack on the caudal fin and promotes spanwise flow. Both simulations and multi-layer particle image velocimetry reveal that the cross-flow stabilizes the leading edge vortex on the caudal fin, similar to how wing strakes prevent stall during fixed-wing aircraft maneuvers. Unlike other fin-fin interactions, this mechanism is phase-insensitive and offers a

simple, passive solution for flow control over oscillating propulsors.

Since flexible elements are widely present in fishes, it is reasonable to expect that flexibility might be relevant to their high swimming performance over a wide range of speeds. In the case of tail flexibility, we reveal one of the secrets of high fish efficiencies: tunable flexibility. Motivated by fish, who use muscles to modulate their stiffness, we derived a model that explains how and why tuning stiffness affects performance. We show that to maximize efficiency, muscle tension should scale with swimming speed squared, offering a simple tuning strategy for fish and fish-like robots. Tuning stiffness can double swimming efficiency at tuna-like frequencies and speeds (0-6 Hz; 0-2 body lengths/sec). Energy savings increase with frequency, suggesting that high-frequency fish and robots have the most to gain from tuning stiffness.

# Acknowledgements

First, I would like to thank my advisor, Daniel Quinn, for his advice and support over my years at the University of Virginia. Dan struck the perfect balance between guiding me to the right track and encouraging me to make my own movements, from which I benefited a lot. Dan stood by me through every challenge and choice, not only in research but also in life - and for that, I deeply consider him as a friend as much as a mentor. What I learned from Dan is far beyond research training and will benefit me during the rest of my life.

Next, I would like to thank the MURI team, and other ONR supported teams: Hilary Bart-Smith, Haibo Dong, George Lauder, Frank Fish, Lex Smits, Clancy Rowley, Keith Moored, and Melissa Green, whose helpful feedback and consistent insights shape my researches. Special thanks should go to Haibo Dong, who fueled my enthusiasm for bio-inspired studies. I also want to thank Jianzhong Zhu, he involved me in mantabot and tunabot studies. Moreover, I would like to thank my lab members and friends in FSRG that they made those years at UVa became one of my most precious memories.

Finally, I would like to thank my family. To my wife, Xiaoxue, it was her that lighted up my world and supported me in those darkest days. I might already get lost without her love and company. To my parents and grandparents, it was them that taught me to be curious about unknown things, to be brave when facing challenges, to be self-motivated when exploring alone. This thesis also belongs to them.

The work presented in this thesis was supported by the Office of Naval Research (N00014-14-1-0533, N00014-18-1-2537, and N00014-08-1-0642; Program Manager: R. Brizzolara), the National Science Foundation (1921809; Program Manager: Ron Joslin), and the University of Virginia.

# Contents

Abstract . . . . .	ii
Acknowledgements . . . . .	v
Nomenclature . . . . .	xxvii
<b>1 Introduction</b>	<b>1</b>
1.1 Motivation and Goals . . . . .	1
1.2 Boundary Interactions . . . . .	3
1.3 Fish Maneuver . . . . .	4
1.4 Multi-Fin Interactions . . . . .	5
1.5 Tail Flexibility . . . . .	7
1.6 Summary of Chapters and Contributions . . . . .	8
<b>2 Development of the Intelligent Experimental System</b>	<b>14</b>
2.1 Intelligent Experiment Apparatus . . . . .	15
2.1.1 Digital-Controlled Closed-loop Water Tunnel . . . . .	15
2.1.2 Two-axis Air Suspension System . . . . .	17
2.1.3 Low frequency ( $\leq 2.5$ Hz) Pitching Actuation Module . . . . .	18
2.1.4 Rotary-based High Frequency ( $\leq 7.0$ Hz) Actuation Module . . . . .	19
2.1.5 Tilting and Leveling System . . . . .	22
2.1.6 Carriage Electronics and Data Acquisition Method . . . . .	23
2.1.7 Control command Protocol . . . . .	24

2.2	Particle Image Velocimetry System . . . . .	27
2.2.1	Stereo Particle Image Velocimetry . . . . .	27
2.2.2	Three-dimensional scanning Particle Image Velocimetry . . . . .	27
2.3	Swimming Performance Measurement . . . . .	29
2.3.1	Drag Profile Measurements . . . . .	29
2.3.2	Force, Power, Efficiency, and Economy . . . . .	30
2.3.3	Performance Measurement System Validations . . . . .	31
2.4	Newton-Raphson based Free-Swimming Algorithm . . . . .	32
2.5	Summary and Configuration for Studies . . . . .	33
<b>3</b>	<b>Pitching Propulsor: Boundary Interactions</b>	<b>34</b>
3.1	Experiment Setup and Methods . . . . .	34
3.1.1	Constrained performance measurement of two-dimensional hydrofoil	34
3.1.2	Unconstrained dynamics measurement of two-dimensional hydrofoil	35
3.1.3	Constrained performance measurement of finite aspect ratio hydro- foils . . . . .	35
3.1.4	Simulating near-ground propulsion . . . . .	37
3.2	Results . . . . .	38
3.2.1	Near-ground performance of two-dimensional hydrofoil . . . . .	38
3.2.2	Near-ground performance of high-aspect-ratio hydrofoils . . . . .	42
3.2.3	Near-ground performance of low-aspect-ratio hydrofoils . . . . .	44
3.2.4	Comparing simulations and experiments . . . . .	47
3.2.5	Near-ground wakes of high- and low-aspect-ratio foils . . . . .	48
3.3	Discussion . . . . .	51
<b>4</b>	<b>Pitching Propulsor: Fish Inspired Maneuver</b>	<b>54</b>
4.0.1	A wireless carriage with a pitching hydrofoil . . . . .	54
4.0.2	Streamwise/lateral maneuvers . . . . .	56

4.0.3	Performance metrics and flow fields . . . . .	57
4.1	Results . . . . .	58
4.1.1	Bulk performance of streamwise maneuvers . . . . .	58
4.1.2	Instantaneous forces during streamwise maneuvers . . . . .	61
4.1.3	Bulk performance of lateral maneuvers . . . . .	62
4.1.4	Instantaneous forces during lateral maneuvers . . . . .	65
4.1.5	Wake structures behind lateral maneuvers . . . . .	66
4.2	Discussion . . . . .	69
<b>5</b>	<b>Tuna-Inspired Platform: Multi-fin Interactions</b>	<b>71</b>
5.1	Experimental setup and Methods . . . . .	71
5.1.1	Fish model design and construction . . . . .	71
5.1.2	Speed and economy measurements . . . . .	74
5.1.3	Immersed-boundary method simulations . . . . .	74
5.2	Results . . . . .	75
5.2.1	Sharpness affects swimming speed and economy . . . . .	75
5.2.2	Leading Edge Vortex is stabilized on the caudal fin . . . . .	77
5.2.3	Sharp dorsal fins create streamwise conical vortices . . . . .	80
5.3	Discussion . . . . .	81
<b>6</b>	<b>Tuna-Inspired Platform: Real-time Adjustable Flexibility</b>	<b>84</b>
6.1	Experiment setup and Methods . . . . .	84
6.1.1	Tuna-tail stiffness test . . . . .	84
6.1.2	Tuna-inspired platform with tunable stiffness tail . . . . .	85
6.1.3	Self-propelled swimming performance test . . . . .	88
6.1.4	Variable speed swimming mission test . . . . .	90
6.1.5	Modified Tunabot construction and experiment . . . . .	91
6.2	Mathematical modeling of robot fish with tunable stiffness tail . . . . .	93

6.2.1	Deriving the tail fin model . . . . .	93
6.2.2	Model predictions for free-swimming . . . . .	96
6.2.3	Model implications for efficiency . . . . .	98
6.3	Results . . . . .	100
6.3.1	Tuna tails inspire theory and experiments with tunable stiffness . . . . .	100
6.3.2	Maintaining high speed and efficiency with tunable stiffness . . . . .	101
6.3.3	Muscle/spring tension scale with swimming speed . . . . .	103
6.3.4	Nonlinear wakes at high stiffnesses . . . . .	106
6.3.5	Real-time stiffness tuning in variable speed swimming missions. . . . .	106
6.3.6	Tuning stiffness for high frequency fish and robots . . . . .	107
6.4	Discussion . . . . .	110
<b>7</b>	<b>Concluding Remarks and Future Work</b>	<b>112</b>
7.1	Boundary Interactions . . . . .	112
7.2	Fish-inspired Maneuvers . . . . .	114
7.3	Multi-fin Interactions . . . . .	115
7.4	Real-time Adjustable Flexibility . . . . .	116
7.5	Future Work . . . . .	117
	<b>References</b>	<b>119</b>
<b>A</b>	<b>Supplemental Data and figure of Multi-fin Interaction</b>	<b>132</b>
A.1	Dorsal fin stiffness scaling . . . . .	132
A.2	Supplemental Figures . . . . .	133
<b>B</b>	<b>Supplemental Data and figure of Real-time Adjustable Flexibility</b>	<b>136</b>

# List of Figures

2.1	<b>Experiment system hardware.</b> (a) The experiment apparatus sits on the top of the water tunnel. (b) bottom view of the two-axis air suspension system. (c) detailed view of the inner frame of the two-axis air suspension system. . . . .	15
2.2	<b>Diagram of low frequency pitching actuator</b> . . . . .	19
2.3	<b>High-frequency pitching actuator design.</b> (a) The actuator consists of three modules: frequency (red), amplitude (blue), and pitch bias (green). Together, the modules convert the rotary motion of a DC motor into pitching motions of the platform’s tail. (b) A detailed view of amplitude control. The distance between the shaft and the central axis of the eccentric wheel is adjusted by a smart servo. The slot converts the motion of the rotating pin into periodic heaving motions. (c) A detailed view of pitch bias control. A servo adjusts the neutral angle of the pitch bias module, thus giving an offset, $\theta_{\text{bias}}$ , to the pitch motions of the driveshaft. . . . .	20
2.4	<b>Communication layout of the experiment system</b> . . . . .	25
2.5	<b>System Diagram of Three-Dimensional PIV System</b> . . . . .	28
2.6	<b>Drag profile of <math>\mathcal{R} = 1.5</math> teardrop hydrofoil.</b> Fit line: $F_x = 0.53u^2 + 0.196$ , $R^2 = 0.99$ The constant coefficient was constrained at 0.198 because a 0.198 N pre-load force was attached during the test. . . . .	30

2.7	<p><b>Validating thrust/power measurements.</b> (a) The measured thrust coefficient agrees with published values. Thrust coefficient is defined as <math>C_T \equiv \overline{F_T}/0.5 \rho a u^2</math>, where <math>\rho</math> is water density and <math>a</math> is airfoil area (twice the span times chord). Frequency is scaled as it was in the previous study [7] to facilitate comparisons: the scaling constant <math>c_6 = 2.55</math>. Error bars show +/- one standard deviation, and the shaded band shows an envelope circumscribing the published values [7]. (b) The measured power coefficient also agrees with published values, particularly at lower frequencies. The reduced frequency is defined as <math>f^* = 2\pi f c/u</math>, where <math>c</math> is chord length, and the scaling constant <math>c_9 = 4.89</math>. . . . .</p>	31
3.1	<p><b>Experimental setup.</b> (a) Four different aspect ratios (<math>\mathcal{A}</math>) were tested. (b) The foils underwent pitch oscillations near a splitter plane (pitch amplitude <math>\theta_0</math>, ground proximity <math>d</math>, incoming flow speed, <math>u</math>). (c) A <math>z</math>-traverse raised and lowered the foils in a water channel to facilitate Particle Image Velocimetry. A baffle plane reduced the effect of surface waves. Insert: an automated <math>y</math>-traverse (“Fisherman System”) controlled ground proximity by using a detachable latch to shift the foil’s lateral position (<math>\pm 0.01</math> mm resolution). . . . .</p>	36
3.2	<p><b>Performance coefficients of two-dimensional hydrofoil:</b> (a) Lift coefficient as a function of the non-dimensional distance from the ground for <math>k = 1.02</math> and (b) equilibrium altitude as a function of the Strouhal number and reduced frequency. No data are shown in the regions colored with white. Experiment data took by [83] at the Lehigh University. . . . .</p>	39

3.3	<p><b>Time-varying ground distance as a function of time normalized by the period of motion, <math>T</math>, for <math>St = 0.3</math>.</b> Data from (a) experiments and (b) simulations (simulation data took by [83] at the Lehigh University). The line color from black to light grey represents three different initial conditions: <math>D^* = 0.25, 0.5</math>, and <math>0.75</math>. Three reduced frequency cases of <math>k = 0.5, 0.75</math>, and <math>1</math> are presented. . . . .</p>	40
3.4	<p><b>Time-varying ground distance as a function of normalized time for <math>k = 1</math>.</b> Data from (a) experiments and (b) simulations (simulation data took by [83] at the Lehigh University). The line color from black to light grey represents three different initial conditions: <math>D^* = 0.25, 0.5</math>, and <math>0.75</math>. Three Strouhal number cases of <math>St = 0.3, 0.4</math>, and <math>0.5</math> are presented. . . . .</p>	41
3.5	<p><b>Performance coefficients for <math>\mathcal{R} = 2.5</math> at <math>\theta_0 = 9^\circ</math>.</b> (a) Thrust coefficient (<math>C_T \equiv \overline{F_T}/(0.5\rho u^2 sc)</math>) peaks at high Strouhal numbers (<math>St</math>) and low ground distances (<math>d/c</math>). (b) Efficiency (<math>\eta</math>) peaks at intermediate <math>St</math> and shows little dependence on <math>d/c</math>. (c) Lift coefficient (<math>C_L \equiv \overline{F_L}/(0.5\rho u^2 sc)</math>) can be positive or negative, leading to equilibrium altitudes where <math>C_L = 0</math>. . . . .</p>	43
3.6	<p><b>Performance coefficients for <math>\mathcal{R} = 1, 1.5, 2, 2.5</math>.</b> (a,c) Thrust coefficient (a) and efficiency (c) show similar trends as aspect ratio decreases, with a slight decrease at higher pitch amplitudes and lower aspect ratios. (e) Lift coefficient (<math>C_L</math>) shows changing trends as aspect ratio decreases: positive lift values and equilibrium altitudes decrease in magnitude. (f) (b,d,f) The performance coefficients for each <math>d/c</math> and <math>\mathcal{R}</math> combination, averaged across all <math>St</math> and <math>\theta_0</math> cases, reveal the dominant effects of changing aspect ratio. Ground proximities with only partial amplitudes were omitted in bulk averaging to make fair comparison. . . . .</p>	45

- 3.7 **Near-ground unsteady equilibria are less sensitive to aspect ratio than stable equilibria.**(a) Aspect ratio affects the location and magnitude of maximum lift, but it has little effect on the unsteady equilibrium altitude. (b) For a fixed Strouhal number, the unsteady equilibrium altitude slightly increases with larger amplitude. (c) For a fixed amplitude, the unsteady equilibrium altitude slightly increases with larger Strouhal number. . . . . 47
- 3.8 **Comparison between experiment and potential flow simulation.**(a) Both experiments and simulations show that stable equilibrium altitude increases with aspect ratio. No equilibria were found for the lowest aspect ratio cases at the Strouhal numbers of the simulations (0.25 and 0.35).(b) Relative change of time-averaged thrust coefficients ( $\Delta C_T$ ) at  $St = 0.35$ ,  $\theta_0 = 15^\circ$ . (c) Relative change of time-averaged efficiency ( $\Delta\eta$ ) at  $St = 0.35$ ,  $\theta_0 = 15^\circ$ . 48
- 3.9 **Aspect ratio affects wake topology near the ground.** Wakes from experiments (a-d) and simulations (e-h) are shown at the same phase (trailing edge closest to the ground). Wake structures are visualized with iso-surfaces of  $Q$ -criterion ( $Q = 5 s^{-2}$ ) colored by spanwise vorticity ( $\omega_z$ ). Sideplots show spanwise vorticity at a mid-span slice of the 3D wake. (a,b) Experiments:  $\mathcal{R} = 2$  hydrofoil far from and near to the ground. (c,d) Experiments:  $\mathcal{R} = 1$  hydrofoil far from and near to the ground. (e,f) Simulations:  $\mathcal{R} = 2$  hydrofoil far from and near to the ground. (g,h) Simulations:  $\mathcal{R} = 1$  hydrofoil far from and near to the ground. . . . . 49

3.10	<b>Low aspect ratio foils can more easily reach high-thrust regions.</b> Sample case shown is $St = 0.5$ and $\theta_0 = 9^\circ$ . Fish avatars: Manta ray $\mathcal{R} \approx 2.3$ [100] and Atlantic stingray $\mathcal{R} \approx 1.0$ [29]. Shaded regions denote the presence of a downward force towards a stable equilibrium (green), an upward force towards a stable equilibrium (yellow), or a downward force towards the ground (red), with color intensity meant to suggest the difficulty of maintaining a steady ground proximity. . . . .	53
4.1	<b>A wireless experimental rig for studying bio-inspired maneuvers.</b> (a) A carriage gliding on air bushings suspended a hydrofoil into the center of a water channel. Four stepper motors (z-traverses) auto-level the carriage frame. (b) Six air bushings provide the carriage with streamwise (s) and lateral (l) freedom. (c) Pitching motions are generated by a servo motor; driveshaft dynamics are recorded by a force/torque sensor and encoder. (d) The carriage reset system uses a linear actuator and a servo-driven gripper to reset the carriage in between trials. (e) Visualization of a maneuver test trial. Each step was performed automatically by an online control PC. . . .	58
4.2	<b>Bulk performance of streamwise maneuvers.</b> (a) Pitching motion profiles. (b) Displacement in the s-l plane after the 10-cycle maneuver. (c) Time-history of streamwise displacement during the maneuver. Light lines: raw data; dark lines: fitted parabolas. (d) Streamwise force peak magnitudes. (e) Lateral force peak magnitudes. . . . .	59
4.3	<b>Intracycle dynamics of streamwise maneuvers.</b> Curves and shaded bands represent the mean and standard deviation across five trials of the 5th pitching cycle of the maneuver. (a) Pitching motion profiles. (b) Streamwise displacement. (c) Streamwise force coefficient. (d) Lateral displacement. (e) Lateral force coefficient. . . . .	61

4.4	<b>Bulk performance of streamwise maneuvers.</b>	(a) Pitching motion profiles. (b) Displacement in the x-y plane after the 10-cycle maneuver. (c) Time-history of streamwise displacement during the maneuver. Light lines: raw data; dark lines: fitted parabolas. (d) Streamwise force peak magnitudes. (e) Lateral force peak magnitudes. . . . .	63
4.5	<b>Intracycle dynamics of lateral maneuvers.</b>	Curves and shaded bands represent the mean and standard deviation across five trials of the 5th pitching cycle of the maneuver. (a) Pitching motion profiles. (b) Streamwise displacement. (c) Streamwise force coefficient. (d) Lateral displacement. (e) Lateral force coefficient. . . . .	65
4.6	<b>Flow field during lateral maneuver.</b>	(a) Baseline kinematics. (b) representative spatial asymmetry case ( $\theta_{bias} = 3^\circ$ ). (c) Representative temporal asymmetry case ( $\beta = 0.75$ ). In all cases, incoming flow speed was subtracted from the velocity fields. First row: phase = $\pi$ ; second row: phase = $2\pi$ . . . . .	67
4.7	<b>Flow field comparison between zebrafish turning and temporally asymmetric pitching.</b>	(a) Time sequence of the flow field as zebrafish perform a yaw maneuver. Incoming flow speed was subtracted from the velocity fields. Body based $Re = 2500 \pm 700$ . Time between snapshots: 1/32 s. Replotted with permission from [104]. (b) Time sequence of the flow field around the temporal asymmetric hydrofoil ( $\beta = 0.75$ ). Incoming flow speed was subtracted from the velocity fields. Chord based $Re = 28500$ . Bottom row: yaw torque ( $\tau_z$ ) as a function of phase; red dot indicates phase of PIV. . . . .	68

5.1 **A reduced-order fish model was based on data from live tuna.** (a) Bluefin tuna and Crevalle jack reconstructions from [59]. (b) Reduced-order model used in this study (lengths in mm). The highlighted cross sections (F-F' and D-D') are shown in (c), and cross section D-D' is used to define sharpness. (c) Sharpness ( $\sigma \equiv 1 - \frac{OC}{OE}$ ) varied from 0 to 1 between the five models (M1 to M5). Solid lines show the cross-sections of the body plus fin for each model, while dotted lines show the base ellipse (semi-axes OA and OB) and the Bezier curve (end points B and D, control point C) used to define the cross section.  $OA = 0.97$  cm,  $OB = 0.74$  cm,  $OD = 1.73$  cm. . . . . 72

5.2 **Swimming speed increases with sharpness, while economy peaks for M4.** (a) A servo motor actuated the back half of the model (the “body”), and an encoder and F/T sensor recorded angular displacement and  $z$ -torques. PIV planes 1-5 are used to investigate flow features in Figure 3. Self-propelled swimming speed increases linearly with frequency for each model. (c) Compared to M1, self-propelled speed increases from M1 to M4, but shows no noticeable difference between M4 and M5.(d) Propulsive economy,  $\xi \equiv u/\bar{p}$ , decreases with frequency for each model. (e) Compared to M1, economy increases from M1 to M4, then decreases from M4 to M5. See Appendix. A for cycle-averaged power plots. . . . . 75

5.3 **Both PIV and simulations reveal a more stable Leading Edge Vortex (LEV) on the caudal fin. Results are shown at self-propelled swimming for M1 (a,b,c) and M4 (d,e,f) at three times in the flapping cycle  $T$ :  $t = 0.1T, 0.3T$ , and  $0.4T$ ). (a,d) Nine stacked layers of phase-averaged  $z$ -vorticity show how the LEV separates from the caudal fin around  $t = 0.3T$ . (b,e) The third vorticity contour from the top (Layer 3), shows the separation event in more detail. In the case of M4, the sharp dorsal fin induces a crossflow (DFC) which stabilizes the LEV on the caudal fin. The dotted triangular and rectangular regions are used for averaging flow speeds in Figure 4. (c,f) Simulated  $z$ -vorticity contours are shown at the same time steps. The simulations show a more stable flow on the caudal fin in M4, but the effect is less pronounced than in the experiments. See Appendix. A for PIV around M1\* . . . . . 78**

5.4 **Dorsal Fin-induced Crossflow (DFC) increases with fin sharpness, while flow attachment on the caudal fin peaks at M4. (a) DFC is quantified by the average flow speed ( $\overline{|v|}$ ) in the triangular region in Figure 5.3 3b,e ( $t = 0.3T$ ). To facilitate a fair comparison across models, speed was normalized by  $fA$ . Filled symbols, PIV; empty symbols, simulations. (b) The stabilization of the flow on the caudal fin was quantified by the average flow speed in the rectangular region in Fig 3b,e ( $t = 0.4T$ ). Flow attachment increases from M1 to M4 but shows no further increase from M4 to M5. . . . . 79**

5.5	<p><b>Long, thin, conical vortices are shed from sharp dorsal fins, causing a lateral crossflow towards the caudal fin.</b> Flows were visualized by mapping streamlines from the simulation results on M1 (<i>a</i>) and M4 (<i>b</i>) at <math>t = 0.4T</math>. In M4, streamlines seeded on the dorsal side of the body (25 uniformly seeded on the dorsal fin), colored by the <math>\lambda_2</math> criterion, are wound into tightly-packed vortices that move downstream and over the caudal fin. Streamlines seeded upstream (50 seeded upstream of the head), colored in light gray, show how these vortices induce a flow toward and along the caudal fin in M4 but not in M1. (<i>c</i>) Wing strake vortices (orange) shown passing over the main wing (schematic adapted from [117]) (<i>d</i>) Dye injection reveals strake vortices promoting flow attachment over an F-16A model in a water channel. Angle of attack, 15. Reynolds number, 15,000. Reprinted with permission from [117]. . . . .</p>	81
6.1	<p><b>Tuna-inspired reduced-order platform with adjustable stiffness tail joint.</b>(<i>a,b</i>) Side and top views of the reduced-order tuna-inspired platform (lengths in mm). (<i>c</i>) Rendering of the 3D model with the tail made transparent to reveal internal structures. The head is fixed by a carbon fiber shaft (6.35 mm diameter), and the tail is driven by a rotating carbon fiber drive shaft (12.7 mm diameter). Insert: a midsize servo installed inside the tail adjusts the effective torsional stiffness of the tail joint. (<i>d</i>) Diagram of tail joint that convert muscle tension to joint stiffness. <math>\ell_H = 11.6</math> mm , <math>\ell_J = 15</math> mm. . . .</p>	86

6.2	<b>Tunabot with modified tail joint design.</b>	(a) Original Tunabot design. A pair of elastic bands gave a constant stiffness to the tail joint. The maximum tail fin pitch angle was constrained to $\pm 15^\circ$ by a mechanical stop. (b) Our modified design uses a leaf spring to connect the tail joint to the tail fin. We changed the thickness of the leaf spring (1095 spring steel) to adjust the fixed stiffness of the joint. (c) The modified design had no mechanical stop (max tail fin pitch angle of $\pm 72^\circ$ ). . . . .	92
6.3	<b>A tail with tunable stiffness was modeled after tuna.</b>	(a) In tuna tails, paired lateral tendons connect anterior body muscles to rays of the caudal fin. (b) Simplified model: The tail is pitched back and forth at an angle $\theta_T$ , and the tail fin responds passively. (c) In our platform, a servo tightened a spring to adjust tail stiffness. The robot's head was fixed while its tail was pitched by a driveshaft. (d) A dissected tuna tail (see Supp. Figure. B.1 for other tails, $N = 6$ ) exhibited behaviors of a tuned torsional spring. When a force ( $T_M$ ) was applied to the lateral tendons, the restoring torque of the peduncle rose faster with fin pitch angle ( $\theta_F$ ). (e-f) The model and robotic tail also behave like tuned springs (1-parameter fit to match tuna tail see section 6.1.2). (g) A Scotch-yoke mechanism adjusted the frequency, amplitude, and pitch-bias of the driveshaft. An absolute encoder and a torque sensor recorded mechanical power input. (h) The platform was suspended in a recirculating water channel ( $W: 380 \text{ mm} \times H: 450 \text{ mm} \times L: 1520 \text{ mm}$ ) and could float in a horizontal plane due to a two-axis air bushing system. . . . .	102

- 6.4 **Swimming speed and efficiency depend on muscle tension and tailbeat frequency.** (a) Speed is maximized when both frequency and muscle tension are high (contour plot interpolated from 841 points). Insert: if muscle tension stays constant ( $T_M = 1.9$  N), stride length declines at high frequencies. Model is matched to experiment with a 1-parameter fit for tail fin thrust coefficient ( $C_T = 2.4$ ; see section 6.2.1). (b) Efficiency is maximized when muscle tension is tuned for a specific frequency. Ideal tension at  $f = 6$  Hz: 8.7 N (Model),  $7 \pm 0.3$  N (Experiment, ♦) Insert: if muscle tension stays constant, efficiency peaks at an intermediate frequency. . . . . 103
- 6.5 **Dimensional analysis and flow visualization reveal dynamics that govern optimal muscle/spring tension.** (a) Our model (black line) predicts that the scaled muscle tension ( $\tau$ ) determines the stride length ( $S$ ) and thus the efficiency (see section 6.2.2). Experimental data (colored circles) support these predictions. Model is matched to experiment with a 1-parameter fit for thrust coefficient ( $C_T = 2.4$ ; see section 6.2.1). Shaded gray band shows the sensitivity of the fit ( $C_T \pm 50\%$ ). (b) Three values of  $\tau$  highlight differences in kinematics: “too soft” ( $\tau = 1.88$ ), “ideal” ( $\tau = 2.68$ ), and “too stiff” ( $\tau = 3.96$ ) ( $f = 5$  Hz;  $T_M = 1.6, 5.3,$  and  $10.6$  N). Tail fin traces illustrate how the phase relationships maximize amplitude in the ideal case. (c) Increasing stiffness leads to higher angles of attack and a stronger, more detached Leading-Edge Vortex (LEV).  $Q$ -criterion isosurfaces are colored by dorsoventral vorticity ( $\omega_z$ ). Inserts: top view of one slice at the tail fin’s quarter span. . . . . 105

6.6	<b>Tuning stiffness saved energy across all missions.</b> (a) The platform used closed-loop control to stay on its goal path (on-board PD controller in a Micro Controller Unit (MCU)). (b) Tuning stiffness let the platform finish its mission faster. In the loose and rigid cases, speed plateaus during the mission. (c) Fixing stiffness led to inefficient mission segments. Only by tuning stiffness could the robotic tail maximize efficiency throughout the mission. (d) Tuning stiffness led to less energy drain in all four missions. Storage capacity of a AAA battery ( $\approx 6$ kJ) shown for reference. . . . .	108
6.7	<b>Tunable stiffness is most beneficial for high frequency fish and robots.</b> (a) Our model predicts that the benefits of tuning stiffness increase with frequency range, so long as muscles are strong enough to reach the optimal stiffnesses. Existing fish-like robots ( $\bullet$ ) are clustered at low servo-limited frequencies. In high-frequency fish ( $\bullet$ ), platforms like ours ( $\blacklozenge$ ), or robots like the Tunabot ( $\blacktriangle$ ), tuning stiffness improves efficiency by closer to 20%. Avatar descriptions in Table.B.2 (b) With fixed stiffness, the Tunabot shows nonlinear speed-frequency and efficiency-frequency dependences that are similar to those of our platform (Figure. 6.4a-b). . . . .	109
A.1	<b>Dorsal fin deflection is not measurably different between M1, M4, and M5.</b> High speed images taken at the same time ( $t = 0.25\tau$ ) and the same frequency ( $f = 1.57$ Hz) show no observable differences in dorsal fin bending.	133
A.2	<b>For self-propelled swimming, cycle-averaged power consumption decreases with sharpness until M4.</b> (a) Cycle-averaged power consumption increases with frequency for each model. (b) Compared to M1, cycle-averaged power consumption decreases from M1 to M4, then slightly increases from M4 to M5. . . . .	134
A.3	<b>PIV around M1* shows similar wake structures as PIV around M1 (Figure 5.3a,b).</b> . . . . .	134

- A.4 **Dorsal-caudal fin interaction is phase insensitive.** (a) Top view of half-cycle time-lapsed kinematics of three phase lags considered (72,108,144). (b) The ratio of M4 thrust to M1 thrust ( $\overline{F}_cM4/\overline{F}_cM1$ ) is mostly greater than 1 over the range of phase lags tested. Decreasing the phase from its natural value (126) would require a stiffer tail joint; increasing the phase would require an actively controlled tail joint. . . . . 135
- A.5 **The effective angle of attack of the caudal fin is lower in M4 than in M1 for most of the pitching cycle.** (a,b) Dorsal Fin-induced Crossflow (DFC) decreases the effective angle of attack of the caudal fin at the mid-stroke and increases the effective angle of attack at stroke transition. (c) The effective angle of attack for M1 and M4 is shown through the full pitching cycle. Layer 3 (Figure 5.3b,e) was chosen to approximate the effective angle of attack of the caudal fin. The average speed of crossflow was computed based on Region 1 (Figure 5.3b,e) translated with the body. Angle uncertainty was estimated based on variability in the PIV vectors of Region 1. The geometric angle of attack was calculated using high speed video. Effective angle of attack was calculated as the angle of the effective incoming flow velocity ( $u_{\text{eff}}$ ), which was calculated using vector addition as follows. (a). M1 midstroke:  $\alpha_{\text{eff}} = \tan^{-1}(\pi fa)/u - (25 \pm 2) = 41 \pm 2$ . M4 midstroke:  $\alpha_{\text{eff}} = \tan^{-1}((\pi fa - (0.63 \pm 0.08)fa \sin(55 \pm 5))/(u + (0.63 \pm 0.08)fa \cos(55 \pm 5))) - (25 \pm 2) = 32 \pm 4$ . (b). M1 at stroke transition:  $\alpha_{\text{eff}} = 12 \pm 2$ . M4 at stroke transition:  $\alpha_{\text{eff}} = \tan^{-1}((0.6 \pm 0.07)fa \sin(56 \pm 4)/(u + (0.6 \pm 0.07)fa \cos(56 \pm 4))) + (12 \pm 2) = 28 \pm 4$ . 135

**B.1 Tuna tail joint stiffness measurement.**(a) Tuna tails were installed on the test rig. Two sets of weights applied the force on the tendons ( $T_M$ ) and the simulated tail fin load ( $F_C$ ). (b) A laser distance sensor measured the deflection ( $d$ ) of the tail fin under various loads. (c) The custom laser distance unit consisted of a laser distance sensor (Baumer CH-8501 OADM 20L6441/S14F), an onboard Micro Controller Unit (MCU), a DC power input, and a LED display. (d) The peduncle area of the tuna tails was dissected to expose the axial tendons on which loads were applied. (e) Six different tails showed similar trend: the applied torque / area and the pitch angle showed a monotonic relation, and the slope of the relation increased with increasing tendon tension. See Tab. S1 for details. . . . . 137

**B.2 Test trial structure.** Each test trial consists of five procedures: 10 s of standby, 5 s of warm-up cycles, 20 cycles of data acquisition, 5 of cool down cycles, then a slow return to the neutral pitching position. . . . . 138

**B.3 Test trial structure.** Variable definitions for estimating power delivered by the scotch yoke mechanism. . . . . 138

**B.4 Overview of the experimental rig and system layout** (a) Our water channel rig consists of a pitching actuator, inner carriage, an outer frame, and a z-axis leveling system. The pitching actuator (Figure.2.3) is installed on the bottom of the inner carriage, which rides on a two-axis air-bushing system supporting by the outer frame. A baffle plate on the water surface minimizes water waves. (b) Air bushings allow the inner carriage to float in a horizontal plane. The x (streamwise) and y (lateral) position of the inner carriage were recorded by laser distance sensors. (c) System layout. The dashed line means wireless communication and the solid line means wired communication. . . . . 139

**B.5 Variable-speed untethered missions.** (a) A microcontroller (MCU3) tuned tail stiffness and maintained speed by modulating frequency with a PD controller. (b) Stiffness was either tuned based on frequency (following the blue curve) or fixed at “low”, “medium”, and “high” values. (c) Speed profiles during the Missions. The low and medium stiffness cases are unable to reach the maximum speed (d) Partial trajectories of the lateral position versus pitching cycles for the four Missions. (e) Efficiency versus swimming speed for the four Missions and four stiffness cases. In general, tuning stiffness led to the highest efficiency. The differences became smaller when the amplitude was increased in mission 4. (f) Simulated battery drain versus swimming distance. . . . . 140

**B.6 Wake structures at low frequencies.**Stiffness value remains constant while the frequency decreases from A to C. (a) Too loose case at high frequency ( $f = 5.0$  Hz). (b) Ideal stiffness at low frequency ( $f = 3$  Hz) leads to similar wake structure to ideal case at high frequency in Figure. 6.5 (c) Too stiff case at low frequency ( $f = 1.5$  Hz). . . . . 141

**B.7 Measured force and power of PIV cases at high frequency.**(a) Ideal stiffness results in favorable phase offset ( $90^\circ \pm 5^\circ$ ), while sufficient stiffness increases phase offset and over stiffness decreases offset. (b) Thrust changes were mainly dominated by axial force component, while suitable phase offset minimized the drag (negative thrust). (c) The magnitude of lift force stays at similar scale, but the phase of lift peak delays as stiffness increases. (d) The magnitude of power increases as stiffness increases. . . . . 141

# List of Tables

1.1	A summary of the major conclusions stated and discussed throughout the thesis with references to the section where the corresponding evidence is located. Part I . . . . .	12
1.2	A summary of the major conclusions stated and discussed throughout the thesis with references to the section where corresponding evidence locates. Part II. . . . .	13
2.1	Mini40 force/torque sensor calibration. . . . .	19
2.2	Input voltage specifications of carriage electronics. . . . .	24
2.3	Sensor output voltage regulation and amplification. . . . .	24
2.4	Example of concatenated string command sent to carriage. . . . .	24
2.5	Example of concatenated string with fixed length sent to carriage. . . . .	26
4.1	Maneuver test parameter specifications. . . . .	55
B.1	Tuna stiffness test specifications . . . . .	136
B.2	Avatar definitions from Fig. 5 . . . . .	142
B.3	Stiffness values used in Fig.3, Fig.4 and Fig.5 . . . . .	143

# Nomenclature

$\xi_{Mi}$	free-swimming economy of the $i$ 'th fin type model
$\mathcal{R}$	Aspect ratio
$\beta$	stroke speed ratio
$\ddot{\phantom{x}}$	Denotes the second time-derivative
$\Delta d_{tip}$	Measured displacement of the tail fin's centerline distal tip
$\delta$	Boundary layer thickness
$\dot{\theta}_{\max}$	Peak value of pitching velocity
$\dot{\phantom{x}}$	Denotes the first time-derivative
$\ell$	Full body length
$\ell_H$	Length of the extension of platform tail fin connector
$\ell_J$	Distance from platform's tail fin connector pitching axis to end of the peduncle.
$\ell_P$	Distance from the slot to the output driveshaft
$\ell_{laser}$	Perpendicular distance from the applied load to the tail fin mount axis
$\eta$	Swimming efficiency of tethered swimming ( $\equiv \overline{F_T u} / \overline{p}$ )

$\gamma$	A rescaled version of $\zeta$ introduced for notational convenience( $\sqrt{\zeta/(\rho\bar{\ell}_F^2/2)}$ )
$\bar{\ell}_F$	Tail fin length
-	Denotes a time-averaged quantity
$\phi$	Heave-pitch phase-offset of the tail fin
$\phi'$	Perturbation potential in an inertial frame fixed to the undisturbed fluid
$\rho$	Density of fluid
$\sigma$	The "sharpness" of the dorsal fin
$\tau$	The scaled muscle/spring tension
$\theta_F$	Tail fin pitch angle
$\theta_T(t)$	Output pitching motion of the high-frequency pitch actuator
$\theta_0$	Pitch amplitude
$\theta_{bias}$	Pitch bias
$\vec{F}_{pin}$	Force on the eccentric pin
$\vec{M}_{motor}$	Torque/moment on the motor
$\vec{r}_{pin}$	Vector from the DC motor's axis of rotation to the pin
$\xi$	Platform's swimming economy; High frequency actuator: $\xi \equiv u/\bar{p}_{motor}$ ; Low frequency actuator: $\xi \equiv u/\bar{p}$
$\zeta$	Approximate conversion constant that converts muscle tension to joint stiffness.
$A$	Peak to peak distance of flapping motion ( $\equiv 2\sin(\theta_0)c$ )
$A^*$	Non-dimensional amplitudes ( $\equiv A/c$ )

$a_{TE}$	Tip-to-tip amplitude of the tail fin's trailing edge
$c$	Chord length
$C_D$	Drag coefficient
$C_L$	Lift coefficient
$C_T$	Thrust coefficient
$C_{def}$	Theodorsen Lift Deficiency Function.
$C_V$	Motor frequency-voltage constant
$C_\tau$	Motor torque-current constant
$d$	Distance between the leading edge of the propulsor and the ground
$D^*$	Non-dimensional distance from the ground ( $\equiv d/c$ )
$D_0^*$	Non-dimensional initial distance from the ground
$D_{eq}^*$	Non-dimensional equilibrium altitude
$D_{head}$	Drag on the platform's head
$d_{pivot}$	Distance from eccentric pin to the axis of the DC motor
$D_{wholebody}$	Drag on the whole platform
$F$	Complex function of the prescribed motions
$f$	Tail-beat frequency
$F_L$	Force on the lateral direction of the water channel
$F_S$	Force on the streamwise direction of the water channel
$F_T$	Net thrust of platform/propulsor

$F_x$	Sensor $x$ axis force
$F_y$	Sensor $y$ axis force
$F_z$	Sensor $z$ axis force
$F_C$	Lateral force on the biological tail fin
$f_{g,1}$	First gravity wave harmonic frequency
$H$	Scaled heave position
$h(t)$	Prescribed heaving motion of the tail fin's leading edge
$h_0$	Heaving amplitude in Garrick model
$I$	Motor current
$I_0$	Motor no-load current
$J_0$	Zeroeth Bessel function of the first kind
$J_1$	first-order Bessel function of the first kind
$k$	Reduced frequency ( $\equiv fc/u$ )
$ks$	Linear spring coefficient
$l_d$	Depth of the water tunnel test section
$l_w$	Width of the water tunnel test section
$L_H$	Real-valued lift in Garrick model
$L_T$	Scaled length of the tail
$m$	Mass of the tail fin
$M_T$	Torque/moment on the tail fin about its pitching axis

$M_H$	Real-valued torque in Garrick model
$M_{z,\text{fin}}$	Measured hydrodynamic z-axis moment on the tail fin
$n_i$	Normal vector of the $i^{\text{th}}$ surface element
$p$	Power input to the fluid
$p_{\text{motor}}$	Motor power
$Re$	Reynolds number
$S$	Stride length
$s$	Span length
$St$	Strouhal number ( $\equiv fA/u$ )
$T$	Heaving/pitching cycle
$T_x$	Sensor $x$ axis torque
$T_y$	Sensor $y$ axis torque
$T_z$	Sensor $z$ axis torque
$T_M$	Muscle/spring tension force
$u$	Incoming flow speed
$V$	Motor voltage
$Y_0$	Zeroeth Bessel function of the second kind
$Y_1$	first-order Bessel function of the second kind
$y_F$	Lateral position of the tail fin's trailing/distal edge
$y_{\text{goal}}$	Goal lateral position in Mission 3

$y_{\text{slot}}$  Slot's lateral position

$L_H^*$  Lift in Garrick model

$M_H^*$  Torque in Garrick model

# Chapter 1

## Introduction

### 1.1 Motivation and Goals

Natural swimmers have benefited from millions of years of evolution, driving them to develop unique features to achieve high-performance swimming. Fishes vastly outperform any man-made underwater vehicles in terms of bulk swimming metrics such as speed, efficiency, maneuverability, and stealth. Typical man-made vehicles can reach a high efficiency with propeller, or high speed using jet-propulsion, but they generally lag in other aspects like maneuverability, stealth, or versatility (e.g. switching between high efficiency and high speed). To design the next generation of underwater vehicles that are able to achieve these features simultaneously, a comprehensive understanding of bio-propulsion is essential.

The idea of "bio-inspiration" is not new; it might have been used by our ancestors. "Yuloh" in ancient China (a stern sculling method) might mimic flapping fish tails, and rowing (a side sculling method) might be a simple imitation of a duck's paddling. Direct imitation of an animal's motion and design could be an attractive solution, but it's not able to build a thorough understanding of the propulsion mechanism and design features. Since the evolution of fishes may not have converged to the optimal design yet, those evolved features might not have hydrodynamic benefits, and they may even have disadvantages.

Moreover, direct imitations and modeling have to reduce the order of design complexity due to the complicated structure of biological systems and the limits of actuators. Therefore, the performance of biomimetic systems/robots is mostly limited or far from the performance of their biological analogs[1, 2, 3, 4].

To overtake or even surpass biological systems, we must deconstruct those systems to extract key information that is relevant to a particular performance goal, but also keep as much detail as possible. Most of the existing bio-inspired propulsion literature focuses on single or multi panel-like propulsors and hydrofoils operating in an unbounded fluid with tethered measurements [5, 6, 7]. These idealized configurations highlight some essential information but also miss several important features of fish swimming, such as effects of a solid boundary in environments[8], lateral recoils[9], three-dimensional wake interactions[10, 11], and real-time control of swimming behaviors[12, 13].

To distill the essential physics and design features of high performance swimming, this thesis uses both idealized models of propulsors and reduced order three-dimensional robotic platforms. All studies are especially motivated by thunniform swimming (like tuna), which is an apex predator famous for its high speed, high efficiency, and unique body structures [14, 15]. Specifically, this thesis will set out to answer the following questions:

- How does the performance and swimming behavior change when approaching the ground or another swimmer?
- How can one generate fish-like rapid streamwise and lateral maneuvers?
- In what ways does the dorsal fin design affect the swimming performance of a robotic fish?
- What is the optimal stiffness control law for variable-speed swimming?
- How does stiffness control affect the swimming performance of a robotic fish?

- How is the three-dimensional wake related to the effects mentioned above?

These questions will be explored using a combination of water tunnel experiments, three-dimensional Particle Image Velocimetry (3D PIV), viscid/inviscid simulations, and analytical modeling.

## 1.2 Boundary Interactions

Fish and birds are known to benefit from the “steady ground effect”, where lift forces are amplified near a seafloor or water surface. Trout, mandarin fish, gulls, and pelicans all use this effect to swim/fly more efficiently [16, 17, 18, 19]. When fins/wings oscillate near a boundary, they experience an “unsteady ground effect”, which can boost thrust as well as lift. Pitching hydrofoils can boost thrust and speed up to 45% and 25%—with no loss in efficiency—by swimming near the ground [20, 21, 22, 23]. Low Reynolds-number simulations produce similar trends [24, 25, 26, 27].

Unsteady ground effect is governed by phenomena that are absent in the steady ground effect. Oscillating near the ground produces asymmetric vortex streets, return flows, and vortex compression [20, 23]. Near-ground oscillations also cause asymmetric lift forces. It was hypothesized that a freely swimming pitching foil would settle into an *equilibrium altitude* as fluid-mediated forces pushed the foil to the edge of these lift regimes. This surprising result was shown for a constrained foil within a potential flow numerical framework [28], leaving open questions as to whether viscosity and/or recoil motions would disrupt the existence of these equilibrium altitudes.

Previous studies of the unsteady ground effect have considered single aspect ratios. It is therefore unknown how aspect ratio affects the wakes, thrust, and equilibrium altitudes of near-boundary swimmers and fliers. Biological observations suggest that it may be a critical design parameter. Benthic (bottom-dwelling) rays tend to have lower-aspect-ratio rounded pectoral fins, whereas pelagic (non-bottom-dwelling) rays have higher-aspect-ratio

triangular fins [29]. Changes in morphology as fish evolve to benthic lifestyles are, in fact, one of the “most common patterns of evolution among aquatic animals” [30].

### 1.3 Fish Maneuver

Fishes vastly outperform human-made vehicles when maneuvering at low speeds [31, 32]. In fact, maneuvering “appears to have been a major factor in the evolution of the chordate body plan” (Webb and Weihs n.d.). The maneuverabilities found in nature are thought to stem from body/fin flexibility [33] and networked control surfaces [34], but the details are poorly understood.

One way to categorize fish maneuvers is to separate them into streamwise (anterior-posterior) and lateral (left-right) maneuvers. Accelerating from rest would be a streamwise maneuver; coordinating a turn a lateral maneuver. Fish are experts at both. Trout and pike can accelerate forward at 40 and 50  $\text{m/s}^2$  [35]; goldfish have turning radii less than their body length [36].

A simple way to produce a streamwise maneuver is to adjust the tailbeat amplitude and/or frequency. Sunfish [37] and lampreys [38], for example, increase their tailbeat amplitude when accelerating. This strategy is common: across 51 species spanning 20 taxonomic orders, tailbeat amplitude increases by  $34 \pm 4\%$  during accelerations [9]. Once swimming steadily, a fish’s speed is more often controlled by tailbeat frequency alone [9, 39].

To perform a lateral maneuver, fishes have to break either their gait’s spatial or temporal symmetry. For example, one stroke of a fin could have a larger amplitude than the other stroke (spatial asymmetry) or be faster than the other stroke (temporal asymmetry). These asymmetries can be small, producing quasi-steady “trimming forces” [40, 41], or large, producing “powered correction forces” that drive unsteady flows and rapid maneuvers [34]. Our understanding of these strategies comes from applying aerodynamic intuition to bio-

logical observations: e.g., trimming forces are thought to be more efficient but only at high speeds [18].

While most bio-inspired propulsion studies have focused on symmetric motions (e.g. ), a few studies have considered maneuvers. An indirect but effective way of studying fish maneuvers is to characterize the dynamics of autonomous fish-inspired robots. Adding a pitch offset (spatial asymmetry) to a robotic tail fin has been used to study lateral maneuvers in salmon-like [42] and tuna-like [43] robots. Flapping faster in one direction than the other (temporal asymmetry) has been used to study maneuvers in tuna-like robots up to high frequencies [3]. A challenge of these studies is that robot efficiencies are estimated using noisy battery drain data, and precise force measurements cannot be done on untethered platforms. Wake studies are also limited by the difficulty of performing flow visualization on a moving target.

An alternate method of studying maneuvers is to use tethered fish-inspired platforms. Tethered platforms have revealed, for example, the role that flexibility and C-start kinematics play in rapid streamwise maneuvers [44, 45, 46, 47]. In a study of pitch-biased (spatially asymmetric) hydrofoils, researchers showed that pressure sensors could inform a lateral maneuver in a vortex street [48]. In another pitch-bias study, researchers recorded lateral force coefficients (lateral forces scaled by foil area and dynamic pressure) up to 5.5, suggesting rapid lateral maneuvers could result from pitch bias [49]. A limitation of these studies is that they do not allow recoil, or at least restrict recoil to one axis using linear air bushings.

## **1.4 Multi-Fin Interactions**

Complex interactions between a fish's multiple fins and body affect its swimming performance. Of particular importance is how dorsal/anal fins interact with the downstream caudal (tail) fin, because the caudal fin is the dominant thrust-producing fin in carangiform

and thunniform fish ([50, 51, 52]). In bluegill sunfish, [53] showed that the wake of the dorsal fin strengthens trailing-edge vortices behind the caudal fin. [54] found similar effects behind the dorsal and anal fins of brook trout. These fin-fin interactions are governed by complex, unsteady flows; in the case of sunfish, [55] used Particle Image Velocimetry to show that the interactions result from a system of intertwined three-dimensional vortex loops. Idealized setups have shown that fin-fin interactions persist in lower-order models. A rigid, pitching hydrofoil, for example, can increase the thrust and efficiency of a second hydrofoil downstream [56, 57, 58]. In these studies, emphasis is placed on the phase lag between the hydrofoils, because thrust and efficiency increase by different amounts – and can even decrease – depending on the phase.

In many high-speed carangiform and thunniform species, the dorsal and/or anal fins are elongated, stretching over a large portion of the fish’s proximal margin. In the Crevalle Jack (*Caranx hippos*), for example, thin dorsal and anal fins stretch along nearly the entire back half of the fish (Figure 5.1*a*, [59]). In mackerels and tunas, an array of small dorsal/anal “finlets” sits upstream of the caudal fin [60]. For notational convenience, we will henceforth discuss “dorsal” fins, but all results apply equally to elongated anal fins. Because of their close proximity to the caudal fin, these elongated dorsal features are likely to produce a strong interaction, because fin-fin interactions drop off quickly with distance [57]. Immersed-boundary-method-based flow simulations by [59] suggest that in the Crevalle Jack, the elongated dorsal fin increases caudal fin thrust by 13.4%. The simulations show that the caudal fin constructively interferes with vorticity shed from the dorsal fin. [61] used a three-dimensional potential flow solver to study dorsal-caudal interactions in a tuna-like model. They found that far-field wake modes depend on the phase lag between the dorsal and caudal fins, suggesting phase-dependent fin interactions. For these simulations, the Reynolds number based on swimming speed and whole body length is a limiting factor; whereas real fish may swim with  $Re \sim O(10^4) - O(10^5)$ , in those studies  $Re$  was 2100 (immersed-boundary-method) and effectively infinite (potential flow solver).

## 1.5 Tail Flexibility

For decades, scientists and engineers have tried to understand how fish maintain such high efficiencies over such a wide range of speeds. One of the “overarching themes” in this quest has been flexibility [62]. Fish are highly flexible: when limp, their bodies can be as pliable as loose-leaf paper (e.g.  $EI \approx 1\text{--}2 \text{ N mm}^2$  [63]). Theories, simulations, and experiments all show that flexibility can improve performance [64, 65, 66, 67, 68], yet fish-inspired robots—even those that are flexible—trail real fish in terms of speed and efficiency [69, 32, 70, 4]. Here we demonstrate a key missing feature that perpetuates this performance gap: *tunable stiffness*.

It has been hypothesized that there is no one “correct” fish stiffness, so fish tune their stiffness as they swim via active muscle tensioning [71]. Muscle activity in sunfish [72], for example, suggests speed-dependent tail stiffening. Electrical stimulations of dead bass [73] and eels [63] suggest that muscle tensioning could triple a fish’s effective stiffness. How muscles actively modulate stiffness is “poorly understood” [62], but proposed mechanisms include bilateral tendon tensioning [73, 74] and curvature control [75]. Because it is nearly impossible to measure the stiffness of live fishes as they swim, two key questions remain unanswered: what are the energetic advantages of tuning stiffness, and how should stiffness be tuned to maximize efficiency during free-swimming?

These questions apply equally to robotic fish, where stiffness-tuning mechanisms already exist. Robots can tune stiffness offline by swapping in/out passive stiffness elements [76, 77], or online by using adjustable linear/leaf springs [78, 79] bilateral soft actuators [80], artificial tendons [81], electrorheological modulation [82], or cyber-physical motor braking [3]. These studies show how stiffness-tuning mechanisms have unique pros and cons involving degrees of freedom, compactness, simplicity, and modularity. They also demonstrate how tuning stiffness can increase thrust production. It is still unclear, however, what stiffness-tuning strategies are best and how they relate to swimming efficiency.

## 1.6 Summary of Chapters and Contributions

- **Chapter 2** describes the development of the Intelligent Experimental System. First, the design details of the Intelligent Experiment Apparatus are described in section 2.1: digital-controlled water tunnel (section 2.1.1), air-suspension system (section 2.1.2), modularized motion actuators (section 2.1.3 and 2.1.4), tilting and leveling systems (section 2.1.5), electronics and wireless data communications (section 2.1.6 and 2.1.7). Then section 2.2 describes details of the three-dimensional Particle Image Velocimetry system. For all experiments, performance was measured by a force/torque sensor and encoder described in section 2.3. Finally, the Newton-Raphson based Free-swimming algorithm is described in section 2.4.

The results of the Chapter 2 were the foundation of all experiments in this thesis. This intelligent experiment system also forms the basis of the following journal publications:

- Ayancik, F., Zhong, Q., Quinn, D.B., Brandes, A., Bart-Smith, H. and Moored, K.W., 2019. Scaling laws for the propulsive performance of three-dimensional pitching propulsors. *Journal of Fluid Mechanics*, 871, pp.1117-1138. (Experiment related Sections).
  - Gunnarson, P., Zhong, Q. and Quinn, D.B., 2019. Comparing Models of Lateral Station-Keeping for Pitching Hydrofoils. *Biomimetics*, 4(3), p.51. (Experiment related Sections).
- **Chapter 3** presents the experimental setup and results of the unsteady ground effect studies. The two-dimensional case is considered first, including constrained performance measurements taken by [83], and unconstrained dynamics measurements and

simulations (section 3.2.1). Then constrained performance measurement results of finite aspect ratio cases with  $\mathcal{R}$  ranging from 2.5 to 1.0 are described in section 3.2.2 and 3.2.3. Comparison between experiments and inviscid simulations is described in section 3.2.4 at  $\mathcal{R} = 2.0$  and 1.0. Finally, section 3.3 discusses the existence of stable and unstable equilibrium altitudes, as well as Strouhal number, reduced frequency, and aspect ratio effects.

The results of Chapter 3 formed the basis of the following journal publications:

- Kurt, M., Cochran-Carney, J., Zhong, Q., Mivehchi, A., Quinn, D.B. and Moored, K.W., 2019. Swimming freely near the ground leads to flow-mediated equilibrium altitudes. *Journal of Fluid Mechanics*, 875. (Unconstrained Experiment related Sections).
- Zhong, Q., Han, T.J, Moored, K.W. and Quinn, D.B., 2021. Aspect ratio affects the equilibriums altitude of near-ground swimmers. *Journal of Fluid Mechanics*, In press.
- Mivehchi, A., Zhong, Q., Kurt, M., Quinn, D.B. and Moored, K.W., 2021. Scaling Laws for the Propulsive Performance of a Purely Pitching Foil in Ground Effect. *Journal of Fluid Mechanics*, In press. (Experiment related Sections).
- **Chapter 4** presents the experimental setup and results of fish-inspired maneuver experiments. The chapter begins with a description of the lateral position reset system, and the maneuver motion design and test protocol are in section 4.0.1. Section 4.1 then describes the experimental results. First, section 4.1.1 and 4.1.2 describe the bulk and instantaneous performance of a streamwise maneuver. Then section 4.1.3 and 4.1.4 describe the bulk and instantaneous performance of a lateral maneuver. Finally, section 4.2 discusses how frequency/amplitude modulation and spa-

tial/temporal asymmetry modulation apply to fish/robot maneuvers.

The results of Chapter 4 formed the basis of the following journal publication:

- Zhong, Q., and Quinn, D.B., 2021. Streamwise and lateral maneuvers of fish-inspired hydrofoils. *Bioinspiration & Biomimetics*, Submitted.

- **Chapter 5** presents details of wake interactions between the dorsal fin and caudal fin of the tuna-inspired platform. This chapter begins with a description of the experimental setup and methods (section 5.1) including tuna-inspired platform design, performance measurements, and simulations. Then section 5.2 presents experiment and simulation results. Section 5.2.1 presents the swimming performance with various dorsal fins, section 5.2.2 presents wake interactions in both experiments and simulations, and section 5.2.3 describes cone-shaped vortices introduced by the elongated dorsal fin. Finally, section 5.3 discuss caudal fin Leading Edge Vortex (LEV) stabilization due to interaction with the dorsal fin induced cone-shaped vortices.

The results of Chapter 5 formed the basis of the following journal publication:

- Zhong, Q., Dong, H. and Quinn, D.B., 2019. How dorsal fin sharpness affects swimming speed and economy. *Journal of Fluid Mechanics*, 878, pp.370-385.

- **Chapter 6** presents details of real-time adjustable flexibility of the tuna-inspired platform. First, section 6.1 describes experimental details, including tuna-tail stiffness tests, tuna-inspired platform with tunable stiffness tail design, self-propelled swimming performance test, variable speed swimming mission test, and modified tunabot construction and tests. Then section 6.2 describes details of modeling a robot fish

with a tunable stiffness tail. Section 6.3 then presents experiment and modeling results. First, section 6.3.1 compares a tuna tail, a model tail and a robotic tail. Then section 6.3.2 presents swimming speed and efficiency as a function of tail stiffness and tail-beat frequency. Section 6.3.3 describes scaling between stiffness and swimming speed, and section 6.3.4 discusses nonlinear wakes at high stiffnesses. Then, section 6.3.5 presents results of tunable stiffness in variable-speed swimming missions. Finally, section 6.4 discusses how tunable stiffness relates to swimmers and broader applications.

The results of Chapter 6 formed the basis of the following journal publication:

- Zhong, Q., Zhu, J., Fish, F.E., Kerr, S.J., Downs, A.M., Bart-Smith, H. and Quinn, D.B., 2021. How tunable stiffness enables fast and efficient swimming. *Science Robotics*, Under review.

To the best of the author’s knowledge, this study is (1) the first to build a wireless experimental system for bio-inspired propulsion studies, (2) the first to prove the existence of stable and unstable equilibrium altitudes of unsteady ground effects with high resolution experimental 3D flow visualization, (3) the first to investigate fish-inspired maneuvers with precise measurements of performance, dynamics, and flow, (4) the first to explore dorsal fin shape optimization in the context of multi-fin wake interactions, and (5) the first to explore real-time adjustable flexibility on robotic platforms with precise measurements of performance and flow. The results of these studies will support a variety of conclusions, which are presented in the following table:

Table 1.1: A summary of the major conclusions stated and discussed throughout the thesis with references to the section where the corresponding evidence is located. Part I

Chapter	Conclusion	Results
Pitching Propulsor: Boundary Interactions	(1) 2D: The swimmer generates asymmetric lift when swimming near the ground, leading to a stable equilibrium altitude.	3.2.1
	(2) 2D: Stable equilibrium altitude is independent of initial condition, but increases with increasing Strouhal number and decreasing reduced frequency.	3.2.1
	(3) 3D: The propulsor generates higher thrust with negligible change in efficiency.	3.2.2
	(4) 3D: The asymmetric lift force drops from positive to negative when very close to the ground ( $d/c \leq 0.35$ ), leading to another unstable equilibrium altitude.	3.2.2, 3.2.3
	(5) 3D: Increasing aspect ratio leads to stronger unsteady ground effects, including a stronger thrust boost, larger asymmetric lift magnitude, and higher .	3.2.3
	(6) 2D and 3D: Viscosity plays a minor role in unsteady ground effects.	3.2.1, 3.2.4
	(7) 2D and 3D: Unsteady ground effect collapses the vortex rings and vectors them away from the ground.	3.2.5
	(8) 3D: It is harder for high aspect ratio swimmers to boost thrust than it is for low aspect ratio swimmers due to strong asymmetric lift forces.	3.3
Pitching Propulsor: Fish-inspired maneuver	(1) At the same Strouhal number, a frequency-driven maneuver generates six times as much acceleration as an amplitude-driven maneuver.	4.1.1
	(2) Lateral recoil increases with increasing amplitude, but remains constant with frequency modulation.	4.1.2
	(3) Adding pitch bias (spatial asymmetry) leads to a steady lateral shift with nearly no changes in the streamwise direction.	4.1.3, 4.1.4
	(4) Modulating stroke speed ratio (temporal asymmetry) leads to a pulsed yaw torque/lateral force, resulting in displacement in both streamwise and lateral directions.	4.1.4,4.1.3
	(5) Temporal asymmetry generates a pair of vectored strong vortices which is qualitatively similar to fish turning.	4.1.4,4.1.5,4.2

Table 1.2: A summary of the major conclusions stated and discussed throughout the thesis with references to the section where corresponding evidence locates. Part II.

Chapter	Conclusion	Results
Tuna-inspired platform: Multi-Fin Interactions	(1) Swimming speed increases with dorsal fin sharpness, while economy peaks for the M4 case.	5.2.1
	(2) Leading Edge Vortices are stabilized on the caudal fin due to multi-fin wake interactions.	5.2.2
	(3) Dorsal-caudal fin interactions persist at lower Reynolds numbers.	5.2.2
	(4) Elongated sharp dorsal fins create streamwise conical vortices.	5.2.3
	(5) Wake interactions between elongated dorsal fins and caudal fins is insensitive to phase delay.	5.2.3
Tuna-inspired platform: Real-Time Adjustable Flexibility	(1) A tuna can increase its tail fin joint stiffness by pulling tendons harder.	6.3.1
	(2) Both swimming speed and efficiency are functions of tail muscle/spring tension (stiffness) and tail-beat frequency.	6.3.2
	(3) Constant muscle/spring tension (stiffness) only leads to high stride length and efficiency within a small range of tail-beat frequency.	6.3.2
	(4) Optimal muscle/spring tension (stiffness) should scale with swimming speed squared.	6.3.3
	(5) A too high stiffness introduces nonlinear flow wakes that hurt swimming performance.	6.3.4
	(6) Real-time stiffness tuning saves up to 55% energy in variable speed missions.	6.3.5
	(7) Tuning stiffness is most beneficial for high frequency fish and robots.	6.3.6

## **Chapter 2**

# **Development of the Intelligent Experimental System**

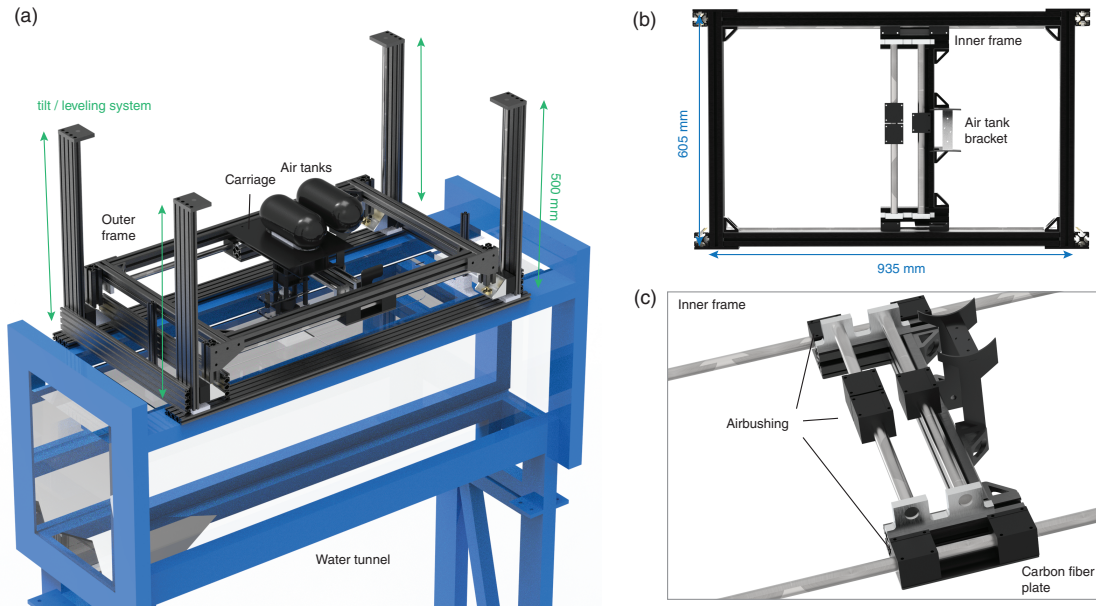


Figure 2.1: **Experiment system hardware.** (a) The experiment apparatus sits on the top of the water tunnel. (b) bottom view of the two-axis air suspension system. (c) detailed view of the inner frame of the two-axis air suspension system.

## 2.1 Intelligent Experiment Apparatus

To study bio-inspired propulsion in various conditions, such as unsteady ground effects, high-frequency pitching motion, asymmetric motion, etc., I built a water tunnel rig that overcomes traditional limitations on swimming experiments (Figure.2.1a). At a glance, this rig suspends swimmers (hydrofoils, tail fins, robot platform, etc.) into a test section, as with other setups. What gives the rig unprecedented capabilities are the following unique features: a two-axis air suspension system, modularized motion actuators, an automated leveling and tilting system, a wireless dual-direction communication system, and a three-dimensional Particle Image Velocimetry system.

### 2.1.1 Digital-Controlled Closed-loop Water Tunnel

All water tunnel experiments were performed in a free-surface recirculating water tunnel at the University of Virginia. The test section measured 1520 mm long, 380 mm wide, and

450 mm deep. Significant surface waves were found when the test propulsor operated at frequencies near the first gravity wave harmonic  $f_{g,1}$ . This natural frequency was estimated using the dispersion relation from Airy wave theory:

$$f_{g,1} = \sqrt{(g\pi/l_w) \arctan(\pi l_d/l_w)}/2\pi, \quad (\text{Eq. 2.1})$$

where  $l_w$  and  $l_d$  are the width and depth of the test section. This harmonic frequency was estimated and verified by experiment to be  $\approx 1.6$  Hz. A planar baffle was installed to prevent the significant surface wave whenever possible, which minimized the effect of these gravity waves.

The water tunnel conditioned the flow upstream of the test section. The first is a perforated plate, which reduces the turbulence to a small scale, followed by two fiberglass screens that further reduce the turbulence level. The last is a honeycomb flow straightener. The contraction section has an area ratio of 6:1. The geometry has been selected to provide the minimum contraction length consistent with good velocity distribution, turbulence reduction, and avoidance of local separation and vorticity development. The water tunnel's flow speed ranges from 0 m/s to  $\approx 1$  m/s, controlled by a built-in controller (AC 1200) with a manual input panel. The measured turbulence intensity level is  $< 1.0\%$  RMS up to 0.3 m/s. An Ultrasonic flow speed sensor (Dynasonics Series TFXB) was installed to measure the actual flow speed of the test section with a 0.001 m/s resolution.

To develop an intelligent experimental system for this water tunnel, the water tunnel's built-in controller is switched to be controlled by an external analog signal. This analog signal ranged from 0 V to 10 V, mapping to the desired flow velocity of 0 m/s to 1.0 m/s. A custom micro-controller was designed and programmed to take the desired flow speed input from a Labview interface on a control desktop via serial communication, then output a Pulse-Width Modulation (PWM) signal as a 0 ~ 5 V analog signal. This micro-controller-generated analog control signal was further amplified by a signal conditioner (OMEGA)

with a 0 ~ 5 V to 0 ~ 10 V range, then sent to the built-in controller of the water tunnel.

### **2.1.2 Two-axis Air Suspension System**

The two-axis air suspension system possesses two layered frames: the outer layer frame corresponding to the streamwise direction and the inner layer frame corresponding to the lateral direction. As shown in figure 2.1*b*, the outer frame's dimension is 935 mm in length and 605 mm in width and holds two stainless steel rails along the streamwise direction of the water tunnel. This pair of stainless steel rails were 36 inch (914.4 mm) long and 0.75 inch in diameter and installed carefully to ensure that they were near-perfectly parallel to each other at a distance of 534.7 mm. The outer frame is made with 1.5 inch (38.1 mm) aluminum extrusions and aluminum brackets (80/20 Inc.) to provide maximum stability and durability.

To compress the height of the rig and thus minimize the distance between the rig and water surface, the inner layer frame is designed to be 178 mm in length and 487 mm in width so that it can fit inside the outer frame. To minimize the inner frame's weight while keeping maximum durability, the inner frame consists of a "C" shape aluminum extrusion assembly and four custom-made 1/8 inch thickness carbon fiber plates (Figure 2.1*c*). Two of these carbon fiber plates stack together and attach to the inner frame with bolts for each side. On the top of the "C" shape aluminum extrusion assembly, another two parallel stainless steel rails (18 inch in length and 0.75 inch in diameter) are installed with a 69.7 mm separation distance.

On the side of the "C" frame, a custom-made carbon fiber bracket is installed to support a compressed air tank. Four (two for one side) air bushings (S301901 with 0.75 inch inner diameter, Newway air bearings Inc.) are installed on these plates with bolts. These bushings support the entire inner frame, which glides along the pair of streamwise stainless steel rails on the outer frame.

The carriage frame is constructed with aluminum standoffs and custom-made 1/8 inch

thickness carbon fiber plates to reach a balance between durability and weight. The carriage is a two-layer structure to reserve enough room for air systems, electronics, and air tanks. A 3D printed bracket is installed on the center of the first layer plate and through a hole on the second layer plate, which works as another compressed air tank support. On the bottom of the first layer plate, three air bushings are installed with a triangular arrangement. These bushings support the carriage, which glides along the lateral stainless steel shafts (one air bushing for the first shaft, two air bushings for the second shaft) on the inner frame.

Because the rig is intended to be fully wireless, a compressed air tank-based system allows the rig to carry the air source by itself. As mentioned above, two compressed air tanks (Ninja HPA Tank - 68/4500) made of carbon fiber are installed for two axes of air bushings. One tank is installed on the inner frame to provide compressed air for the stream-wise air bushings, and the other is installed on the carriage for the lateral air bushings. The compressed air tanks store nitrogen at 4500 psi, then regulate the high-pressure air from 4500 psi to 65 psi by inline regulators (CUSTOM PRODUCTS V2). To incorporate the air system with other electronics, two digitally controlled solenoid valves are installed on the air system to open/close the air with input commands from the control desktop.

To record the position of the carriage, two high-precision laser sensors (Baumer C8501) are installed on the carriage for the lateral position and on the inner frame for the stream-wise position. All parts and accessories used in the two-axis air suspension are painted in matte black or covered with a black anodized surface to avoid any possible reflecting or shining surface in preparation for laser-related studies.

### **2.1.3 Low frequency ( $\leq 2.5$ Hz) Pitching Actuation Module**

To prepare for diverse research studies, the motion actuators are designed to be modularized. For studies that focus on low-frequencies with variable pitching amplitude, pitching motion is generated by a simple servo-based pitch actuator (Figure:2.2) installed on the bottom of the carriage. A custom-made shaft (3/8 inch diameter with stainless steel) is

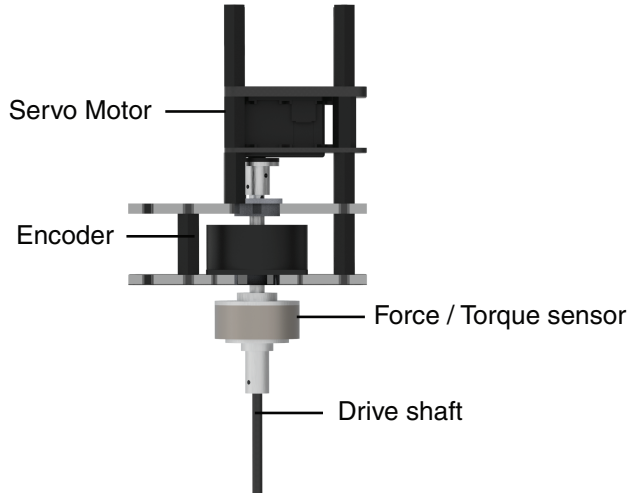


Figure 2.2: **Diagram of low frequency pitching actuator**

Table 2.1: Mini40 force/torque sensor calibration.

Calibration	$F_x, F_y$	$F_z$	$T_x, T_y$	$T_z$	$F_x, F_y$	$F_z$	$T_x, T_y$	$T_z$
SI-20-1	20 N	60 N	1 Nm	1 Nm	1/200 N	1/100 N	1/8000 Nm	1/8000 Nm
SI-40-2	40 N	120 N	2 Nm	2 Nm	1/100 N	1/50 N	1/4000 Nm	1/4000 Nm
SI-80-4	80 N	240 N	4 Nm	4 Nm	1/50 N	1/25 N	1/2000 Nm	1/2000 Nm
	Sensing Ranges				Resolution			

installed on the output wheel of a high torque digital servo motor (Dynamixel MX-64) to transmit motion to the hydrofoil. An absolute encoder (US Digital A2K 4096 CPR) is installed on the shaft to record the output motion with a 0.01 degree resolution. A six-axis force/torque sensor (Mini 40 IP 65/67) is installed to measure the force transmits to the swimmer on the end of the shaft. This force sensor equipped with three different calibration files; details are in Table.2.1.

#### 2.1.4 Rotary-based High Frequency ( $\leq 7.0$ Hz) Actuation Module

We also designed a rotary-based pitching actuator that allows us to test at tailbeat frequencies up to 7 Hz. Our design is a modified “Scotch-yoke mechanism”, which converts rotary motion to linear motion. The actuator consists of three individual parts: a frequency module, an amplitude module, and a pitch bias module (Figure.2.3). Together, the modules

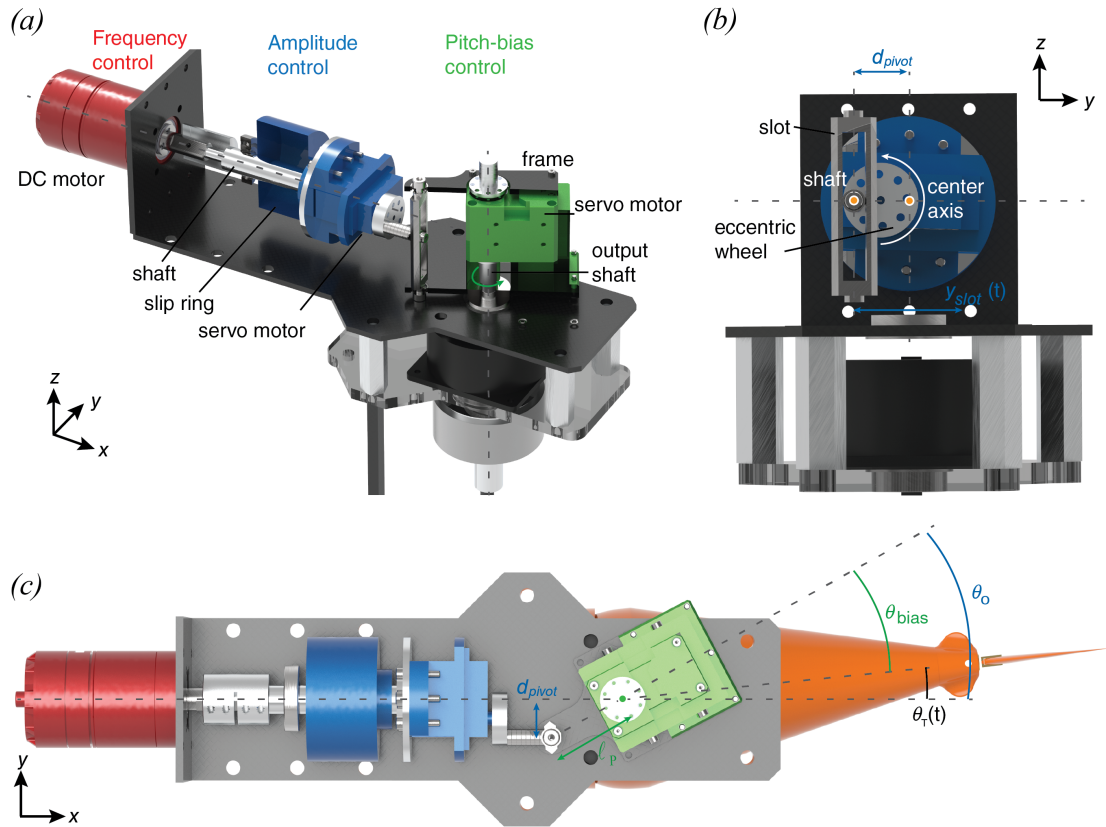


Figure 2.3: **High-frequency pitching actuator design.**(a) The actuator consists of three modules: frequency (red), amplitude (blue), and pitch bias (green). Together, the modules convert the rotary motion of a DC motor into pitching motions of the platform's tail. (b) A detailed view of amplitude control. The distance between the shaft and the central axis of the eccentric wheel is adjusted by a smart servo. The slot converts the motion of the rotating pin into periodic heaving motions. (c) A detailed view of pitch bias control. A servo adjusts the neutral angle of the pitch bias module, thus giving an offset,  $\theta_{bias}$ , to the pitch motions of the driveshaft.

control the frequency  $f$ , amplitude  $\theta_0$ , and pitch bias  $\theta_{\text{bias}}$  of the platform's tail: (0.5-7 Hz, 0-35°, and 0 to 20°, respectively).

The *frequency module* rotates a drive-shaft using a high-torque smart brushless digital DC motor (3 Nm, 488 rpm) (figure. 2.3a). The motor speed is closed-loop controlled using an onboard controller (OpenCM 9.04 + OpenCM 485 expansion board). The motor rotates a stainless-steel shaft (12.7 mm diameter) that ends in a circular disk upon which the amplitude module is attached.

The *amplitude module* uses a tunable eccentric wheel to control the amplitude of the tail fin oscillations (Figure.2.3b). The module's base was 3D-printed from polycarbonate-ABS, while its eccentric wheel was machined by a CNC machine with stainless steel material. The eccentric wheel is rotated by a high-torque precision smart servo (Dynamixel XH430) driven by a Micro Controller Unit (MCU3-sub). Rotating the wheel adjusts the distance between a pin in the wheel and the DC motor axis ( $d$ ) from 0 to 20 mm. As the DC motor rotates, it drives a slot's motion that connects to the pitch bias module. The lateral position of slot ( $y_{\text{slot}}$ ) as a function of time ( $t$ ) is

$$y_{\text{slot}}(t) = d_{\text{pivot}} \cos(T) \quad (\text{Eq. 2.2})$$

where  $T = 2\pi ft$ . The *pitch bias module* converts the heaving motion of the slot into a pitching motion (Figure.2.3c). The slot is seated such that it can rotate on the 3 mm carbon fiber frame to which it is attached, and the pitch bias module is free to rotate around the axis of the platform tail's driveshaft. The result is that the driveshaft rotates back and forth at the angular frequency of the continuously rotating DC motor. A co-axial servo motor adjusts the neutral angle of the pitch bias module, thus allowing offsets in the driveshaft's pitch oscillations ( $\theta_{\text{bias}}$ ). The angle of the driveshaft is

$$\theta_T(t) = \arcsin\left(\frac{y_{\text{slot}}}{\ell_P}\right) + \theta_{\text{bias}} = \arcsin\left(\frac{d_{\text{pivot}} \cos(T)}{\ell_P}\right) + \theta_{\text{bias}} \approx \theta_0 \cos(T) + \theta_{\text{bias}} \quad (\text{Eq. 2.3})$$

where  $\ell_P$  is the fixed distance from the slot to the driveshaft,  $\theta_0 \equiv \arcsin(d_{pivot}/\ell_P)$ , and the small-angle approximation was applied.

To verify the motions of the tail, we installed an absolute encoder (US Digital A2K 4096 CPR) in line with the driveshaft. The measurements were converted to an analog signal and streamed to two places: 1) to a custom circuit board that relayed the data back to the main control computer (to verify the commanded motion), and 2) to an onboard controller designed for closed-loop position control. We also used an on-board sensor (ATI mini40 SI-80-4) to measure forces/torques on the drive shaft.

### 2.1.5 Tilting and Leveling System

A tilting and leveling system was built as the base of the two-axis air suspension system. Four high-precision linear actuators raise/lower each corner of the two-axis air suspension system independently (Figure.2.1a). Each high precision linear actuator consists of a high torque stepper motor (NEMA 57), a digital controlled brake clutch, an end position switch sensor, an aluminum extrusion frame, a high precision lead screw (1204), and a driver (TB6600). All four linear actuators and end switch sensors were connected to a microcontroller (Arduino Mega 2560), then communicated with the control desktop via a Labview interface.

The digitally-controlled brake clutches open when the Tilting and Leveling system is powered on. After the Tilting and Leveling system is activated by the LabVIEW interface, all four linear actuators start the *initialization* process by moving to the lower end with a 1 mm/s speed until reaching the end switch sensor. Therefore, the Tilting and Leveling system can find its actual *zero* references for leveling/tilting actions. By inputting desired altitude and bias angles in the LabVIEW interface, the desktop computer controls the Tilting and Leveling system to move to the target position. The maximum height is limited to 360 mm to avoid collision with the frame.

By changing the configuration of the driver, we can change the resolution of the stepper

motor from 6400 to 200 steps per revolution, thereby changing linear actuator resolution from 0.000625 mm to 0.02 mm. For studies in this thesis, the resolution of the linear actuator was fixed at 0.00246 mm. When used independently, the linear actuators auto-level the carriage to  $\pm 0.001^\circ$  precision, which reduces the effect of gravity during maneuver tests to  $\approx 18$  mN. When used synchronously, the linear actuators offer a  $z$ -traverse with a 0.00246 mm resolution, which enables us to capture layers of phase-averaged Stereo Particle Image Velocimetry (Section 2.2.2).

### **2.1.6 Carriage Electronics and Data Acquisition Method**

All electronics, including a power source, are installed on the carriage to achieve fully wireless control. The main power source of the carriage is a 6S 5000 mAh LiPo battery with a 16.8 voltage output. This output voltage is regulated to two levels: 12 V and 5V, as the power source for different sensors and actuators. The six-axis force/torque sensor is powered by its own battery pack inside the force/torque wireless transmitter (F/T Wireless). Details of voltage regulation for each sensor and actuator are in Table.2.2. It should be noted that because the carriage is powered by a single power source (a LiPO battery), it can be powered by a 12 V external power source for tests longer than 10 hours.

There could be a time delay between each sensor's measurement if signals were sent back to the desktop computer individually with independent wireless transmitters. These potential time delays could result in serious errors, especially for phase-sensitive analyses. Therefore, it is important to minimize the possible time delay between each measured signal before it is sent back to the desktop computer. Since we can not make modifications to the F/T wireless transmitter and force/torque sensor, all other signals (except force and torque signals) are conditioned/amplified to meet the requirement of the F/T wireless transmitter analog input. A custom-designed circuit is fabricated to regulate analog sensor signals to  $2.5V \pm 250$  mV analog signals (Table.2.3). Those regulated signals are packaged together and connected to port 3 of the F/T wireless transmitter, then streamed to the

Table 2.2: Input voltage specifications of carriage electronics.

Power source	powered devices	powered devices
16.8 V Battery or external power source	12 V Solenoid Valves Servo Motor Laser Sensors Encoder	5 V Arduino Xbee Laser Alignment unit Custom signal conditioner
F/T Wireless transmitter	six axis force/torque sensor	

Table 2.3: Sensor output voltage regulation and amplification.

Sensor	default output	constrained output	conditioned output
Encoder	0 ~ 5 V	4.17 ~ 5 V	2.5 V $\pm$ 250 mV
Laser sensor1	0 ~ 10 V	0 ~ 10 V	2.5 V $\pm$ 250 mV
Laser sensor2	0 ~ 10 V	0 ~ 10 V	2.5 V $\pm$ 250 mV

desktop computer packaged with the force/torque sensor data.

## 2.1.7 Control command Protocol

The desktop computer controls all experiment subsystems via a single LabVIEW interface, so it is necessary to develop a simple and clear command protocol to send control commands efficiently. All systems shown in figure 2.4 share a universal control command protocol based on serial communication at a 57600 baud-rate. The desktop computer uses an XBee to send wireless commands to an XBee on the carriage and a USB cable for the water tunnel and leveling system. For each subsystem, the LabVIEW interface establishes a corresponding VISA port and sends commands simultaneously via these ports. For those subsystems requiring multiple inputs, the LabVIEW interface concatenates inputs into a single string with commas separators.

Table 2.4: Example of concatenated string command sent to carriage.

Format:	Amplitude*10,	Frequency*10,	Cycles,	Bias*10,	Air signal
Example:	125	, 25	, 30	, 30	, 1

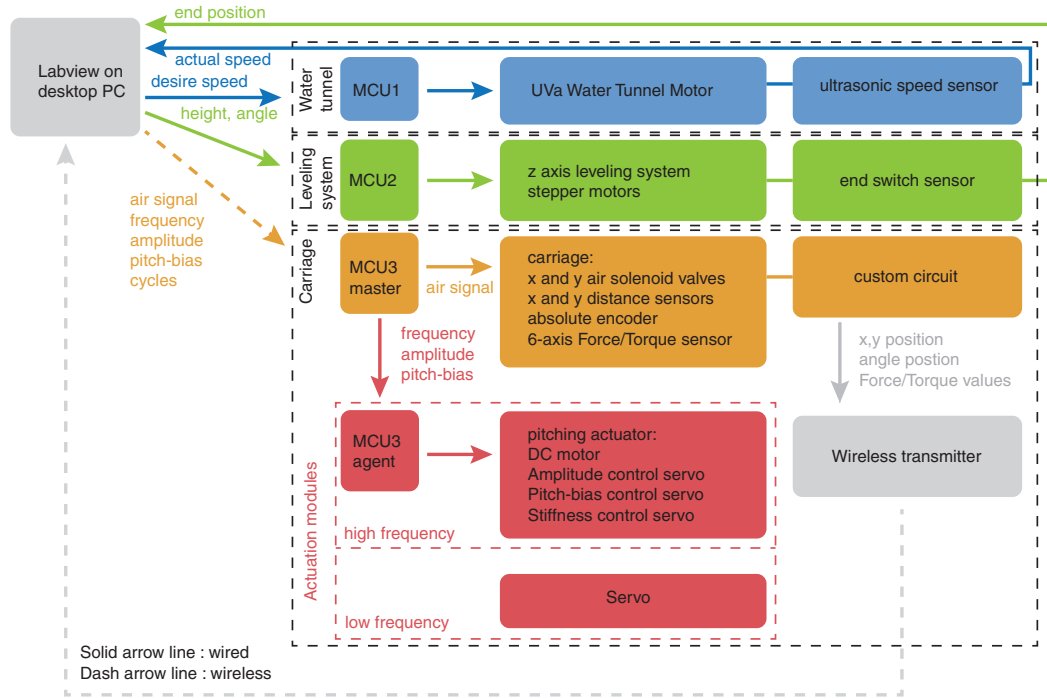


Figure 2.4: **Communication layout of the experiment system**

Table.2.4 shows a representative command sent to the carriage for generating a sinusoidal motion with a bias angle. Inputs with decimals are multiplied by 10 and rounded up to simplify the structure of the string command. After the micro-controller receives the command, it deciphers the command and converts it into individual input values. For example, the command shown in Table.2.4 is asking the low-frequency actuator to generate a 30-cycle sinusoidal motion with a  $12.5^\circ$  pitching amplitude, a 2.5 Hz pitching frequency, and a  $3^\circ$  bias angle. The motion generation program of the micro-controller is set to run at 100 Hz and is thus able to send a desired angle command to the servo every 10 ms. Moreover, this sample command also contains an air control signal at the end. A switch structure is applied to control two solenoid valves of the air system as follows:

- case 0: input 0, both valves off;
- case 1: input 1, x valve on and y valve off;
- case 2: input 2, x valve off and y valve on;

- case 3: input 3, both valves on;

This command protocol is widely used in other subsystems such as water tunnels and leveling systems due to its simplicity and flexibility. However, the deciphering process in a micro-controller requires more than 10 ms to extract information, which is not suitable for some fast-updating situations, like real-time motion updating or closed-loop feedback motion control. To satisfy those requirements, we developed another type of command protocol that focuses on reducing communication time and allows the desktop computer to control the motion in real-time. In this protocol, each input is adjusted and assigned to a constant length string block, then concatenated together. Because the desired angle position could have a negative value, a shift value is added to shift the inputs from negative to positive.

Table 2.5: Example of concatenated string with fixed length sent to carriage.

Format	angle position			Air signal
Desire 1 :	-12.5°			1
Command 1:	1	7	5	1
Desire 2 :	5.1°			1
Command 2:	3	5	1	1
Desire 3 :	-25.0°			1
Command 3:	0	5	0	1

Table.2.5 shows three representative commands sent to the motion actuator to reach specific angle positions. In these cases, the shift value is  $30^\circ$  and the maximum pitching angle is limited to  $\pm 30^\circ$ . Unlike the previous command protocol that sent motion parameters to the micro-controller to generate a motion profile, this command protocol only forwards one position every few micro seconds from the Labview interface to the micro-controller. In this thesis, the Labview interface is modified to send out the motion position at 100 Hz. After the micro-controller receives the command, it reads the first three characters, then converts them to the desired angle position, then reads the last character as the air signal. This command protocol constrains the input command and simplifies the deciphering pro-

cess, thereby allowing the system to perform arbitrary motions and closed-loop feedback control in real-time.

## **2.2 Particle Image Velocimetry System**

### **2.2.1 Stereo Particle Image Velocimetry**

To explore wake patterns around the swimmer during maneuvers in chapter 4, we used Stereo Particle Image Velocimetry (SPIV) to generate flow fields. The flow was seeded with neutrally buoyant polyamide particles ( $12\ \mu\text{m}$  average diameter), which were illuminated by two overlapping laser sheets (5 W Raypower MGL-W-532, and 10 W CNI MGL-W-532A). The lasers were fired from opposite sides to avoid a shadow. Two cameras beneath the channel recorded  $2956 \times 1877$  pixel images of the particle motions (Phantom, SpeedSense M341).

To isolate the key features of the flow fields, we phase-averaged the PIV data. We averaged 1000 frames over 25 pitching cycles in order to get 40 phase-averaged frames. Cross-correlations were calculated by an adaptive PIV algorithm (Dantec Dynamic Studio 6.1) with  $16 \times 16$  px overlapping interrogation windows, and the phase-averaging, layer stitching, and vorticity calculations were done in Matlab (2019). Flow field plots and animations were produced in Tecplot (2017R2).

### **2.2.2 Three-dimensional scanning Particle Image Velocimetry**

To understand the complicated three-dimensional wake patterns around the swimmer in chapter 3, 5, and 6, we developed a three-dimensional (3D) PIV system (figure 2.5). The laser sheet remains stationary while the leveling system raises/lowers the carriage. We start the first layer at the platform's midline, move to the next layer with a user-defined layer separation distance, then repeat this procedure, finishing with three extra layers below

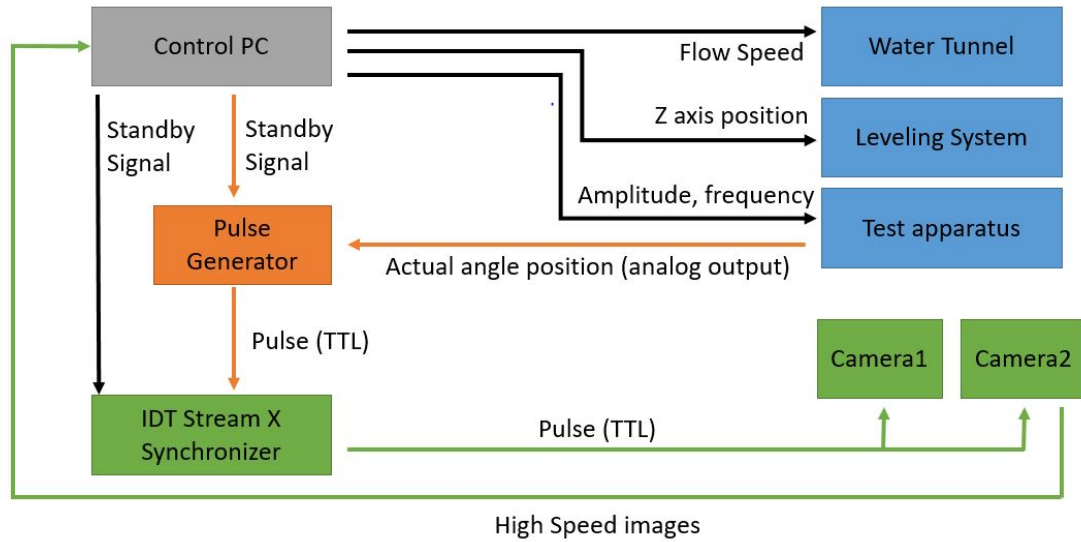


Figure 2.5: System Diagram of Three-Dimensional PIV System

the bottom edge of the swimmer. To avoid the wake of the driveshaft, we mirror the bottom layers across a horizontal plane at the midline. Because the 3D PIV consists of multiple SPIV layers along the  $z$  axis, it is essential to keep the same start phase for each layer. A custom-designed pulse generator (based on Arduino nano) was designed to synchronize angle signals from our custom experimental system to the shutter timing of the high-speed cameras. There are two different ways to perform phase-lock PIV:

- Method 1: The pulse generator generates a single pulse to drive cameras to take one frame when the swimmer passes the desired phase in a desired flapping direction.
- Method 2: When the swimmer passes the desired phase with a desired flapping direction for the first time, the pulse generator treats that as a start condition, then generates a series of pulses with a specific frequency.

The first method does not require precise frequency control of pulse signal generation and motion but is time-consuming for capturing a series of time-frames for a complete flapping cycle. In contrast to the first method, the second method relies on precise frequency control of motion and pulse signal but requires the ability to generate ultra-high-frequency pulse signals. For example, a 200 Hz pulse TTL signal is required to capture a 5 Hz motion

with 40 phase frames per flapping cycle. In this thesis, all 3D PIV was performed with the second method because our custom pulse generator is able to generate precise TTL pulse signals with frequency ranges from 30 Hz to 65000 Hz. We also made a new Labview interface that incorporates the 3D PIV system into our experimental system and offers a semi-automatic way to perform 3D PIV. When creating 3D wake isosurface plots, we phase-averaged across pitching cycles. The phase-averaging, as well as the merging from 2D to 3D and the vorticity calculations, were performed in Matlab (2019a), and the three-dimensional vorticity plots were created in Tecplot (2017R2).

## 2.3 Swimming Performance Measurement

### 2.3.1 Drag Profile Measurements

We designed a drag measurement test to build drag profiles for each swimmer before the experiment. To gain maximum resolution and reduce possible sensor drift, we use a high-resolution one-axis force sensor (Interface Inc., ULC Ultra-Low Capacity Load Cell, 1 N) to perform the test. Figure 2.6 shows representative results of a drag profile for a teardrop shape hydrofoil with  $\mathcal{R} = 1.5$  and chord  $c = 95$  mm over various incoming flow speeds. A 0.196 N pre-load force was attached during the test to shift the measurements within the optimal measurement range of the sensor. Then we fitted the measurements to get the drag as a function of flow speed and calculated the drag coefficient to be 0.7 ( $C_D \equiv Drag / (0.5\rho u^2 c^2)$ , where  $\rho$  is water density).

For the tuna-inspired platform, we use the same measurement protocol for head only and whole body to gain the drag profile of the head  $D_{\text{head}}$  and the whole body  $D_{\text{wholebody}}$  as functions of flow speed. For the tuna-inspired platform used in chapter 6, the drag coefficient was 0.046 ( $C_D \equiv Drag / (0.5\rho u^2 \ell^2)$ , where  $\ell$  is body length.) for whole body and 0.057 with the tail removed (head only).

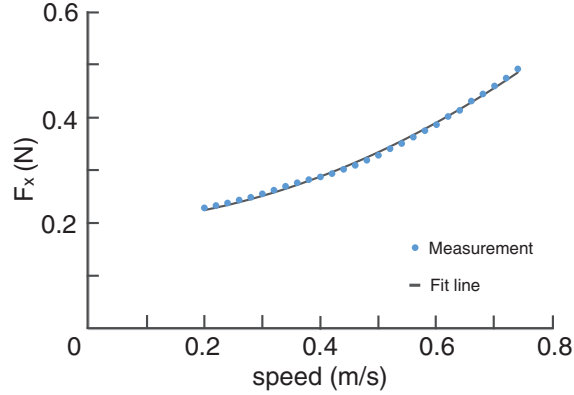


Figure 2.6: **Drag profile of  $R = 1.5$  teardrop hydrofoil.** Fit line:  $F_x = 0.53u^2 + 0.196$ ,  $R^2 = 0.99$  The constant coefficient was constrained at 0.198 because a 0.198 N pre-load force was attached during the test.

### 2.3.2 Force, Power, Efficiency, and Economy

We measured forces and power input to the fluid with measurements from the six-axis force/torque sensor and encoder. The measurements of the six-axis force/torque sensor drift slightly with time (0.0125% ~ 0.05% of its measurement range), which results in noticeable errors in performance measurements. To fix this drift, a five second stationary calibration period is introduced before the test motion for each test trial. Because the swimmer stays still during this period, those measurements can be seen as the bias of the force sensor. By subtracting the mean value of these biases for each axis, the effective measurements are re-calibrated. It should be noted that since the swimmer is suspended with an incoming flow, the calibration value of  $F_x$  should be the expected static drag instead of zero.

After the offsets are corrected, all raw measurements are coupled with the measured angle position  $\theta$  from the encoder to transform from force/torque sensor coordinates to water tunnel coordinates to get streamwise ( $F_S$ ) and lateral forces  $F_L$ . These two forces are further time-averaged over 20 cycles to produce "net thrust"  $\overline{F_T}$  and "net lift"  $\overline{F_L}$ . See [84] for a validation of our system based on prior work. For the tuna-inspired platform, the "net thrust" ( $\overline{F_T}$ ), is the sum of the drag on the head ( $D_{\text{head}}$ ) and the cycle-averaged streamwise

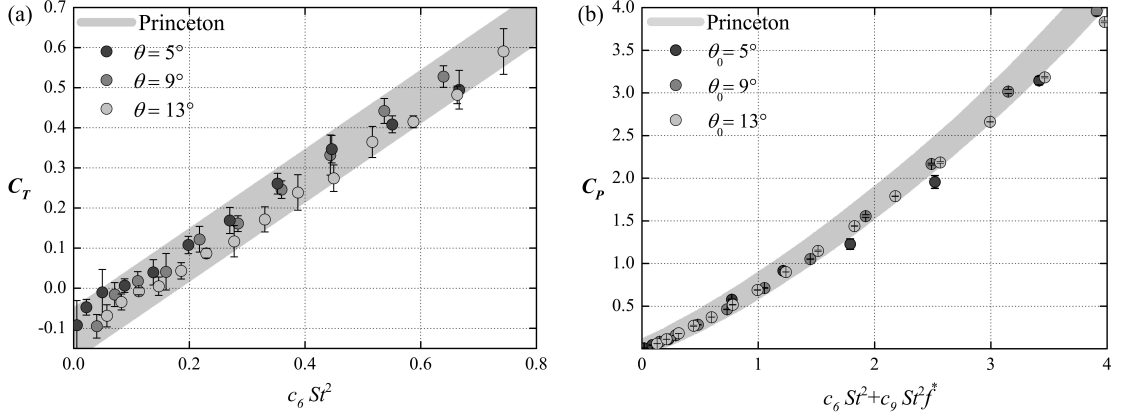


Figure 2.7: **Validating thrust/power measurements.** (a) The measured thrust coefficient agrees with published values. Thrust coefficient is defined as  $C_T \equiv \overline{F_T}/0.5 \rho a u^2$ , where  $\rho$  is water density and  $a$  is airfoil area (twice the span times chord). Frequency is scaled as it was in the previous study [7] to facilitate comparisons: the scaling constant  $c_6 = 2.55$ . Error bars show  $\pm$  one standard deviation, and the shaded band shows an envelope circumscribing the published values [7]. (b) The measured power coefficient also agrees with published values, particularly at lower frequencies. The reduced frequency is defined as  $f^* = 2\pi f c/u$ , where  $c$  is chord length, and the scaling constant  $c_9 = 4.89$ .

force on the body ( $\overline{F_S}$ ).

For tethered swimming with positive "net thrust", the propulsive efficiency is defined as  $\eta \equiv \overline{F_T} u / \overline{p}$ , where  $\overline{p} \equiv \overline{\tau_z \dot{\theta}}$  is the time-averaged power based on the pitching torque ( $\tau_z$ ) and pitching velocity ( $\dot{\theta}$ ). For steady swimming cases (self-propelled swimming condition), where the net thrust ( $\overline{F_T}$ ) is zero, we measured the propulsive economy defined as  $\xi = u / \overline{p}$ , which is a measure of the model's range, or distance travelled per unit energy.

### 2.3.3 Performance Measurement System Validations

We validated the accuracy of our setup by comparing our force/torque data to data from a previous study in a similarly-sized closed-loop water channel at Princeton University [7]. As in our study, the previous study measured forces and torques on rigid pitching airfoils. Our measured time-averaged thrust and power coefficients agree very well with the published values (figure 2.7a). To make a fair comparison, we matched all possible experimental conditions. First, we recreated a rigid airfoil with the same geometry: a

teardrop cross-section, an 80 mm chord, a maximum thickness of 8 mm, and an aspect ratio of 3.5 [7]. To minimize differences in vibrational noise, we used the same distance between the bottom of the force sensor and the top edge of the airfoil (2.5 cm). We used a horizontal splitter plate to match the depth of the Princeton channel (300 mm) and used the same free-stream velocity, 60 mm/s (a chord-based Reynolds number of 4780). We recreated three of the reported pitch amplitudes,  $\theta_0 = 5, 9$  and  $13^\circ$ , over a range of frequencies. Each individual trial was performed 7 times with 30 total cycles: 5 cycles for a warm-up period, 20 cycles for data acquisition, and 5 cycles for a cooling period. To increase the signal-to-noise ratio at low frequencies ( $f < 0.5$  Hz), we applied a 2nd-order Butterworth filter ( $6f$  cutoff frequency) to all instantaneous force and position data. The only difference between setups was that the previous study's airfoil was a single piece of anodized aluminium, whereas ours was 3D-printed (Dimension 1200es) with ABS and fixed to a carbon fiber drive rod. To be consistent with the previous study, we did not remove inertial forces by subtracting forces in air from forces in water. Given the lower frequencies used for our validation, we do not expect this difference to significantly affect our comparison, though it may explain the slight discrepancy between the two studies in the power reported at higher frequencies (figure 2.7b).

## 2.4 Newton-Raphson based Free-Swimming Algorithm

In order to find free-swimming speed with given input parameters, a Newton-Raphson based Free-Swimming Algorithm was developed. Before the experiment, a preliminary test was performed to find suitable test speed range for given parameters. At each swimming speed, the Newton-Raphson-based zero-finding scheme was used to determine the pitching frequency  $f$  that produced zero net thrusts. Each iteration of the scheme consists of a warm-up period (5 pitching cycles), a data-acquisition period (30 pitching cycles), and a cooling period (1 second). After two initial guesses for  $f$ , the scheme chooses the

next frequency as the intercept of a  $f(\overline{F_T})$  line fitted through the two guesses. This process iterates until net thrust is less than a threshold value was lower than 5% of the static drag, which was considered steady swimming within the uncertainty of the system. The scheme and subsequent measurements were applied to each swimming speed five times. This algorithm was used in both chapter 5 and 6.

## 2.5 Summary and Configuration for Studies

The modularized design of the experiment system allow us to change configuration with different hardware add-ons and software for various studies. In Chapter 3, the lateral actuator and automatic parameter swipe program are added for the boundary interaction studies ( $\geq 10000$  test trials); In Chapter 4, the position reset subsystem and close-loop controlled maneuver program are added for the fish inspired maneuver study; In Chapter 5, the Newton-Raphson based free swimming program and pitching actuator are added for multi-fin interaction study; In Chapter 6, the Newton-Raphson based free swimming algorithm, the closed-loop swimming mission program, the robotic platform with tunable stiffness actuator, and the rotary-based high frequency motion actuator are added for the real-time adjustable flexibility study.

# Chapter 3

## Pitching Propulsor: Boundary Interactions

This chapter gives the results of experiments and inviscid simulations that explore the effects of unsteady ground effects. We set out to answer four questions: (1) Do equilibrium altitudes exist for an oscillating foil in the presence of a solid boundary ? (2) Does aspect ratio affect near-boundary thrust and efficiency? (3) Does aspect ratio affect the existence and/or position of equilibrium altitudes? (4) Does aspect ratio affect the evolution of the 3D asymmetric wakes behind near-boundary propulsors? We answered these questions through a combination of direct force measurements, potential flow simulations, and 3D Particle Image Velocimetry (PIV).

### 3.1 Experiment Setup and Methods

#### 3.1.1 Constrained performance measurement of two-dimensional hydrofoil

Constrained foil experiments were conducted in a closed-loop water channel with a test section of 4.9 m long, 0.93 m wide, and 0.61 m deep. In order to produce a nominally

two-dimensional flow, a splitter and surface plate were installed near each hydrofoil tip. A vertical ground wall was also installed on the side of the channel. Five different non-dimensional amplitudes were tested:  $A^* = 0.125, 0.25, 0.38, 0.49, \text{ and } 0.61$ . The non-dimensional ground distance was varied within a range of  $0.25 \leq D^* \leq 2.6$ . Lift measurements were conducted with a six-axis force sensor (ATI Nano43). The lift data were time-averaged over 100 oscillation cycles, and each reported data point is the mean value of five trials. This section was performed at the Lehigh University by [83].

### **3.1.2 Unconstrained dynamics measurement of two-dimensional hydrofoil**

Tests were also conducted for a pitching hydrofoil that was unconstrained in the cross-stream direction. A nominally two-dimensional flow was achieved by installing a horizontal splitter plate and a surface plate near the tips of the hydrofoil. The gap between the hydrofoil tips and the surface/splitter plate was less than 5 mm. Surface waves were also minimized by the presence of the surface plate. The wall of the channel was used as a ground plane, and the ground distance was recorded by a laser distance sensor (Baumer CH-8501). The hydrofoil was placed at three initial positions:  $D_0^* = 0.25, 0.5 \text{ and } 0.75$ . Each trial included at least 80 oscillation cycles. Details of unconstrained airbushing systems, and position tracking are described in section 2.1.2.

### **3.1.3 Constrained performance measurement of finite aspect ratio hydrofoils**

To study aspect ratio, we tested hydrofoils with the same chord ( $c = 95 \text{ mm}$ ) and four aspect ratios: 1, 1.5, 2 and 2.5 (Figure. 3.1*a-b*). The hydrofoils had a tear-drop cross section and were 3D-printed with solid ABS. A stainless steel driveshaft (6.35 mm diameter) pitched the hydrofoil at its leading edge, i.e. pitch angle  $\theta$  was prescribed as  $\theta_0 \sin(2\pi ft)$ , where  $\theta_0$

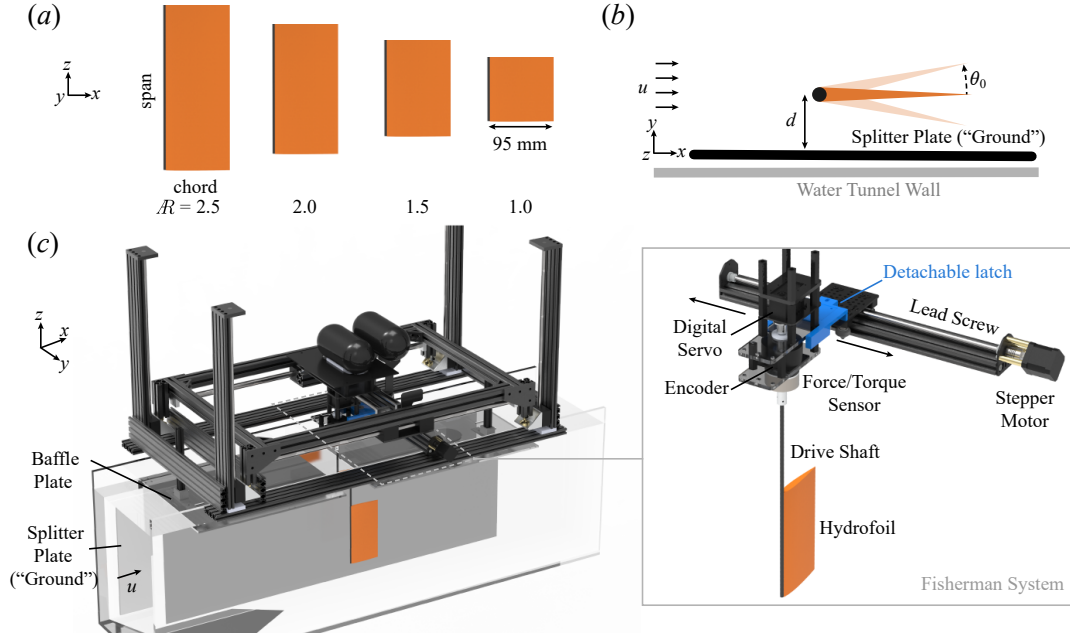


Figure 3.1: **Experimental setup.** (a) Four different aspect ratios ( $\mathcal{R}$ ) were tested. (b) The foils underwent pitch oscillations near a splitter plane (pitch amplitude  $\theta_0$ , ground proximity  $d$ , incoming flow speed,  $u$ ). (c) A  $z$ -traverse raised and lowered the foils in a water channel to facilitate Particle Image Velocimetry. A baffle plane reduced the effect of surface waves. Insert: an automated  $y$ -traverse (“Fisherman System”) controlled ground proximity by using a detachable latch to shift the foil’s lateral position ( $\pm 0.01$  mm resolution).

is pitch amplitude,  $f$  is frequency, and  $t$  is time. The driveshaft was driven by a high-torque digital servo motor (Dynamixel MX64), and its angle was verified by an absolute encoder (US Digital A2K 4096 CPR).

To test their near-ground performance, we pitched the hydrofoils near a vertical splitter plate in the closed-loop water channel (Figure. 3.1c). The splitter plate was used instead of the sidewall to control the boundary layer thickness. A boundary layer thickness of  $\delta_{99\%} \approx 7.5$  mm was measured using Particle Image Velocimetry at the position aligned with the leading edge of the hydrofoil. The incoming flow speed  $u$  was set to 143 mm/s using an ultrasonic flowmeter (Dynasonics Series TFXB). This speed gave a chord-based Reynolds number of 13500 (comparable to Blevins and Lauder, 2013, e.g., who tested a ray-inspired robot at  $Re \approx 10000$ ). The distance between the foil’s leading edge and the splitter plate,  $d$ , was controlled by an automated lateral traverse (Figure. 3.1c insert).

We tested each hydrofoil over a range of kinematics and ground proximities. For each

hydrofoil, we considered eight Strouhal numbers ( $St \equiv 2cf \sin \theta_0 / u$ ) between 0.2 and 0.55, five pitching amplitudes ( $\theta_0$ ) between  $7^\circ$  and  $15^\circ$ , and seventeen dimensionless ground proximities ( $d/c$ ) between 0.24 and 1.66. Combinations of  $St$ ,  $\theta_0$ , and  $d/c$  that would produce  $f \geq 2.5$  Hz or less than 10 mm ( $1.3 \delta_{99\%}$ ) distance between the trailing edge and the ground were omitted. Each trial was repeated three times. We measured forces with a six-axis force-torque sensor (ATI-Mini 40: SI-40-2 for  $\mathcal{R} > 1.5$ , SI-20-1 for  $\mathcal{R} \leq 1.5$ ), details of performance calculation can be found in section 2.3.2.

### 3.1.4 Simulating near-ground propulsion

To determine whether viscous effects played a significant role in our experiments, we ran potential flow simulations at overlapping conditions. The simulations had three purposes: (1) provide additional evidence for trends observed in the experiments, (2) determine which (if any) trends are sensitive to viscous effects, and (3) confirm that the boundary layer on the splitter plate (which does not exist in near-ground free-swimming/flying) has a negligible effect. The simulations use an unsteady 3D boundary element method that assumes irrotational, incompressible and inviscid flow. The method of images is used to model the presence of the ground [86]. The boundaries of the water channel were simulated based on the test section of the experiments for a fairer comparison. Equilibrium altitudes were determined by iterating  $d/c$  values until time-averaged lateral forces converged below a threshold range ( $C_L \leq 0.015$ ).

The workflow of the simulations is described in our previous work [84, 87], and a brief summary is given here. Potential flow is governed by Laplace's equation,  $\nabla^2 \phi' = 0$ , where  $\phi'$  is the perturbation potential in an inertial frame fixed to the undisturbed fluid. To approximate a solution for  $\phi'$ , the hydrofoil's surface, wall of the water channel, and the wake are modeled as discrete quadrilateral boundary elements. Each element contains a constant-strength doublet and source, and at each timestep, new wake elements are shed at the hydrofoil's trailing edge. Wake elements advect with the local velocity based on

a desingularized Biot-Savart law, as in [88], [89], and [87]. The evolving distribution of doublet/source strengths is determined by the Kutta condition (smooth flow at the trailing edge), Kelvin’s circulation theorem (constant global circulation), and the no-flux boundary condition ( $\nabla \phi' \cdot n_i = 0$ , where  $n_i$  is the normal vector of the  $i^{\text{th}}$  surface element). Once  $\phi'$  is known, the forces on the hydrofoil follow from the unsteady Bernoulli equation.

## 3.2 Results

### 3.2.1 Near-ground performance of two-dimensional hydrofoil

Figure 3.2a presents the lift coefficient measured from the constrained foil experiments at  $k = 1.02$  as a function of the ground distance and Strouhal number. Far from the ground ( $D^* \gtrsim 1$ ) there is negative time-averaged lift that acts to pull the foil towards the ground. Close to the ground ( $D^* \lesssim 1$ ) the foil produces positive lift that acts to push the foil away from the ground. At a ground distance between these two lift regimes, the time-averaged lift is zero. These zero-lift ground distances represent *stable* equilibrium altitudes,  $D_{\text{eq}}^*$ . If a foil is perturbed away from or towards the ground, lift forces would act to return the foil to the equilibrium altitude. Additionally, with increasing Strouhal number, the minimum and maximum lift force is amplified and the equilibrium altitude moves farther from the ground. These constrained foil experiments confirm the potential flow results presented by [28] and the existence of equilibrium altitudes shown by [21].

The equilibrium altitudes are determined by interpolating the lift data near the zero-lift ground distance with a cubic-spline function for each  $St - k$  case for the constrained two dimensional foil experiments. Figure 3.2b presents these equilibrium altitudes as a function of the Strouhal number and reduced frequency. Indeed, the equilibrium altitudes move farther from the ground as the Strouhal number increases for all of the reduced frequencies examined. In contrast, the equilibrium altitudes move closer to the ground as the reduced frequency increases.

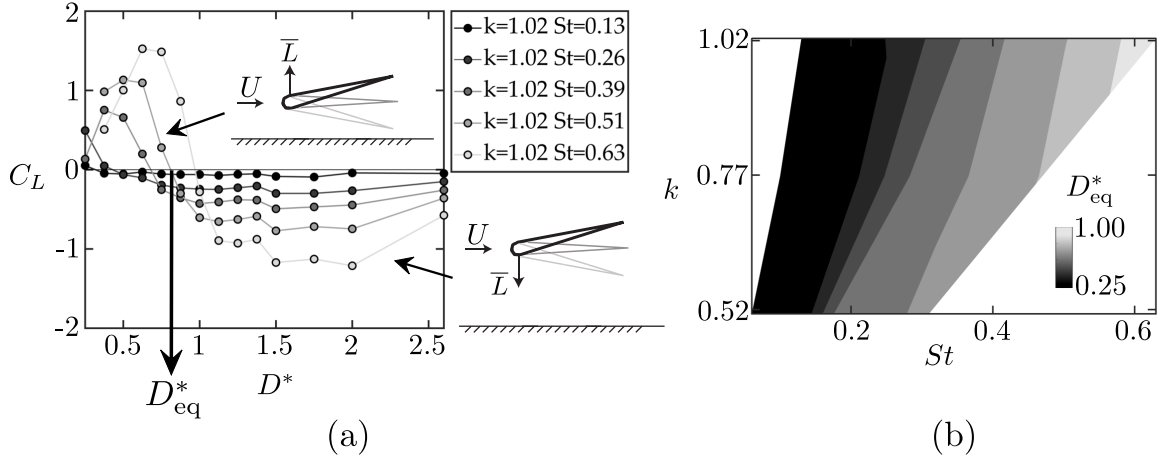


Figure 3.2: **Performance coefficients of two-dimensional hydrofoil:** (a) Lift coefficient as a function of the non-dimensional distance from the ground for  $k = 1.02$  and (b) equilibrium altitude as a function of the Strouhal number and reduced frequency. No data are shown in the regions colored with white. Experiment data took by [83] at the Lehigh University.

The constrained two-dimensional experiments suggest that equilibrium altitudes exist for unsteady ground effect swimmers, but they cannot prove whether or not dynamic recoil motions of a freely-swimming body alter the physics that give rise to these altitudes. To prove the existence of equilibrium altitudes for freely swimming foils, we tested two-dimensional hydrofoil that were free to move in the cross-stream direction. Figure 3.3 presents the two-dimensional hydrofoil's time-varying ground distance for  $St = 0.3$  and various reduced frequencies measured from the experiments and simulations. Regardless of the initial condition and the reduced frequency, the two-dimensional hydrofoil reaches an equilibrium altitude in both the experiments and the simulations. Moreover, the equilibrium altitudes measured from the experiments and predicted by the simulations are in excellent agreement ( $< 0.03$  disagreement in  $D_{eq}^*$ ). This agreement indicates that the physics of unsteady ground effect are dominated by inviscid phenomena. Additionally, the equilibrium altitude can be observed to move closer to the wall as the reduced frequency is increased, which is in agreement with the constrained two-dimensional hydrofoil experiments (Figure 3.2b). The two-dimensional hydrofoil's trajectory shows sinusoidal recoil oscillations in

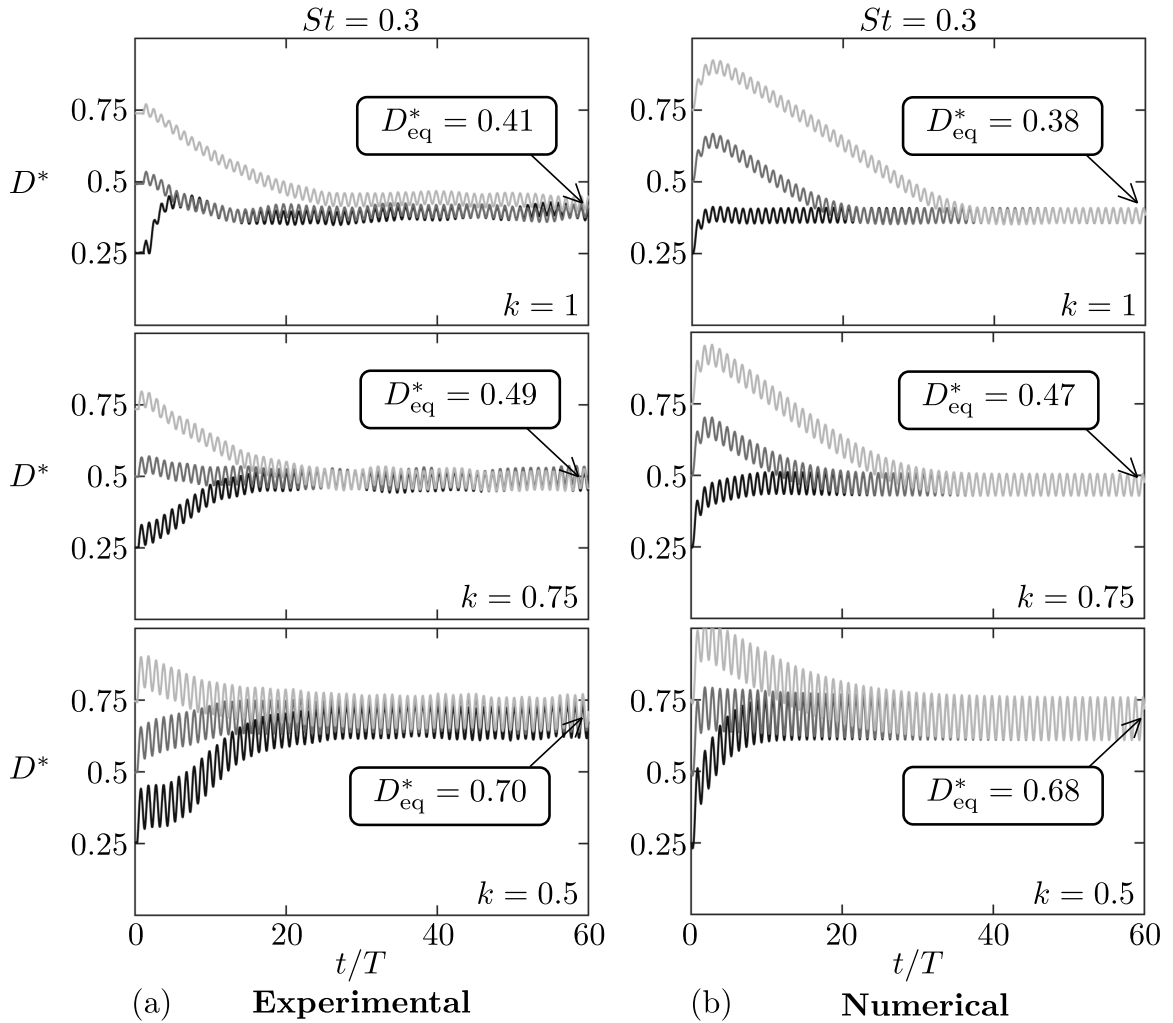


Figure 3.3: **Time-varying ground distance as a function of time normalized by the period of motion,  $T$ , for  $St = 0.3$ .** Data from (a) experiments and (b) simulations (simulation data took by [83] at the Lehigh University). The line color from black to light grey represents three different initial conditions:  $D^* = 0.25, 0.5$ , and  $0.75$ . Three reduced frequency cases of  $k = 0.5, 0.75$ , and  $1$  are presented.

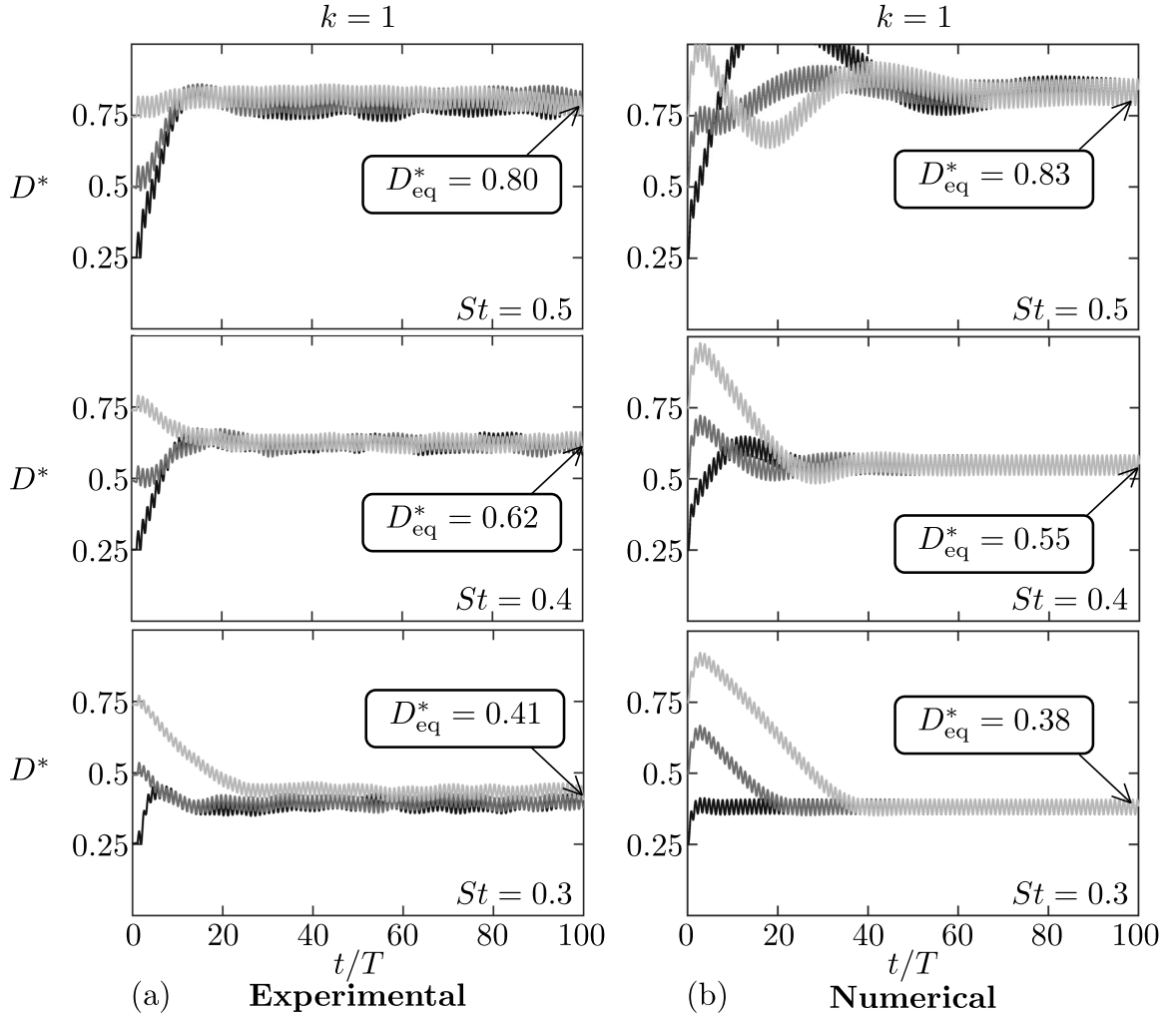


Figure 3.4: **Time-varying ground distance as a function of normalized time for  $k = 1$ .** Data from (a) experiments and (b) simulations (simulation data took by [83] at the Lehigh University). The line color from black to light grey represents three different initial conditions:  $D^* = 0.25, 0.5$ , and  $0.75$ . Three Strouhal number cases of  $St = 0.3, 0.4$ , and  $0.5$  are presented.

the cross-stream direction with each pitching cycle. The amplitude of these oscillations are slightly higher in the numerical results than the experimental measurements on the order of 10 – 20%. This can be attributed to viscous flow effects such as mild separation and/or end effects in the experiments that are not present in the simulations, which can lead to increased experimental damping. The recoil oscillations can be observed to grow with decreasing reduced frequency, which can be explained by increased pitching amplitude that occurs to maintain the Strouhal and Reynolds numbers among these cases.

Figure 3.4 presents the two-dimensional hydrofoil’s time-varying ground distance for  $k = 1$  and various Strouhal numbers measured from the experiments and simulations. Again, regardless of the initial condition, the two-dimensional hydrofoil converges to the same equilibrium altitude for all of the examined Strouhal numbers, and there is excellent agreement between numerics and experiments ( $< 0.07$  disagreement in  $D^*_{eq}$ ). In fact, the numerically predicted equilibrium altitudes are within 3 – 11% of the experimental measurements for all of the cases examined in Figures 3.3 and 3.4. As the Strouhal number increases, recoil oscillations increase and the equilibrium altitudes move further away from the ground, in agreement with the constrained two-dimensional hydrofoil experiments (Figure 3.2b). There is some disagreement between the simulations and experiments in the initial time-varying trajectories of the two-dimensional hydrofoil before an equilibrium altitude is reached.

### 3.2.2 Near-ground performance of high-aspect-ratio hydrofoils

The highest finite aspect ratio foil we considered ( $\mathcal{R} = 2.5$ ) shows similar trends as 2D near-ground hydrofoil in section 3.2.1. As expected, the time-averaged thrust is highest at high Strouhal numbers and low ground distances (Figure. 3.5a). As the foil moves away from the ground, thrust decreases and levels off, generally following the empirical scaling observed by [20] ( $\overline{F}_T \sim c_1[1 + (d/c)^{-0.4}]St^2$ ,  $R^2 = 0.97$ ) and the model-based scaling proposed by [90] ( $\overline{F}_T \sim [c_1 + c_2(d/c)^{-2}]St^2$ ,  $R^2 = 0.98$ ). Unlike thrust, efficiency peaks

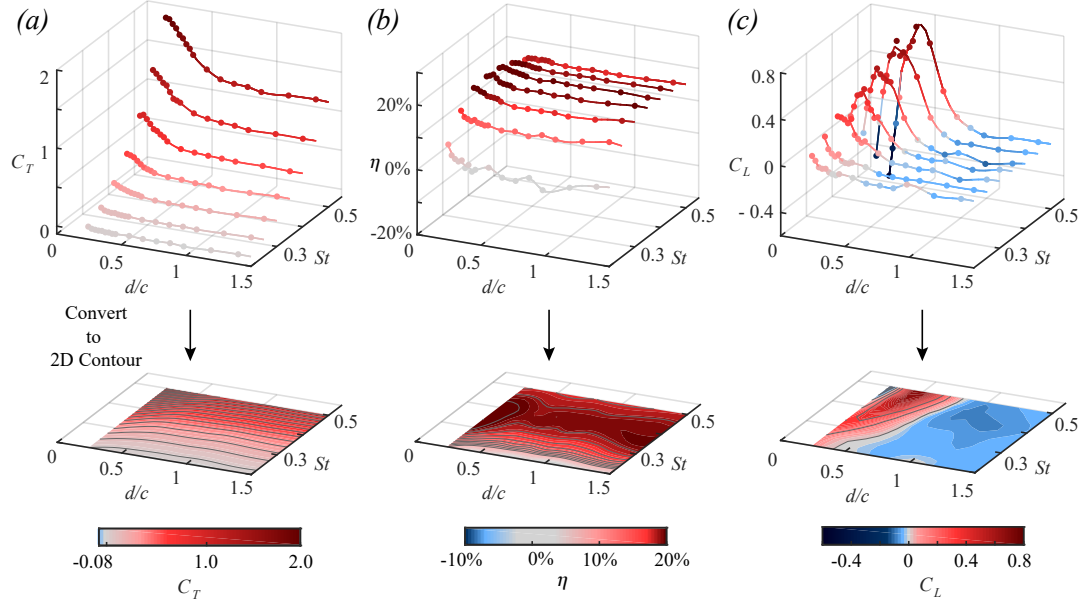


Figure 3.5: **Performance coefficients for  $\mathcal{R} = 2.5$  at  $\theta_0 = 9^\circ$ .** (a) Thrust coefficient ( $C_T \equiv \overline{F}_T / (0.5\rho u^2 sc)$ ) peaks at high Strouhal numbers ( $St$ ) and low ground distances ( $d/c$ ). (b) Efficiency ( $\eta$ ) peaks at intermediate  $St$  and shows little dependence on  $d/c$ . (c) Lift coefficient ( $C_L \equiv \overline{F}_L / (0.5\rho u^2 sc)$ ) can be positive or negative, leading to equilibrium altitudes where  $C_L = 0$ .

at an intermediate Strouhal number and has only modest increases near the ground (+1%-3%; Figure. 3.5b). The implication is that for the same input kinematics, a hydrofoil can produce higher free-swimming speeds and accelerations near the ground without sacrificing efficiency.

The  $\mathcal{R} = 2.5$  hydrofoil also reproduces the equilibrium altitudes observed in two-dimensional case. Far from the ground, lift is negative; closer to the ground, lift becomes positive (Figure. 3.5c). Between these two lift regimes is a stable equilibrium altitude into which an untethered, open-loop, symmetrically-actuated hydrofoil would settle. As  $St$  increases, the positive lift magnitudes are amplified, leading to a more stable and higher equilibrium altitude ( $d/c$  rises from 0.55 to 0.85 as  $St$  rises from 0.2 to 0.5). This positive shift with  $St$  is consistent with previous work on 2D foils and confirms that equilibrium altitudes exist for finite aspect ratios.

We also observed a second set of equilibrium altitudes very close to the ground ( $d/c < 0.35$ ; Figure. 3.5c). Unlike the lift near the stable equilibria, the lift here is increasing

with  $d/c$ . Just above equilibrium, positive lift pushes the hydrofoil away from the ground; just below equilibrium, negative lift sucks the hydrofoil towards the ground. The result is an unstable equilibrium. The instability is considerable: lift changes rapidly ( $\Delta C_L \approx 1$ ) over a narrow range ( $\Delta d/c \approx 0.1$ ;  $\Delta d \approx 10$  mm). Unstable near-ground equilibria have been hypothesized in our previous two-dimensional study [83], but here they are shown experimentally for the first time. The effect only appears at high Strouhal numbers ( $St \geq 0.4$ ) and low  $d/c$  values, which helps to explain why they are difficult to observe.

Pitching amplitude also affects performance near the ground. At low Strouhal numbers, smaller amplitudes lead to higher net thrust, presumably because of the smaller projected area ( $cs \sin \theta_0$ ; Figure. 3.6a). At high Strouhal numbers, amplitude has relative smaller effect on absolute thrust but does affect near-ground thrust enhancement ( $\Delta C_T = 0.58$  for  $\theta_0 = 9^\circ$  vs.  $\Delta C_T = 0.35$  for  $\theta_0 = 15^\circ$  at  $St = 0.5$ ). Following thrust, efficiency was also higher at lower amplitudes (Figure. 3.6b). For example, at a representative case far from the ground ( $St = 0.3$ ;  $d/c = 1.66$ ), efficiency was 6.0% for  $\theta_0 = 15^\circ$  vs.  $\eta = 18.7\%$  for  $\theta_0 = 9^\circ$ . Moreover, the equilibrium altitude decreased from 0.93 to 0.82 at lower amplitudes ( $\theta_0 = 15^\circ$  to  $\theta_0 = 9^\circ$ ; Figure. 3.6c).

### 3.2.3 Near-ground performance of low-aspect-ratio hydrofoils

In general, we found that as aspect ratio decreases, so do the effects of the ground. For example, in otherwise identical conditions ( $d/c = 0.35$ ,  $St = 0.55$ ,  $\theta_0 = 15^\circ$ ), the  $\mathcal{R} = 2.5$  hydrofoil's thrust was boosted by  $+41\% \pm 1\%$ , compared to only  $+18\% \pm 3\%$  when  $\mathcal{R} = 1$  (Figure. 3.6a). To consider the bulk performance of each aspect ratio, we averaged the thrust boosts across all sets of kinematics for each aspect ratio. On average, the ground amplified thrust more than twice as much when  $\mathcal{R} = 2.5$  than it did when  $\mathcal{R} = 1.0$  (Figure. 3.6b). The regime where thrust was amplified ( $d/c \lesssim 0.75$ ) was similar across the four aspect ratios.

The ground's effect on efficiency was less sensitive to aspect ratio (Figure. 3.6c-d).

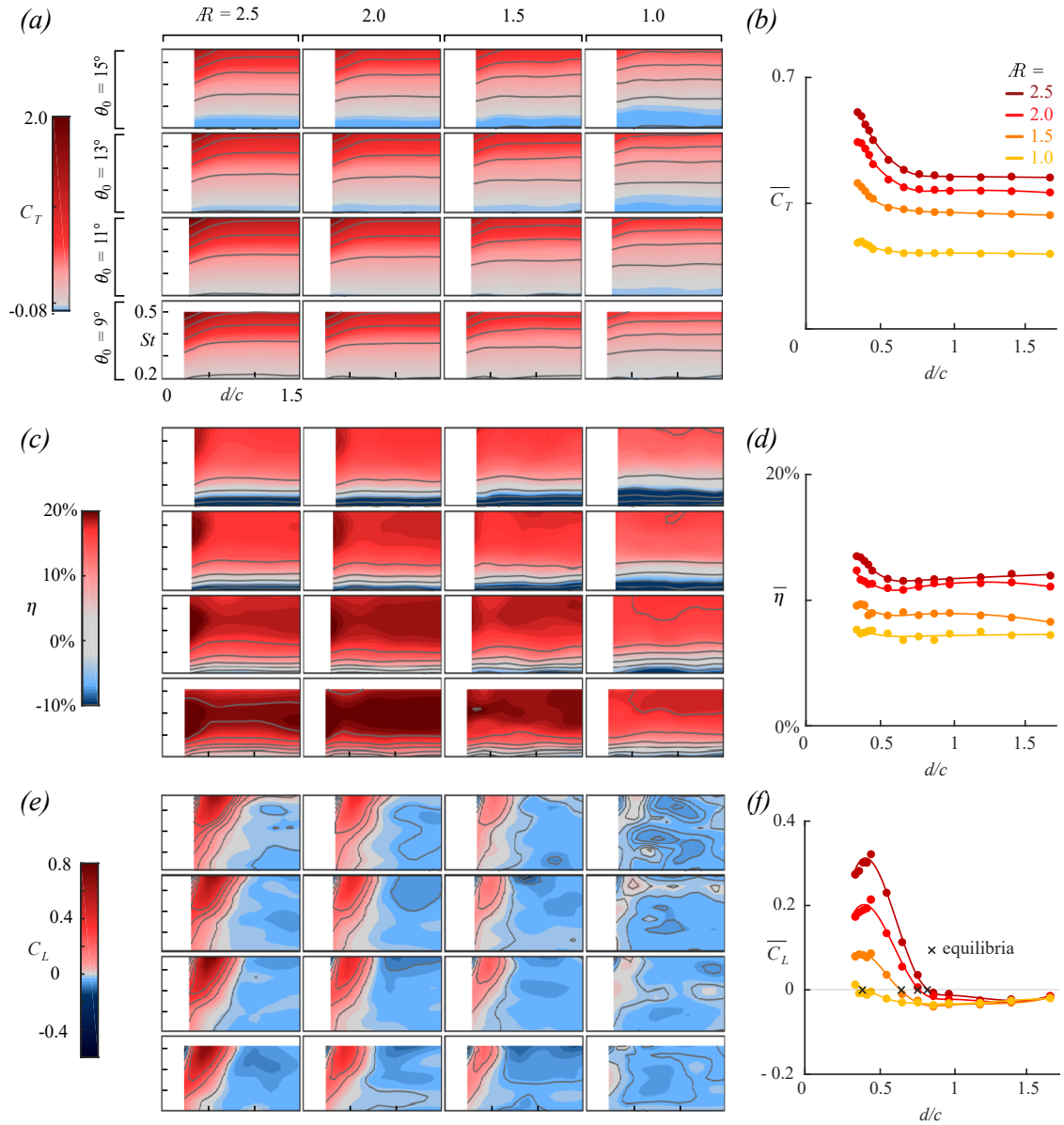


Figure 3.6: **Performance coefficients for  $\mathcal{R} = 1, 1.5, 2, 2.5$ .** (a,c) Thrust coefficient (a) and efficiency (c) show similar trends as aspect ratio decreases, with a slight decrease at higher pitch amplitudes and lower aspect ratios. (e) Lift coefficient ( $C_L$ ) shows changing trends as aspect ratio decreases: positive lift values and equilibrium altitudes decrease in magnitude. (f) (b,d,f) The performance coefficients for each  $d/c$  and  $\mathcal{R}$  combination, averaged across all  $St$  and  $\theta_0$  cases, reveal the dominant effects of changing aspect ratio. Ground proximities with only partial amplitudes were omitted in bulk averaging to make fair comparison.

Lower aspect ratios led to lower efficiencies, presumably due to tip vortices and induced drag (see e.g. [91]). However, the effect of ground proximity was similar across all aspect ratios: efficiency stayed mostly constant, with a 1-3% rise near the ground ( $d/c \lesssim 0.5$ ). (Figure. 3.6d).

Unlike thrust and efficiency, the lift—and therefore the equilibrium altitude—is significantly affected by aspect ratio (Figure. 3.6e-f). As the aspect ratio decreases, the near-ground regime of positive lift shrinks, and the equilibrium altitude shifts toward the ground (average equilibrium  $d/c$  drops from 0.8 to 0.35, Figure. 3.6f). When  $\mathcal{R} = 1$ , the positive lift regime is so small that the equilibrium altitude vanishes at low Strouhal numbers, though it persists when  $St \geq 0.35$ .

The second unstable equilibrium altitude is less sensitive to aspect ratio. Because the equilibria occur over a small band of high Strouhal numbers and very close to the ground, they do not appear in averaged lift trends (Figure. 3.6f). To better understand the unstable equilibria, we therefore plotted  $C_L$  near the ground at a high Strouhal number (Figure. 3.7a). The unstable equilibria are mostly unaffected by aspect ratio, varying over only a narrow range ( $d/c = 0.28 \sim 0.3$ ). The unstable equilibria shift slightly higher with increasing amplitude and Strouhal number (Figure. 3.6b,c), but differences due to aspect ratio remain small. Note that the unstable equilibria start to disappear at high aspect ratio and high amplitude (Figure. 3.7b).

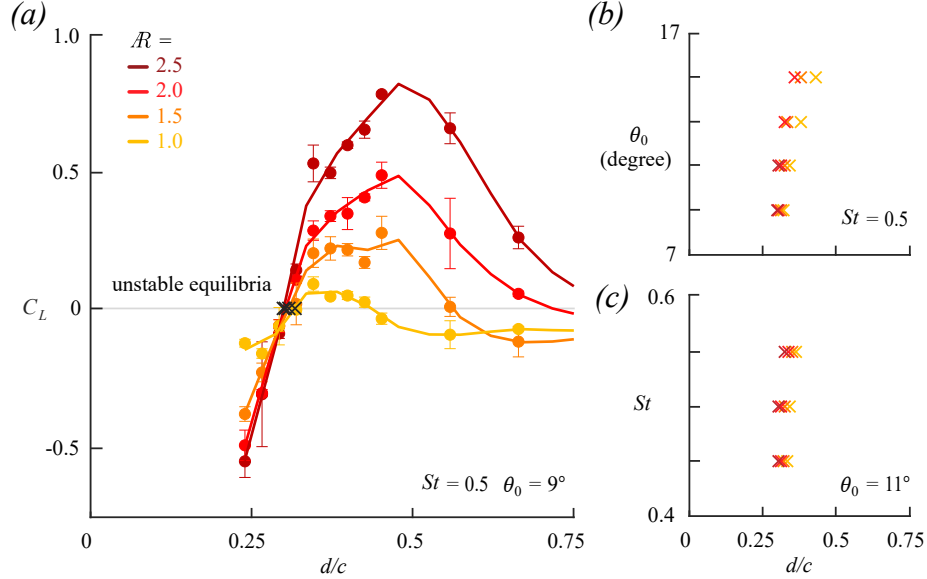


Figure 3.7: **Near-ground unsteady equilibria are less sensitive to aspect ratio than stable equilibria.** (a) Aspect ratio affects the location and magnitude of maximum lift, but it has little effect on the unsteady equilibrium altitude. (b) For a fixed Strouhal number, the unsteady equilibrium altitude slightly increases with larger amplitude. (c) For a fixed amplitude, the unsteady equilibrium altitude slightly increases with larger Strouhal number.

### 3.2.4 Comparing simulations and experiments

Comparing potential flow simulations with our experiments confirms that viscosity likely plays a minor role in unsteady ground effects at high Reynolds numbers and moderate Strouhal numbers ( $St = 0.25, 0.35$ ). As in the experiments, the simulations show that lower aspect ratios lead to weaker lift forces and lower equilibrium altitudes (Figure. 3.8a). In both cases, the equilibrium altitude drops by  $\approx 0.2$  chord lengths as  $\mathcal{R}$  falls from 2.5 to 1.5. Like the experiments, the simulations predict a vanishing equilibrium as aspect ratio approaches 1 at low Strouhal numbers ( $\mathcal{R} < 1.3$ , Figure. 3.8a). We also performed simulations at high Strouhal number ( $St = 0.5, \theta_0 = 9^\circ$ ) close to the ground to explore the unsteady equilibria. The simulations reproduced unsteady equilibria at high aspect ratios ( $d/c = 0.274$  for  $\mathcal{R} = 2.5$ ;  $d/c = 0.287$  for  $\mathcal{R} = 2.0$ ) but not low aspect ratios ( $\mathcal{R} \leq 1.5$ ).

Our potential flow simulations also predict a rise in thrust near the ground, as they have previously [22]. As in the experiments, the simulations predict that higher aspect-

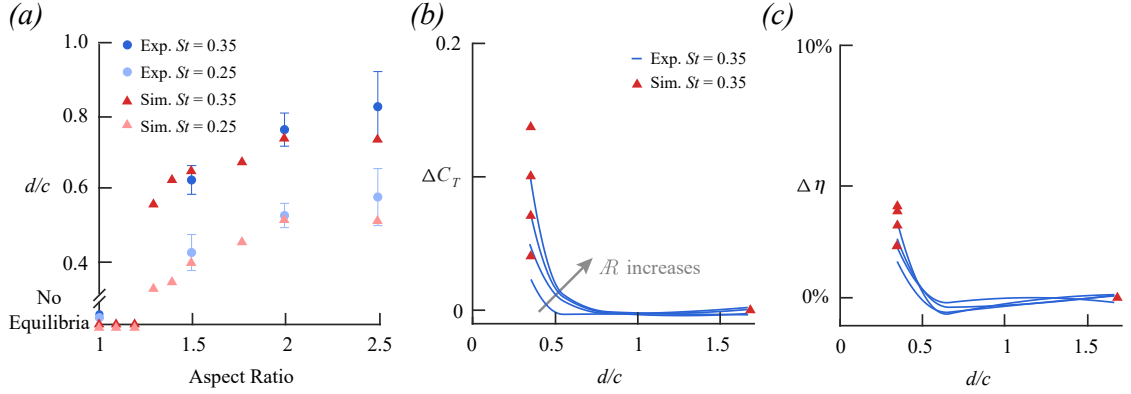


Figure 3.8: **Comparison between experiment and potential flow simulation.**(a) Both experiments and simulations show that stable equilibrium altitude increases with aspect ratio. No equilibria were found for the lowest aspect ratio cases at the Strouhal numbers of the simulations (0.25 and 0.35).(b) Relative change of time-averaged thrust coefficients ( $\Delta C_T$ ) at  $St = 0.35$ ,  $\theta_0 = 15^\circ$ . (c) Relative change of time-averaged efficiency ( $\Delta \eta$ ) at  $St = 0.35$ ,  $\theta_0 = 15^\circ$ .

ratio foils experience a larger boost in thrust near the ground ( $\Delta C_T = 0.14$  at  $\mathcal{AR} = 2.5$  vs.  $\Delta C_T = 0.046$  at  $\mathcal{AR} = 1.0$ ) (Figure. 3.8b). However, the absolute thrust coefficient was consistently overestimated by the simulations (by about 0.21 ~ 0.25 for each aspect ratio). The discrepancy is presumably due to the absence of skin-friction drag and leading-edge separation in the simulations.

Efficiency trends show similar patterns as thrust trends. The efficiency in the simulations stays mostly constant, then increases by 3%-5% when  $d/c \leq 0.5$  (Figure. 3.8c). Because the simulations over-predict absolute thrust, they also over-predict efficiency ( $\eta \equiv \overline{F_T u} / \overline{\tau_z \theta}$ ). As in previous work [20], the simulations underestimate power input to the fluid (at least at  $St = 0.35$ ), which further increases the absolute efficiency magnitude. Nevertheless, simulations and experiments predict comparable relative changes in efficiency ( $\Delta \eta = 1\text{-}5\%$ ) as the foil approaches the ground.

### 3.2.5 Near-ground wakes of high- and low-aspect-ratio foils

To explore how aspect ratio affects the near-ground wake, we measured the flow around two hydrofoils ( $\mathcal{AR} = 1$  and  $\mathcal{AR} = 2$ ) in and out of ground effect ( $d/c = 0.5$  and  $d/c = 1.8$ ).

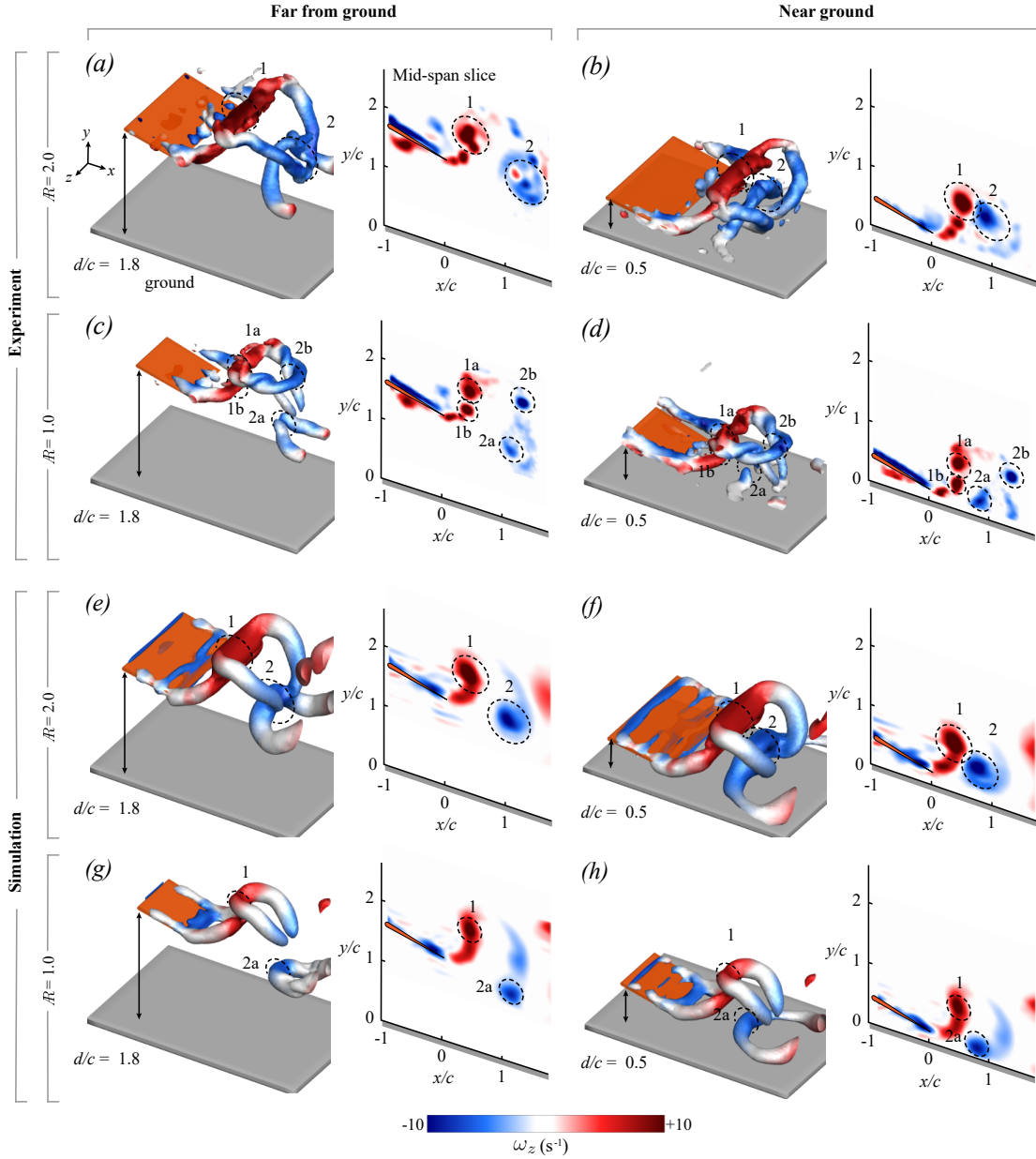


Figure 3.9: **Aspect ratio affects wake topology near the ground.** Wakes from experiments (*a-d*) and simulations (*e-h*) are shown at the same phase (trailing edge closest to the ground). Wake structures are visualized with iso-surfaces of  $Q$ -criterion ( $Q = 5 \text{ s}^{-2}$ ) colored by spanwise vorticity ( $\omega_z$ ). Sideplots show spanwise vorticity at a mid-span slice of the 3D wake. (*a,b*) Experiments:  $AR = 2$  hydrofoil far from and near to the ground. (*c,d*) Experiments:  $AR = 1$  hydrofoil far from and near to the ground. (*e,f*) Simulations:  $AR = 2$  hydrofoil far from and near to the ground. (*g,h*) Simulations:  $AR = 1$  hydrofoil far from and near to the ground.

Far from the ground, the higher aspect ratio foil sheds a 2S reverse von Kármán vortex street at its mid-span (Figure. 3.9a). This classic mid-span wake has been observed in several previous studies, e.g. the soap film visualizations of [6]. Here we show how this 2S wake fits into the full 3D wake behind the foil. Each half-cycle, streamwise tip vortices and a spanwise trailing edge vortex are shed as a loop. As the loop advects into the wake, its downstream end wraps around the upstream end of the previous loop, forming one of the spanwise vorticity cores of the 2S wake (Vortex 2 in Figure. 3.9a). Similarly interconnected loops have been seen behind trapezoidal panels at comparable Reynolds numbers [92], rectangular foils at low Reynolds numbers (Von Ellenrieder, Parker, and Soria, 2003  $Re = 164$ ; Buchholz and Smits 2008,  $Re = 640$ ), and simulations of rectangular and elliptical foils [91, 95].

Near the ground, half of the von Kármán vortices are slowed by the ground, causing the vortex street to clump into vortex pairs that mutually advect upward (Figure. 3.9b). These paired vortices were seen behind near-ground 2D pitching foils [20], and here we show how they fit into a larger 3D wake. Each half-cycle produces a vortex loop, as it does far from the ground. The vortex loop nearer to the ground attaches to the ground and is slowed by the ground, creating an arch of vorticity that interacts with the next vortex loop. As in the free-stream case, the downstream end of the next vortex loop curls and wraps around the previous loop, but now the effect is more pronounced, creating spanwise vortex cores that pair together (Vortices 1 and 2 in Figure. 3.9b).

Compared to the higher aspect ratio hydrofoil, the  $\mathcal{R} = 1$  foil generates a more complicated wake (Figure. 3.9c). A mid-span slice shows that where two vortex cores had been for  $\mathcal{R} = 2$ , there are now four cores. The 3D wake reveals the source of the complexity: the tip vortices, which are now almost as prominent as the trailing edge vortices, create a train of intertwined horseshoe vortices instead of a series of coherent loops. The legs of these horseshoe vortices remain coherent, leading to the extra vortex cores in the mid-span slice. These results—particularly the role of streamwise vorticity in driving the horseshoe

vortex entanglement—confirm and expand upon the dye visualizations of [94] ( $\mathcal{R} = 1.11$ ,  $Re = 640$ ).

Near the ground, the wake of the  $\mathcal{R} = 1$  hydrofoil was less perturbed than the  $\mathcal{R} = 2$  hydrofoil (Figure. 3.9*b,d*). This is surprising, because tip vortices play a key role in steady ground effect [96], so one might expect that the wake of the  $\mathcal{R} = 1$  foil (where tip vortices are more influential) would be more affected by the ground. However, it appears that because the 2S vortex cores are split (Vortex 2 into 2a and 2b; Figure. 3.9*a,c*), only Vortex 2a experiences a strong slowing effect from its image vortex. In contrast, Vortex 2b follows a similar advection path as it does far from the ground. The 3D plot shows that the near-ground vortex ring does not twist and collapse as it does in the  $\mathcal{R} = 2$  case; instead, the ring expands and dissipates, similar to the expansion seen by [27] behind a near-ground flexible panel ( $\mathcal{R} = 2$ ,  $Re = 100$ ).

Our simulations revealed similar wakes as the experiments, suggesting that the near-ground wake is governed largely by inviscid phenomena (Figure. 3.9*e-h*). A notable exception is the mid-span wake behind the  $\mathcal{R} = 1$  foil, where the distinction between Vortices 1b and 2b becomes less clear. Some vortex smearing in the simulations is expected due to the wake desingularization. In addition, the simulations only shed wake elements at the trailing edge, so the tip vortices—which play an active role in deforming the experimental wakes—are weaker in the simulations. Nevertheless, the simulations still capture the main trends of the wake, including the weaker vortex pairing in the  $\mathcal{R} = 1$  case.

### 3.3 Discussion

For the first time, it is experimentally confirmed that freely swimming pitching foils converge to stable equilibrium altitudes. When the foils are far from the ground, negative lift forces pull them towards the ground; when the foils are close to the ground, positive lift forces push them away from the ground. These equilibrium altitudes are insensitive

to initial altitude. Furthermore, the equilibria are dependent on swimming kinematics: in both constrained and unconstrained cases, equilibrium altitudes increase with increasing Strouhal number and decreasing reduced frequency. When very close to the ground, the asymmetric lift drops from positive to negative within a small distance, leading to another unstable equilibrium altitude. Unlike the stable equilibria, foils are hard to stable at this unstable equilibria.

Based on results of finite aspect ratio foils, we found that unsteady ground effect is weaker for lower aspect ratio hydrofoils. The average thrust enhancement at  $d/c = 0.35$  was 44% for  $\mathcal{R} = 2.5$  compared to 18% for  $\mathcal{R} = 1.0$  (Figure. 3.6b). This difference is not simply caused by the difference in area; we reran the  $\mathcal{R} = 2.5$  trials with a reduced chord length ( $0.8c$ ), and thrust enhancements changed by less than 5%. Lower aspect ratio foils also produced less asymmetric lift, causing equilibrium altitudes to weaken and shift toward the ground (Figure. 3.6f). The equilibrium for the  $\mathcal{R} = 1$  foil was not even detectable at low enough Strouhal numbers. These results are consistent with the near-ground wakes we observed, where the ground had a smaller effect on the wake of the  $\mathcal{R} = 1$  foil. Furthermore, vortex-induced drag is known to be a key contributor to streamwise forces on low-aspect-ratio foils [97], so ground effect may play a minor role in low-aspect-ratio hydrofoil dynamics at low Strouhal numbers. This effect may help explain the findings of [85], who found no appreciable performance changes for a stringray-inspired robot ( $\mathcal{R} = 0.5$ ) swimming near the ground at  $St = 0.13$ .

By comparing experiments and potential flow simulations, we found that unsteady ground effects are primarily inviscid phenomena over the conditions we tested. For  $\mathcal{R} \geq 1.3$ , our results suggest that viscosity plays only a minor role in determining equilibrium altitude, which extends previous findings on 2D hydrofoils [83]. However, viscosity reduces relative thrust and efficiency enhancements near the ground, and its role becomes less clear at lower aspect ratios ( $\mathcal{R} < 1.3$ ). Although potential flow simulations confirmed that equilibrium altitudes decrease and vanish as  $\mathcal{R}$  decreases, we did observe noticeable differ-

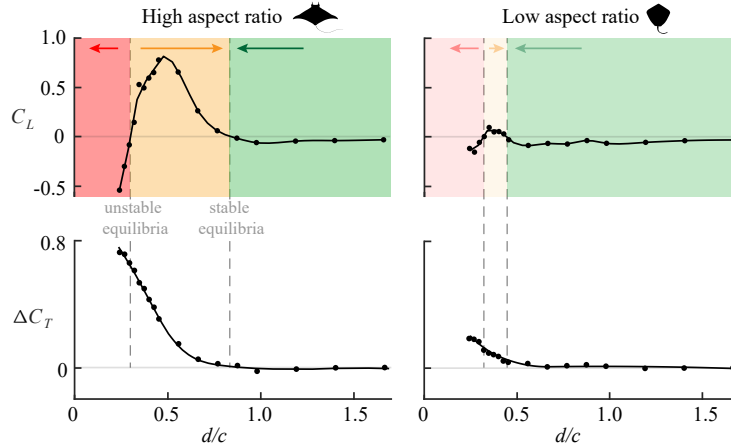


Figure 3.10: **Low aspect ratio foils can more easily reach high-thrust regions.** Sample case shown is  $St = 0.5$  and  $\theta_0 = 9^\circ$ . Fish avatars: Manta ray  $\mathcal{A}R \approx 2.3$  [100] and Atlantic stingray  $\mathcal{A}R \approx 1.0$  [29]. Shaded regions denote the presence of a downward force towards a stable equilibrium (green), an upward force towards a stable equilibrium (yellow), or a downward force towards the ground (red), with color intensity meant to suggest the difficulty of maintaining a steady ground proximity.

ences in wake details due to the absence of viscosity in the  $\mathcal{A}R = 1$  case (Figure. 3.9c,d,g,h).

The fact that lower aspect ratios cause lower equilibrium altitudes can be explained with known scaling laws of pitching hydrofoils. In the case of 2D near-ground hydrofoils, asymmetric added mass forces decrease the equilibrium altitude, while asymmetric circulatory forces increase the equilibrium altitude [83]. The former effect can be explained by near-ground added mass coefficients [98], and the latter effect by the image vortex system [96]. In the case of finite-span hydrofoils, added mass and circulatory forces are reduced by factors of  $\mathcal{A}R/(\mathcal{A}R + 1)$  and  $\mathcal{A}R/(\mathcal{A}R + 2)$ , respectively [99, 98], leading to a ratio between the two of  $(\mathcal{A}R + 2)/(\mathcal{A}R + 1)$ . Therefore, as the aspect ratio decreases, added mass forces become more dominant, which may explain why the net effect is a decrease in equilibrium altitude (Figure. 3.6f).

# Chapter 4

## Pitching Propulsor: Fish Inspired

### Maneuver

In this study, we used a semi-autonomous rig that has some elements of autonomous robots and some of tethered platforms. Our goal was not to replace either but rather to capitalize on some of the benefits of both. We suspended an oscillating hydrofoil from two axes of air bushings to allow both streamwise and lateral recoils during fish-inspired maneuvers. Our rig cannot reproduce the 3D dynamics of fully autonomous propulsors, but it does offer the first force and flowfield measurements for propulsors freely recoiling in two directions. We present results for two streamwise and two lateral maneuver types: 1) an increase in amplitude, 2) an increase in frequency, 3) an increase in spatial asymmetry, and 4) an increase in temporal asymmetry. For each maneuver type, we quantify the dynamics and the surrounding flowfield, then discuss their implications for fish and fish-inspired robot maneuvers.

#### **4.0.1 A wireless carriage with a pitching hydrofoil**

To study the dynamics of maneuvers, we suspended oscillating hydrofoils from a wireless carriage that slides freely in a horizontal plane (Figure.4.1 *a*). To align our setup with

Table 4.1: Maneuver test parameter specifications.

Maneuver direction	Parameters	Values	Unit
Streamwise	Amplitude modulation $\theta_0$	10,12,14,16,18	degree
	Frequency modulation $f$	1.5,1.75,2.0,2.25,2.5,2.75,3.0	Hz
Lateral	Spatial asymmetry $\theta_{bias}$	0,1.0,1.5,2.0,2.5,3.0	degree
	Temporal asymmetry $\beta$	0.0001,0.15,0.3,0.45,0.6,0.75,0.9	

previous work (chapter. 3), we used 3D-printed teardrop-shaped hydrofoils with a chord ( $c$ ) of 95 mm and span ( $w$ ) of 143 mm (aspect ratio 1.5). The hydrofoils swam in a close-loop water channel with a  $L:1520 \text{ mm} \times W:380 \text{ mm} \times H:450 \text{ mm}$  test section. An incoming flow speed of  $u = 300 \text{ mm/s}$  was regulated by a custom circuit (Arduino Mega with a signal amplifier) and an ultrasonic flow sensor (Dynasonics Series TFXB). The carriage and its supporting frame consist of three major subsystems: a two-axis air suspension system (see section 2.1.2), a pitch actuator (see section 2.1.3), and an automated tilt system (see section 2.1.5).

To maximize the repeatability of the maneuver trials, we used an automated carriage reset system (Figure.4.1 *d*). The reset system used a horizontal traverse to automatically align a grabber with the  $x$  position of the hydrofoil (as recorded by the laser distance sensor on the carriage). In between trials, the grabber brought the hydrofoil back to its starting position. The reset system allows maneuver tests that are autonomous yet repeatable.

## 4.0.2 Streamwise/lateral maneuvers

To parameterize the hydrofoil maneuvers, we developed a function for pitch angle that captures the four maneuver types we studied. The function for pitch angle is

$$\theta(t) = \theta_{\text{bias}} + \theta_0 \frac{\tan^{-1}\left(\frac{\beta \sin 2ft}{1 - \beta \cos 2ft}\right)}{\tan^{-1}\left(\frac{\beta}{\sqrt{1 - \beta^2}}\right)},$$

where  $\theta_0$  is pitching amplitude,  $f$  is pitching frequency,  $\theta_{\text{bias}}$  is pitch bias angle, and  $\beta$  is stroke speed ratio. The bias angle,  $\theta_{\text{bias}}$ , sets the average pitch angle within an oscillation cycle and initiates lateral maneuvers via spatial asymmetry. The stroke speed ratio,  $\beta$ , sets the ratio of clockwise and counterclockwise pitch velocities and initiates lateral maneuvers via temporal asymmetry (Figure.4.4 *a*).

We chose a range of maneuver parameters based on our system's performance limits and observations from biology (table 1). We chose as a control case a symmetric motion with a moderate Strouhal number ( $\theta_0 = 10^\circ$ ,  $f = 1.5$  Hz,  $\theta_{\text{bias}} = 0$ , and  $\beta = 0.0001$ ;  $St = 2fc \sin \theta_0 / u = 0.16$ ). With those baseline kinematics, the hydrofoil produced just enough thrust to offset the incoming flow ( $u = 300$  mm/s), meaning there was negligible stream-wise and lateral displacements even when the hydrofoil's carriage was gliding on the air bushings. Maneuvering motions were defined in relation to those baseline kinematics. For example, in a test that considered a stroke speed ratio of 0.9, the three parameters besides stroke speed ratio took on their baseline values ( $\theta_0 = 10^\circ$ ,  $f = 1.5$  Hz,  $\theta_{\text{bias}} = 0$ , and  $\beta = 0.9$ ).

All maneuver tests started from steady swimming. Each trial started with the carriage reset system releasing the hydrofoil in the center of the test section. Simultaneously, the hydrofoil started three cycles of the baseline symmetric motion. Next, the hydrofoil performed three cycles that smoothly vary from the baseline motion to the maneuvering motion. Finally, 10 pitching cycles were recorded as the "maneuver". After the maneuver

was complete, large pitch angles were introduced to amplify drag and push the hydrofoil back to where it could be intercepted by the gripper of the carriage reset system. The reset system then brought the hydrofoil back to its starting position, and the process repeated. We repeated each test condition five times.

### **4.0.3 Performance metrics and flow fields**

We quantified the performance of the hydrofoil based on its kinematic response and the forces it exerted on the water. Kinematics ( $x(t)$  and  $y(t)$ ) were recorded with the laser distance sensors, and forces were recorded with a six-axis force/torque sensor in line with the driveshaft (ATI Inc., Mini-40). The resolutions of the force/torque sensor were sufficient to resolve the differences between trials: force resolution was  $\pm 0.01$  N along the  $y$  and  $x$  axes, and the torque resolution was  $\pm 0.25$  Nmm. The resolution of lasers sensors were  $\pm 0.05$  mm on streamwise direction and  $\pm 0.01$  mm on lateral direction.

Because previous studies have considered the wakes of pitching hydrofoils with varying amplitudes and frequencies [101, 6], we chose to focus our wake study on lateral maneuvers. We quantified the wake with Particle Image Velocimetry (PIV) done at the mid-span of the hydrofoils. Details is described in section 2.2.1.

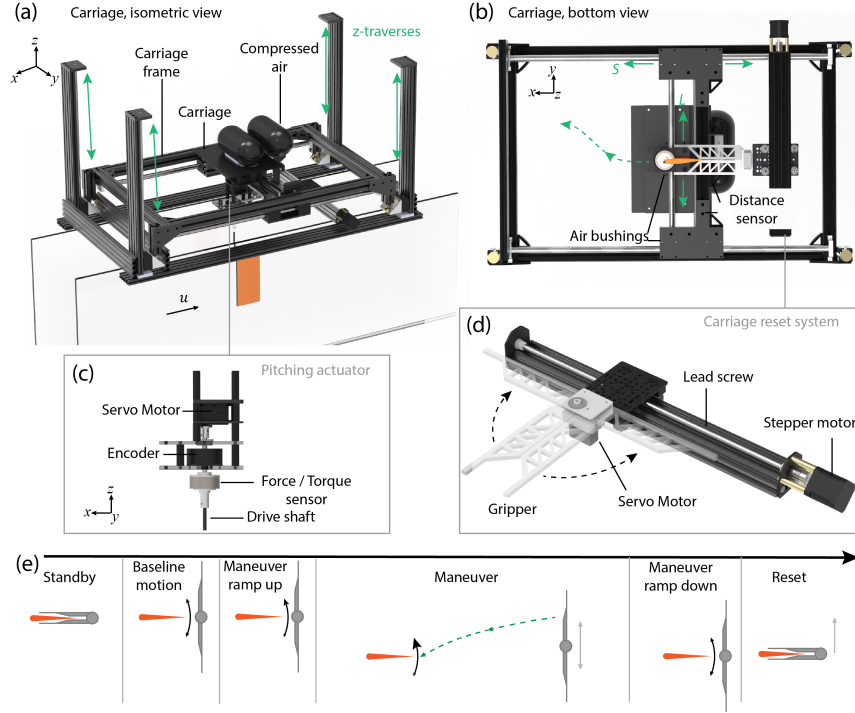


Figure 4.1: **A wireless experimental rig for studying bio-inspired maneuvers.** (a) A carriage gliding on air bushings suspended a hydrofoil into the center of a water channel. Four stepper motors (z-traverses) auto-level the carriage frame. (b) Six air bushings provide the carriage with streamwise (s) and lateral (l) freedom. (c) Pitching motions are generated by a servo motor; driveshaft dynamics are recorded by a force/torque sensor and encoder. (d) The carriage reset system uses a linear actuator and a servo-driven gripper to reset the carriage in between trials. (e) Visualization of a maneuver test trial. Each step was performed automatically by an online control PC.

## 4.1 Results

### 4.1.1 Bulk performance of streamwise maneuvers

We first consider the bulk performance of streamwise maneuvers, i.e. the general dynamics of the hydrofoil over the 10 pitching cycles of the maneuver. As expected, increasing frequency and amplitude both led to streamwise displacements (Figure.4.2 b). The displacements due to increasing frequency tended to be much larger than those due to increasing amplitude. For example, increasing frequency to 2.75 Hz caused a displacement of  $\Delta y = 11.3 \pm 0.7$  mm. Producing the same Strouhal number ( $St \approx 0.3$ ) by instead in-

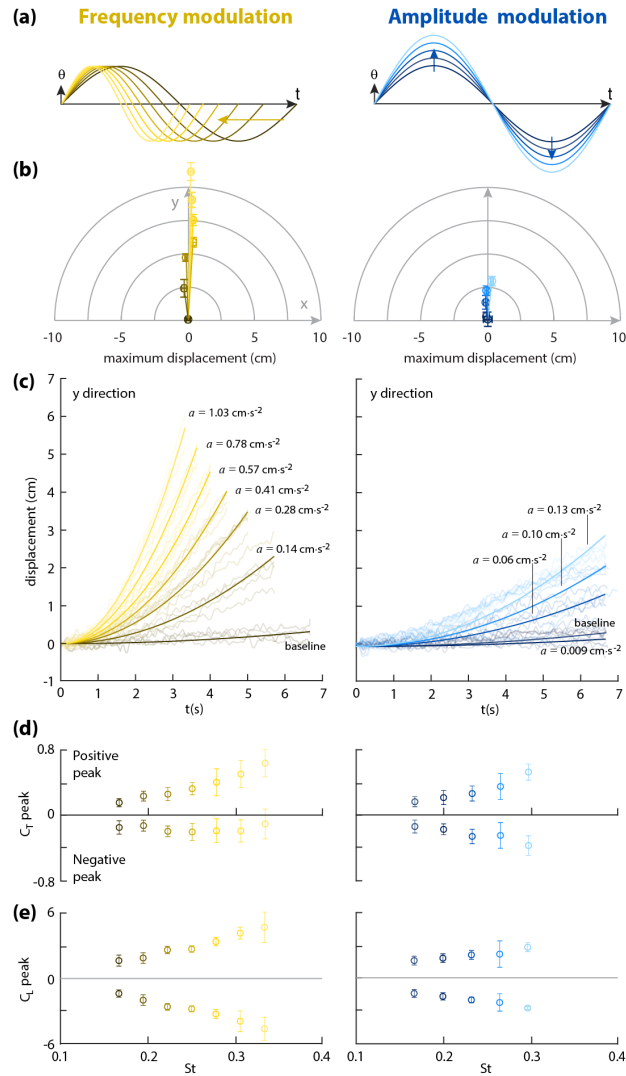


Figure 4.2: **Bulk performance of streamwise maneuvers.** (a) Pitching motion profiles. (b) Displacement in the s-l plane after the 10-cycle maneuver. (c) Time-history of streamwise displacement during the maneuver. Light lines: raw data; dark lines: fitted parabolas. (d) Streamwise force peak magnitudes. (e) Lateral force peak magnitudes.

creasing amplitude ( $f = 1.5$  Hz;  $\theta_0 = 18^\circ$ ) only caused a displacement of  $\Delta y = 2.6 \pm 0.3$  mm.

In addition to causing higher displacements, the frequency-driven maneuvers took less time. This combination led to much larger accelerations. The time-histories of streamwise displacements reveal that the hydrofoil accelerated at a nearly constant rate ( $R^2 > 0.95$  for quadratic fits; Figure.4.2 *c*). At the same Strouhal number, this constant rate was  $7.8 \text{ mm/s}^2$  for increased frequency ( $f = 2.75$  Hz) while only  $1.3 \text{ mm/s}^2$  for increased amplitude ( $\theta_0 = 18^\circ$ ). The magnitude of the acceleration ( $\dot{y}$ ) scaled linearly with amplitude and quadratically with frequency ( $\dot{y} = 0.147f^2 - 0.323$ ,  $R^2 = 0.99$ ). This result corroborates scaling laws for thrust generation based on tethered experimental data [84, 7].

Frequency-driven maneuvers—when compared with amplitude-driven maneuvers—also led to higher streamwise velocities ( $\dot{y}$ ) at the end of the maneuvers (Figure.4.2 *c*). As a result, the hydrofoils coasted further after the 10-cycle maneuver was complete. In the frequency-driven case, these post-maneuver displacements were often comparable to the displacements of the maneuver itself. In terms of total displacement, i.e. maneuver plus post-maneuver coasting, frequency-driven displacements exceed amplitude-driven displacements moreso than illustrated.

In addition to recording displacements, we also recorded the peak magnitudes of streamwise and lateral forces. Increasing frequency led to higher positive peaks in streamwise force but had little affect on negative peaks in streamwise force Figure.4.3 *d*). In contrast, increasing amplitude accentuated both the positive and negative peaks in streamwise force, presumably due to the increased projected area caused by higher amplitudes ( $c \cdot w \cdot \sin \theta_0$ ). As for lateral forces, positive and negative peaks increased monotonically with Strouhal number and increased faster with increasing at  $St \approx 0.3$ , increasing frequency to 2.75 Hz led to lateral force peaks about 1.7 times higher than the peaks brought on by increasing amplitude to  $\theta_0 = 18^\circ$ . ( $|C_L| = 4.7$  vs. 2.8). Because the pitching motion was symmetrical for these streamwise maneuvers, the positive and negative peaks of the lateral force

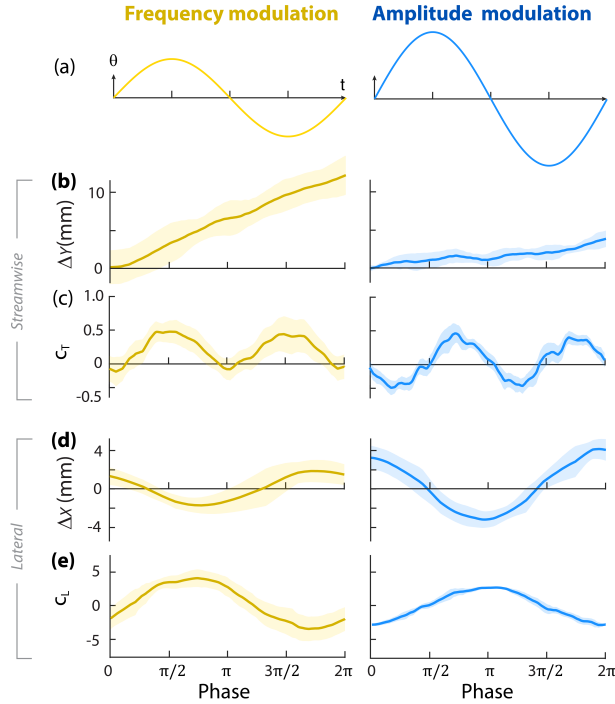


Figure 4.3: **Intracycle dynamics of streamwise maneuvers.** Curves and shaded bands represent the mean and standard deviation across five trials of the 5th pitching cycle of the maneuver. (a) Pitching motion profiles. (b) Streamwise displacement. (c) Streamwise force coefficient. (d) Lateral displacement. (e) Lateral force coefficient.

remained symmetrical.

#### 4.1.2 Instantaneous forces during streamwise maneuvers

The dynamics within a pitching cycle offer more details about the streamwise maneuvers. To compare instantaneous dynamics of the frequency-driven and amplitude-driven maneuvers, we compared two cases at a comparable Strouhal number ( $f = 2.75$  Hz,  $\theta_0 = 10^\circ$  vs.  $f = 1.5$  Hz,  $\theta_0 = 18^\circ$ ;  $St \approx 0.3$ ). To avoid start and end effects, we compared the middle (5th) cycle of the 10-cycle maneuver averaged over the five trials.

On a per cycle basis, the frequency-driven maneuver produces more displacement than the amplitude-driven maneuver ( $\Delta y = 12$  mm/cycle vs. 4 mm/cycle; Figure.4.3 b). These displacements correspond to average streamwise velocities of 27 mm/s and 6 mm/s. Instantaneous forces offer a more nuanced confirmation of the trends observed in the maneuver

bulk (Figure.4.2 *d,e*; Figure.4.3 *c,e*). Increasing frequency caused higher positive peaks in streamwise force, with negative streamwise forces (drag) only appearing in two brief periods of the pitching cycle (Figure.4.3 *c*). In comparison, increasing amplitude led to a higher streamwise force peaks and lower negative peaks. The streamwise force reached its negative peak as the hydrofoil had passed its midline and was approaching its maximum pitching angle (phase between  $n\pi$  and  $n\pi + \pi/2$ ).

Instantaneous kinematics also reveal that lateral recoil is more significant for the amplitude-driven maneuvers. While lateral recoil was almost constant with increasing frequency, it increased considerably with amplitude. The peak-to-peak lateral displacement ( $\Delta x$ ) was 4 mm for the  $f = 2.75$  Hz case but 7.5 mm for the  $\theta_0 = 18^\circ$  case (Figure.4.3 *d*). For comparison, peak-to-peak lateral displacement was 4.2 mm for the baseline kinematics. However, the lateral force peaks were actually higher in the frequency-driven maneuvers (Figure.4.3 *e*). The reason for this apparent contradiction is the shorter cycle times in the frequency-driven maneuvers. Lateral forces scale with lateral acceleration ( $\ddot{x}$ ), and lateral displacements scale with lateral acceleration times the square of the period ( $\ddot{x} \cdot f^{-2}$ ). Frequency-driven maneuvers had higher lateral accelerations (Figure.4.2 *c*), but those accelerations scaled with  $f^2$  and therefore led to comparable lateral displacements.

### 4.1.3 Bulk performance of lateral maneuvers

We now consider the bulk performance of the lateral maneuvers. As expected, both spatial and temporal asymmetries led to lateral displacements (Figure.4.4 *b*). Spatial asymmetries tended to result in larger displacements (e.g.  $\Delta x = 95$  mm for  $\theta_{\text{bias}} = 3^\circ$  vs. 25 mm for  $\beta = 0.9$ ). In the case of spatial asymmetry, lateral displacement increased linearly with pitch bias ( $\Delta x = (32 \text{ mm}/^\circ)\theta_{\text{bias}}$ ;  $R^2 = 0.99$ ). In the case of temporal asymmetry, lateral displacement increased with stroke speed ratio, but with no discernable closed-form scaling.

Lateral maneuvers also caused considerable streamwise displacements. Despite the

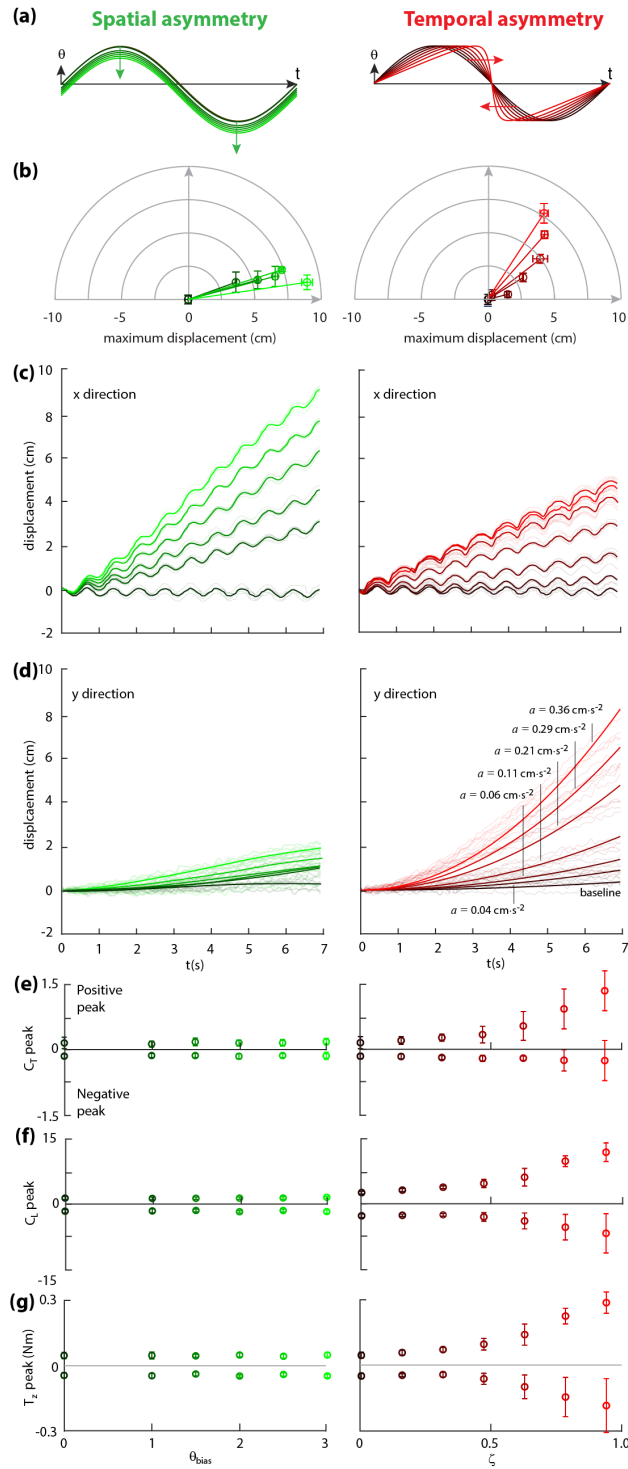


Figure 4.4: **Bulk performance of streamwise maneuvers.** (a) Pitching motion profiles. (b) Displacement in the x-y plane after the 10-cycle maneuver. (c) Time-history of streamwise displacement during the maneuver. Light lines: raw data; dark lines: fitted parabolas. (d) Streamwise force peak magnitudes. (e) Lateral force peak magnitudes.

maneuvers' defining features being lateral asymmetry, the streamwise displacement was at times comparable to the lateral displacement. When  $\beta = 0.9$ , for example, the displacement was higher in the streamwise direction than in the lateral direction ( $\Delta y = 76 \pm 7$  cm;  $\Delta x = 49 \pm 2$  mm). This effect can also be seen from streamwise accelerations (Figure.4.4 *d*). At  $\beta = 0.9$ , the streamwise acceleration was  $3.6 \text{ mm/s}^2$ —higher than any streamwise acceleration caused by increasing amplitude. The lateral maneuvers, like the streamwise maneuvers, showed nearly constant streamwise acceleration ( $R^2 > 0.94$  for quadratic fits, Figure.4.4 *d*).

Unlike the streamwise maneuvers, where streamwise velocity was steadily increasing—lateral maneuvers produced nearly constant bulk lateral velocities (Figure.4.4 *c*). These lateral velocities increase with pitch bias angle ( $\theta_{\text{bias}}$ ) and stroke speed ratio ( $\beta$ ), though they level off beyond a critical stroke speed ratio of about 0.6. Lateral recoil is relatively unaffected by  $\theta_{\text{bias}}$  but increases with stroke speed ratio.

The differing streamwise and lateral force peaks further illustrate the differences between temporal and spatial pitching asymmetries. As  $\theta_{\text{bias}}$  increases, streamwise and lateral force peaks stay the same, even at the largest  $\theta_{\text{bias}}$  value (Figure.4.4 *e,f*). As  $\beta$  increases, negative streamwise force peaks remain relatively unchanged but positive streamwise force peaks rise considerably (Figure.4.4 *e*). Increasing  $\beta$  also leads to a sharp increase in the magnitude of positive and negative lateral force peaks (Figure.4.4 *f*).

Because we merged the control surface and the propulsor into one device, our hydrofoil does not have the yaw freedom that a fully untethered hydrofoil would experience. However, measurements of yaw torque provide some clues as to what a free hydrofoil's yaw response might be. Because the yaw torque is highly correlated with lateral force, we observed the same trends in yaw torque as in lateral force (Figure.4.4 *f,g*). The large differences between positive and negative yaw peaks suggest that a free hydrofoil would be more unstable in yaw in the temporal asymmetry case compared to the spatial asymmetry case.

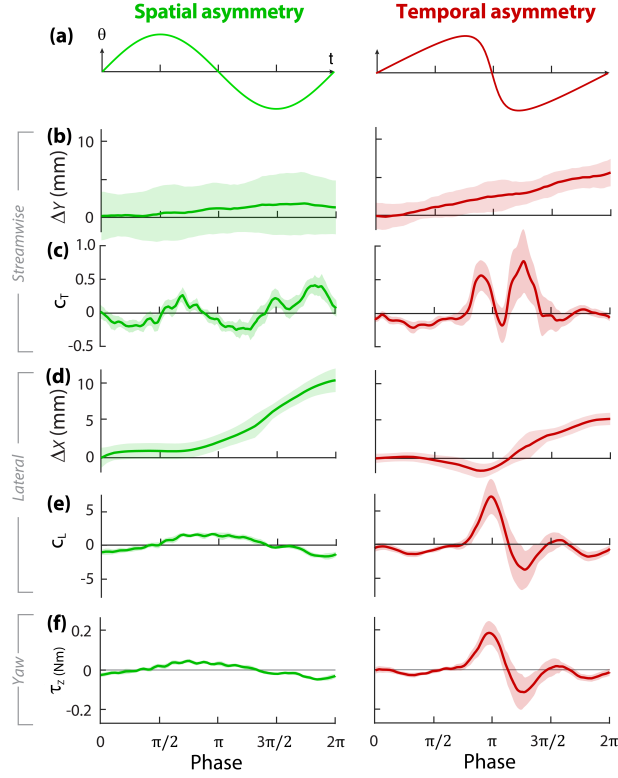


Figure 4.5: **Intracycle dynamics of lateral maneuvers.** Curves and shaded bands represent the mean and standard deviation across five trials of the 5th pitching cycle of the maneuver. (a) Pitching motion profiles. (b) Streamwise displacement. (c) Streamwise force coefficient. (d) Lateral displacement. (e) Lateral force coefficient.

#### 4.1.4 Instantaneous forces during lateral maneuvers

The dynamics within a pitching cycle offer more details about the lateral maneuvers. As a representative comparison, we compared the  $\theta_{\text{bias}} = 3^\circ$  and  $\beta = 0.75$  cases (Figure.4.5), but the same qualitative conclusions can be drawn from any pair of our spatial and temporal maneuvers. As before, we compared the middle (5th) cycle of the 10-cycle maneuver averaged over the five trials.

As expected based on bulk displacements (Figure.4.4 b), lateral maneuvers cause small streamwise displacements within each pitching cycle ( $\Delta y = 2 \text{ mm/cycle}$  for  $\theta_{\text{bias}} = 3^\circ$  vs.  $1.1 \text{ mm/cycle}$  for  $\beta = 0.75$ , Figure.4.5 b). Streamwise forces were larger in the second half of the pitching cycle (Figure.4.5 c), presumably because the streamwise-projected area differs between halfstrokes when pitch bias is introduced. Streamwise forces in the temporal

asymmetry case show a very different pattern. Two large force peaks appear in the middle of the pitching cycle about  $0.4\pi$  apart in phase (Figure.4.5 *c*). This burst in streamwise force mid-cycle helps to explain the larger streamwise displacements caused by temporal asymmetry.

Spatial asymmetry also led to smoother lateral maneuvers, whereas temporal asymmetries led to more lateral recoil within each pitch cycle. In the spatial asymmetry case, the pitch bias shifted the lateral force slightly (Figure.4.5 *e*), causing a smooth, monotonic lateral displacement within the cycle (Figure.4.5 *d*). As for temporal asymmetry, the hydrofoil generated a strong positive lateral force, then a negative lateral force, over a short time (phase  $\approx 0.75\pi$  to  $1.5\pi$ , Figure.4.5 *e*). The result is a jerkier lateral displacement, including a short period of negative lateral displacement (Figure.4.5 *d*).

As with the spatial asymmetries, the yaw torque ( $\tau_z$ ) showed a similar trend as the lateral force. Adding spatial asymmetry introduced small perturbations to yaw torque, whereas adding temporal asymmetry introduced large positive and negative peaks in yaw torque, presumably with implications for yaw stability in the case of a fully untethered hydrofoil.

#### **4.1.5 Wake structures behind lateral maneuvers**

Because the lateral maneuvers revealed unexpected dynamics, we sought to understand and characterize the flowfield behind laterally maneuvering hydrofoils. As a control case, we considered the wake produced by the baseline kinematics. This symmetric motion produced a classic reverse von Kármán vortex street, with each vortex shed at roughly the moment of maximum pitch angle (Figure.4.6 *a*). Despite the symmetric hydrofoil kinematics, the vortex street was not perfectly symmetric about the centerline of the water channel (centerline  $+0.05c$  at phase  $\pi$ ,  $+0.2c$  at phase  $2\pi$ ). Asymmetric wakes generated by symmetric motions have been observed previously; the instability occurs naturally and is sensitive to initial pitch direction and Strouhal number [102, 103].

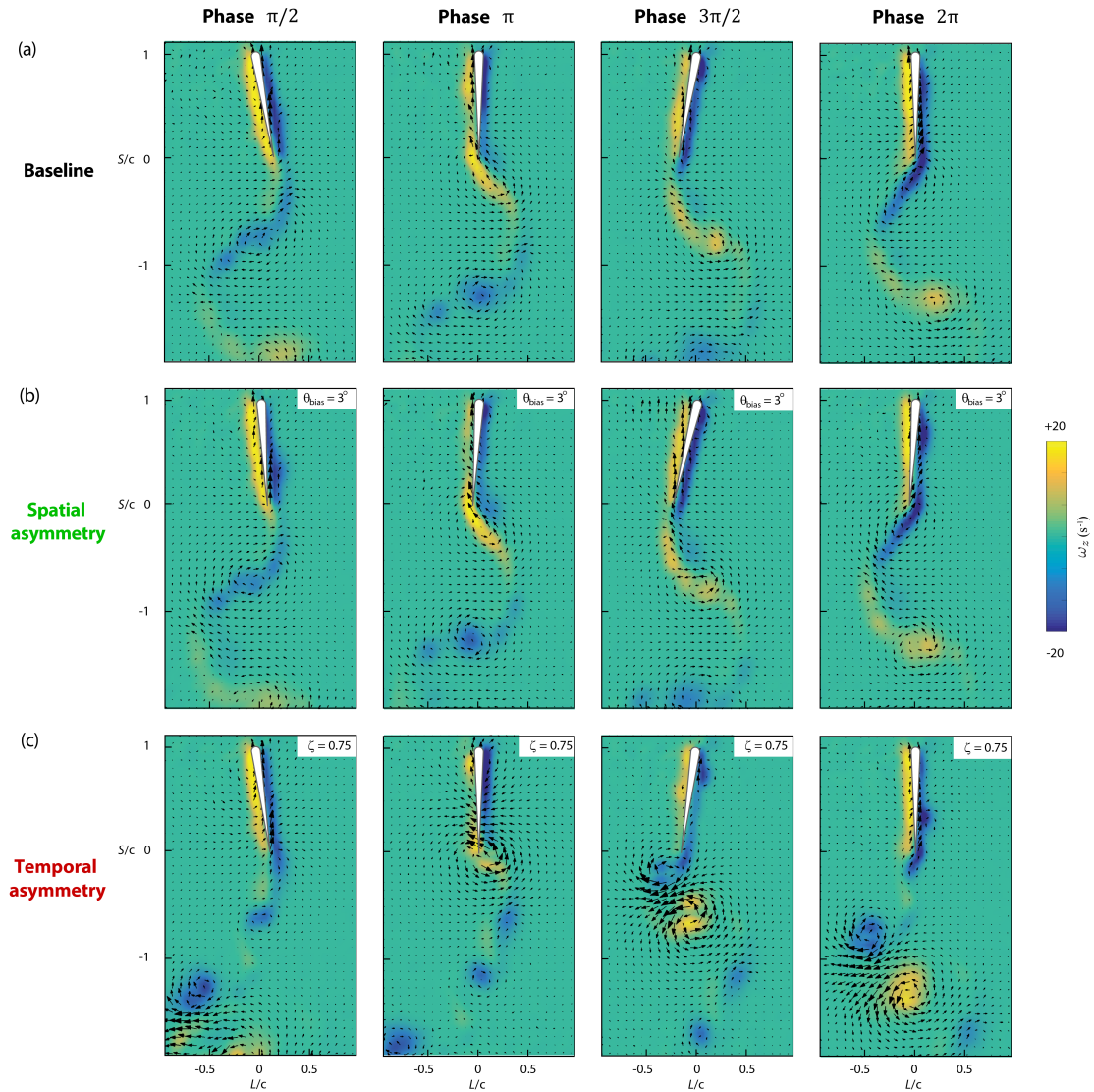
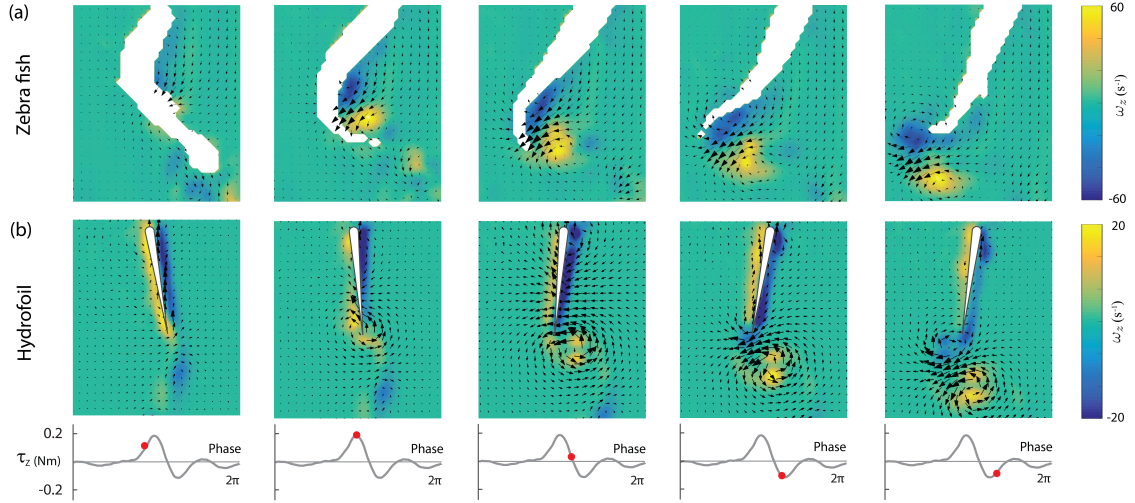


Figure 4.6: **Flow field during lateral maneuver.** (a) Baseline kinematics. (b) representative spatial asymmetry case ( $\theta_{bias} = 3^\circ$ ). (c) Representative temporal asymmetry case ( $\beta = 0.75$ ). In all cases, incoming flow speed was subtracted from the velocity fields. First row: phase =  $\pi$ ; second row: phase =  $2\pi$ .



**Figure 4.7: Flow field comparison between zebrafish turning and temporally asymmetric pitching.** (a) Time sequence of the flow field as zebrafish perform a yaw maneuver. Incoming flow speed was subtracted from the velocity fields. Body based  $Re = 2500 \pm 700$ . Time between snapshots:  $1/32$  s. Replotted with permission from [104]. (b) Time sequence of the flow field around the temporal asymmetric hydrofoil ( $\beta = 0.75$ ). Incoming flow speed was subtracted from the velocity fields. Chord based  $Re = 28500$ . Bottom row: yaw torque ( $\tau_z$ ) as a function of phase; red dot indicates phase of PIV.

When spatial asymmetry was added via a pitch bias angle, the wakes were vectored in the direction of the pitch bias. We found both positive and negative vortices were shifted towards in the pitch bias direction by  $0.15c$  compared to the baseline case. Other than this slight deflection, the wake structure was indistinguishable from the vortex street of the baseline case.

Adding temporal asymmetry introduced drastic changes the wake behind the hydrofoil. When the hydrofoil pitched through the midline (phase  $\pi$ ), a strong trailing edge vortex appeared and grew for the rest of the stroke (Figure.4.6 *e,f*). This vortex may help to explain the high-magnitude pulse in lateral force at that same phase (Figure.4.5 *e*). As the hydrofoil reached its maximum pitch angle, it shed this strong positive vortex. Then, as the hydrofoil slowly pitched the other way, a negative vortex shed from the hydrofoil's trailing edge. Together with the positive vortex, this pair of vortices generated a strong jet in the left-rear direction of the hydrofoil (Figure.4.6 *f*). This paired vortex wake topology is a significant deviation from the classic vortex street of the baseline case.

## 4.2 Discussion

An increase in either amplitude or frequency will increase the Strouhal number, which increases thrust [84, 7]. However, we found that at the same Strouhal number, a frequency-driven maneuver six times as much acceleration as an amplitude-driven maneuver ( $\ddot{y} = 7.8 \text{ mm/s}^2$  vs.  $1.3 \text{ mm/s}^2$ ;  $St = 0.3$ ). This result could help explain why natural swimmers prefer to modulate their tail-beat frequency to adjust swimming speed [9]. Increasing frequency also led to less lateral recoil, which suggests greater lateral stability while accelerating. Because our hydrofoil has a fixed average yaw angle, our rig cannot confirm lateral instabilities, but real fish that modulate tail-beat amplitude during accelerations do show greater lateral recoil [37].

While our results suggest that frequency modulation is a better acceleration strategy, amplitude modulation has benefits. First, it could further increase the Strouhal number in cases where frequency was already maximized, leading to even faster accelerations. Second, amplitude can affect wake structure, which affects efficiency. In rainbow trout, for example, increasing amplitude can realign vortex pairs, causing a more efficient downstream-facing momentum jet [9]. Higher amplitudes also provide a rapid braking mechanism due to high drag forces [49]. In fact, it was this mechanism that we harnessed for the recovery phase of our maneuver tests.

Adding pitch bias (spatial asymmetry) created smooth, quasisteady lateral maneuvers. The fact that lateral displacement scaled linearly with pitch bias suggests that those lateral maneuvers were driven by the quasisteady lift term of thin airfoil theory [105]. These findings are in line with maneuvering studies of fish-inspired robots, where pitch bias causes smooth yaw motions [106]. A key advantage of pitch bias modulation is its mechanical simplicity. Several Central Pattern Generator (CPG) control-based robot fishes have deployed this simple strategy to perform large radius turning [42, 3].

Modulating stroke speed ratio (temporal asymmetry) created lateral maneuvers that

were more complex. First, the lateral asymmetry caused streamwise acceleration due to the higher mid-cycle lateral tailspeeds. Fish and robots wanting to avoid this effect may want to reduce frequency and/or amplitude as they change stroke speed ratio. Fish can adjust both simultaneously: rainbow trout, for example, modulate their amplitude/frequency while swimming through a vortex street [40]. Introducing temporal asymmetry also led to a paired vortex wake (Figure.4.6 *f*) and a burst of asymmetric yaw torque (Figure.4.5 *f*), which could presumably be used to rapidly reorient a fish or robot's yaw angle.

Because some fish use temporal asymmetry to produce yaw maneuvers, we compared our results with dynamics of turning zebrafish. The positive and negative peaks in lateral force that we observed (Figure.4.5 *e*) are qualitatively similar to lateral force estimates along the body of a turning zebrafish [107]. The flowfields around a turning zebrafish [104] also share some features with our PIV results (Figure.4.7). During the yaw turn, the fish uses a fast leftward stroke to release a strong vortex pair into the wake. The caudal fin then sheds this vortex pair, and the fish's body yaw angle shifts. Our PIV results also show a vortex pair shed around the moment of a sudden yaw torque (Figure.4.7 *b*). Other phases in the cycle show fewer similarities. Our hydrofoil is rigid, so it does not generate vorticity along a curled body as the fish does, and our hydrofoil's mean yaw position cannot react to the yaw torque. Still, the similarities suggest that at least some of the dynamics we observed can be used to better understand yaw reorientations in real fish.

In the context of fish-inspired robots, actuator constraints will dictate what maneuver types are feasible. Implementing actuation may cost more energy and increase the complexity of the robot, so choosing an asymmetry type is a critical design decision. For example, the Tunabot [4], in its current form, has one degree of freedom and performs straight-line swimming. Modulating frequency requires simple commands to the motor, whereas modulating amplitude would require a new actuator. Modulating the pitch bias angle would require yet another actuator, but modulating stroke speed ratio could be done with a rotary encoder and a more advanced motor controller.

# Chapter 5

## Tuna-Inspired Platform: Multi-fin Interactions

In this chapter, we tested a 3D-printed tuna-inspired platform to explore the interaction between elongated dorsal fins and caudal fins and compared results with immersed boundary simulations. The shape and kinematics of the model are based on bluefin tuna, and the dorsal fin is an idealized triangular shape. The resulting setup allowed us to study the three-dimensional wake of an idealized dorsal fin on a realistic fish body at a realistic Reynolds number. What we found is that while wake capture plays a role, a more dominant feature is a Dorsal-Fin-induced Crossflow that stabilizes the Leading Edge Vortex against the caudal fin. This stabilized flow appears to prolong the thrust-producing section of the caudal fin's flapping cycle, resulting in higher swimming speeds.

### 5.1 Experimental setup and Methods

#### 5.1.1 Fish model design and construction

Using videos of live bluefin tuna, we reconstructed three-dimensional body kinematics using the same procedure as we have used previously [59, 108]. To facilitate comparisons

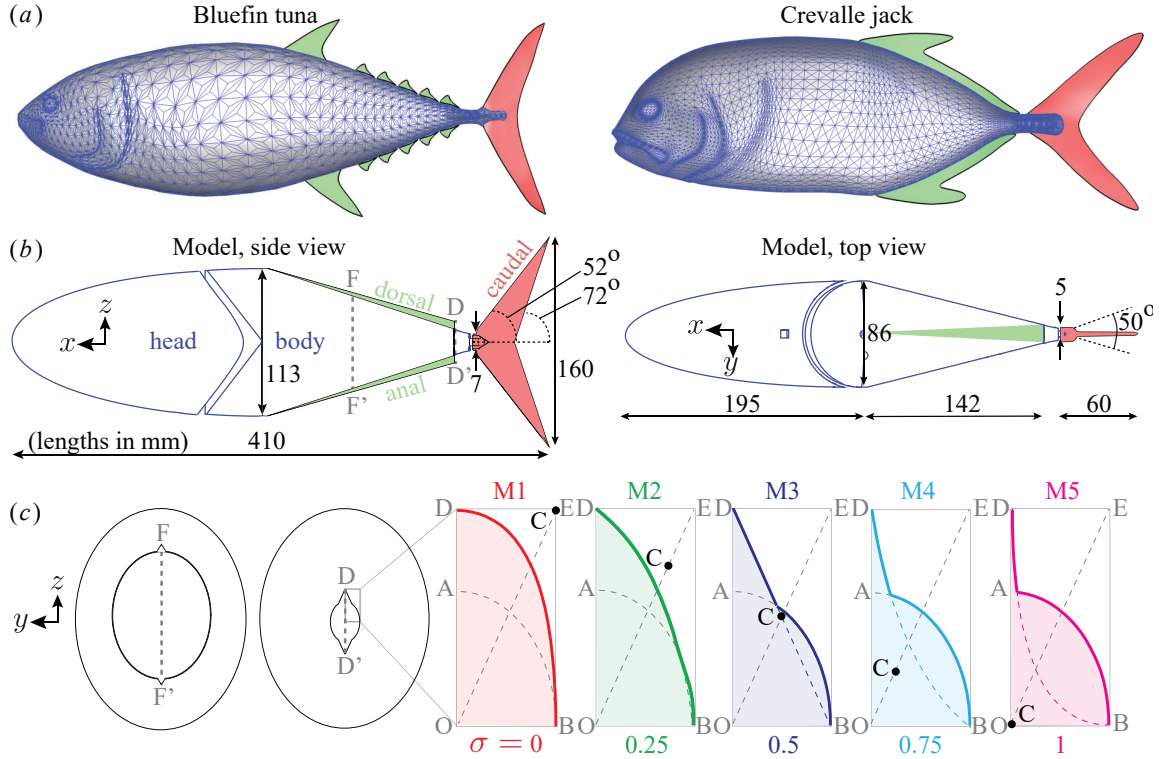


Figure 5.1: **A reduced-order fish model was based on data from live tuna.** (a) Bluefin tuna and Crevalle jack reconstructions from [59]. (b) Reduced-order model used in this study (lengths in mm). The highlighted cross sections (F-F' and D-D') are shown in (c), and cross section D-D' is used to define sharpness. (c) Sharpness ( $\sigma \equiv 1 - \frac{OC}{OE}$ ) varied from 0 to 1 between the five models (M1 to M5). Solid lines show the cross-sections of the body plus fin for each model, while dotted lines show the base ellipse (semi-axes OA and OB) and the Bezier curve (end points B and D, control point C) used to define the cross section.  $OA = 0.97$  cm,  $OB = 0.74$  cm,  $OD = 1.73$  cm.

with fish whose elongated dorsal features are simpler, such as the Crevalle Jack, we chose an archetypal elongated dorsal fin: a long triangular fin whose height is equal to that of the most distal finlet. The fin was mirrored on the bottom side of the fish to allow wake studies far from any influence of the sting supporting the model. We also eliminated other morphological details that could affect the flow on the caudal fin, such as the keel and the large dorsal fin upstream of the finlets. Our resulting reduced-order fish model is based on 11 key measurements of the high fidelity tuna model (Figure 5.1a,b) and has a whole body length  $\ell$  of 410 mm. This reproducible model captures the major geometrical features of the original, including elongated dorsal features just upstream of the caudal fin.

The tuna model was 3D printed as two parts: a fixed head and an actuated body (Figure 5.1*b*). The head of the model was fixed in place by a quarter-inch carbon fiber rod, while the body was actuated by quarter-inch carbon fiber drive rod (Figure 5.2*a*). The drive rod, driven by a high torque digital servo motor (Dynamixel MX-64), twisted with harmonic pitching motions, that is,  $\theta = \theta_0 \sin(2\pi ft)$ , where  $\theta$  is pitch angle,  $\theta_0$  is pitch amplitude,  $f$  is pitch frequency, and  $t$  is time. The caudal fin was actuated indirectly through a passive hinge joint (Figure 5.1*b*). Since fishes are typically frequency rather than amplitude modulators ([109, 110]), we set pitch amplitude to a constant 13 based on the tuna videos (peak-to-peak fin excursion  $A \approx 0.2\ell$ ). The hinge joint of the caudal fin restricted peak-to-peak caudal fin angles to be less than 50 (Figure 5.1*b*).

The “sharpness” ( $\sigma$ ) of the dorsal fin was parameterized with Bezier curves, which allows continuous sharpness values ranging from 0 (no fin) to 1 (“razor-thin” panel) (Figure 5.1*c*). We considered five sharpness values for this study:  $\sigma = 0, 0.25, 0.50, 0.75$  and 1. The cross-section of the model is the union of the area under the Bezier curves and a base ellipse, which forces the laterally-projected areas of the models to be the same. A constant area means that differences in thrust between the models come from differences in fin geometry, not simply from changes in the total lateral width of the body and fin. The body and head of the tuna model were 3D-printed with ABS material (Dimension 1200es) which is effectively rigid over the frequencies and amplitudes considered here (see Appendix section A.1). To avoid different moments of inertia between the models (M1-M5), we kept the total mass of the model constant ( $222.52 \pm 3.46$  grams). An absolute encoder (US Digital A2K 4096 CPR) verified that body motions were indeed the same between models for the same excitation (less than 0.2 % and 0.5 % variation in measured pitching amplitude and frequency).

### 5.1.2 Speed and economy measurements

To compare the swimming performance of the fin types, we measured the forces and torques on the tuna model while it was suspended in the closed-loop water channel. Tests were done at the center of the channel, where the distance to sidewalls was  $\approx 2.4$  and  $\approx 6.3$  times the max span and max chord of the tail fin. These distances are high enough to avoid sidewall effects based on previous studies [28, 111]. The head of tuna model was mounted independently from the body, so the cycle-averaged streamwise force on the entire tuna model, or “net thrust” ( $\overline{F_T}$ ), is the sum of the drag on the head ( $D_{\text{head}}$ ) and the cycle-averaged streamwise force on the body ( $\overline{F_S}$ ). We first measured  $D_{\text{head}}$  as a function of channel speed by suspending the head from a high resolution one-axis force sensor (Interface Inc., ULC Ultra Low Capacity Load Cell, 1 N). We then measured  $\overline{F_S}$  using a six-axis force sensor (ATI Mini-40, SI-80-4) installed along the drive rod. The measured forces were converted from sensor coordinates to test section coordinates and cycle-averaged over 30 pitching cycles to get  $\overline{F_S}$ . Details of performance calculation can be found in section 2.3.2.

We chose to focus on steady swimming speeds, where the net thrust ( $\overline{F_T}$ ) is zero. Based on preliminary tests at tuna-inspired frequencies, we chose 15 steady swimming speeds ( $u$ ) evenly spaced between 100 mm/s and 240 mm/s (0.24 to 0.59  $\ell/s$ ), meaning Reynolds number based on whole body length ranged from  $Re = 41000$  to 98400. At each swimming speed, we used a Newton-Raphson-based zero-finding scheme to determine the pitching frequency  $f$  that produced zero net thrust. Each test was repeated five times. Details of the Newton-Raphson-based zero-finding scheme can be found in section 2.4.

### 5.1.3 Immersed-boundary method simulations

To test which flow features were insensitive to Reynolds number, we compared our experiments to simulations from an in-house immersed-boundary method solver (see [59, 112,

113] for details). The simulations used identical geometries and kinematics as the experiments, the only difference being a lower Reynolds number based on whole body length ( $Re = 2100$ ). The solver used a nonuniform  $385 \times 193 \times 193$  Cartesian grid (about 14 million points) over a computational domain of  $10\ell \times 6\ell \times 6\ell$ . A cubic volume around the caudal fin used a high-resolution grid ( $0.003125\ell \times 0.00278\ell \times 0.00375\ell$  spacing) to resolve the near-field wake structure. The mesh size was chosen based on extensive tests of mesh refinement combined with experience validating the solver on similar geometries [59].

## 5.2 Results

### 5.2.1 Sharpness affects swimming speed and economy

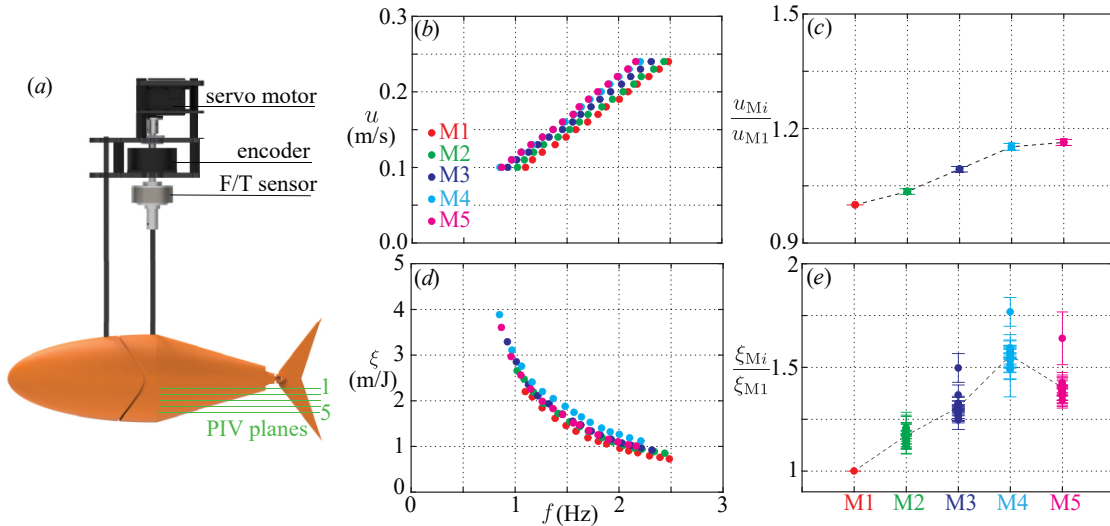


Figure 5.2: **Swimming speed increases with sharpness, while economy peaks for M4.** (a) A servo motor actuated the back half of the model (the “body”), and an encoder and F/T sensor recorded angular displacement and  $z$ -torques. PIV planes 1-5 are used to investigate flow features in Figure 3. Self-propelled swimming speed increases linearly with frequency for each model. (c) Compared to M1, self-propelled speed increases from M1 to M4, but shows no noticeable difference between M4 and M5. (d) Propulsive economy,  $\xi \equiv u/\bar{p}$ , decreases with frequency for each model. (e) Compared to M1, economy increases from M1 to M4, then decreases from M4 to M5. See Appendix. A for cycle-averaged power plots.

Up to a critical sharpness level, sharper dorsal fins lead to faster swimming speeds. For each fin type, the model's steady swimming speed scales linearly with pitching frequency (Figure 5.2*b*), a trend to be expected based on the classic swimming scalings of [114]. As dorsal fin sharpness increases, this linear curve is shifted up and left. A sharper dorsal fin therefore leads to a higher swimming speed at the same pitching frequency, or the same swimming speed at a lower frequency. To better visualize the effect of sharpness, we fitted lines to the speed vs. frequency data for each fin type ( $R^2 = 0.996 \pm 0.001$ ), then compared the slopes. Because all the lines have zero intercept (zero frequency leads to zero swimming speed), the ratio of the slopes gives a measure of how much faster the model swims with a dorsal fin vs. without a dorsal fin. Specifically, the ratio estimates  $u_{Mi}/u_{M1}$  averaged over all frequencies, where  $u_{Mi}$  is the swimming speed of the  $i$ 'th fin type and  $u_{M1}$  is the swimming speed of the control case ( $\sigma = 0$ ) at the same pitching frequency. As sharpness increases from 0 to 0.75, this ratio increases by about 15%, but then saturates; increasing the sharpness further has no measurable result on swimming speed (Figure 5.2*c*).

While the swimming speed plateaus with increasing sharpness (Figure 5.2*c*), the economy peaks at a sharpness value between 0.5 and 1 (Figure 5.2*e*). The economy decreases monotonically with pitching frequency, again consistent with classic scalings [114] (Figure 5.2*d*). To better visualize the effect of sharpness, we calculated  $\xi_{Mi}/\xi_{M1}$ , where  $\xi_{Mi}$  is the economy of the  $i$ 'th fin type and  $\xi_{M1}$  is the economy of the control case ( $\sigma = 0$ ) at the same swimming speed. The ratio gives a measure of how much more efficiently the model swims with a dorsal fin vs. without a dorsal fin at the same speed. As sharpness increases from 0 to 0.75, the economy increases significantly: it rises by about 50% for most of the swimming speeds and up to 75% at the slowest speed considered (Figure 5.2*e*). In contrast, economy decreases slightly as sharpness increases further, showing that economy peaks somewhere between  $\sigma = 0.5$  and  $\sigma = 1$ . Motivated by this peak in economy, we mapped the flow features governing the dorsal-caudal fin interaction and compared them across M1, M3, M4, and M5.

### 5.2.2 Leading Edge Vortex is stabilized on the caudal fin

We first used Particle Image Velocimetry (PIV) to compare the flow fields of M1 (the control case,  $\sigma = 0$ ) to M4 ( $\sigma = 0.75$ ) at an intermediate swimming speed ( $u = 170$  mm/s). What we found is that the Leading Edge Vortex (LEV) of the caudal fin is both stronger and more stable in the M4 case (Figure 5.3*b* vs. 5.3*e*). Attached LEVs can lead to high transient lift forces [115], which in this case presumably enhance thrust and increase the swimming speed (Figure 5.2*d*). Compared to M1, M4 exhibits a stronger, narrower jet of fluid produced by the translating gap between the dorsal and caudal fins (Figure 5.3*b,e*;  $t = 0.1T$ ). This jet forms the LEV, which contains positive  $z$ -vorticity (as seen by, e.g., [116] and [59]). In M1, the LEV fully detaches, leaving a region of slow-moving fluid adjacent to the caudal fin (Figure 5.3*a,b*;  $t = 0.4T$ ). In contrast, M4 exhibits a Dorsal-Fin-induced Crossflow (DFC) that stabilizes the LEV along the caudal fin (Figure 5.3*d,e*;  $t = 0.4T$ ). The crossflow energizes the boundary layer along the caudal fin, keeping the flow there attached longer in the pitching cycle.

By comparing the PIV results with immersed boundary method simulations, we found that major parts of these dorsal-caudal interactions persist at lower Reynolds numbers. The simulations, which simulate a lower  $Re$  than the experiments (2100) but use the same geometry and Strouhal number, also show crossflow induced by the sharp dorsal fin of M4 (Figure 5.3*f*). Like in the experiments, this crossflow inhibits LEV detachment and energizes the boundary layer along the caudal fin. Unlike in the experiments, the negative  $z$ -vorticity shed from the dorsal fin is confined to well-defined cores. In the experiments, these cores have mostly broken apart by  $t = 0.4T$  (Figure 5.3), as expected given the higher relative strength of inertial forces in the flow.

To quantify the Dorsal-Fin-induced Crossflow and the flow attachment on the caudal fin, we considered average flow speeds in two regions of the PIV data. Region 1 quantifies the strength of the crossflow produced by the dorsal fin at  $t = 0.3T$ , and Region 2 quantifies

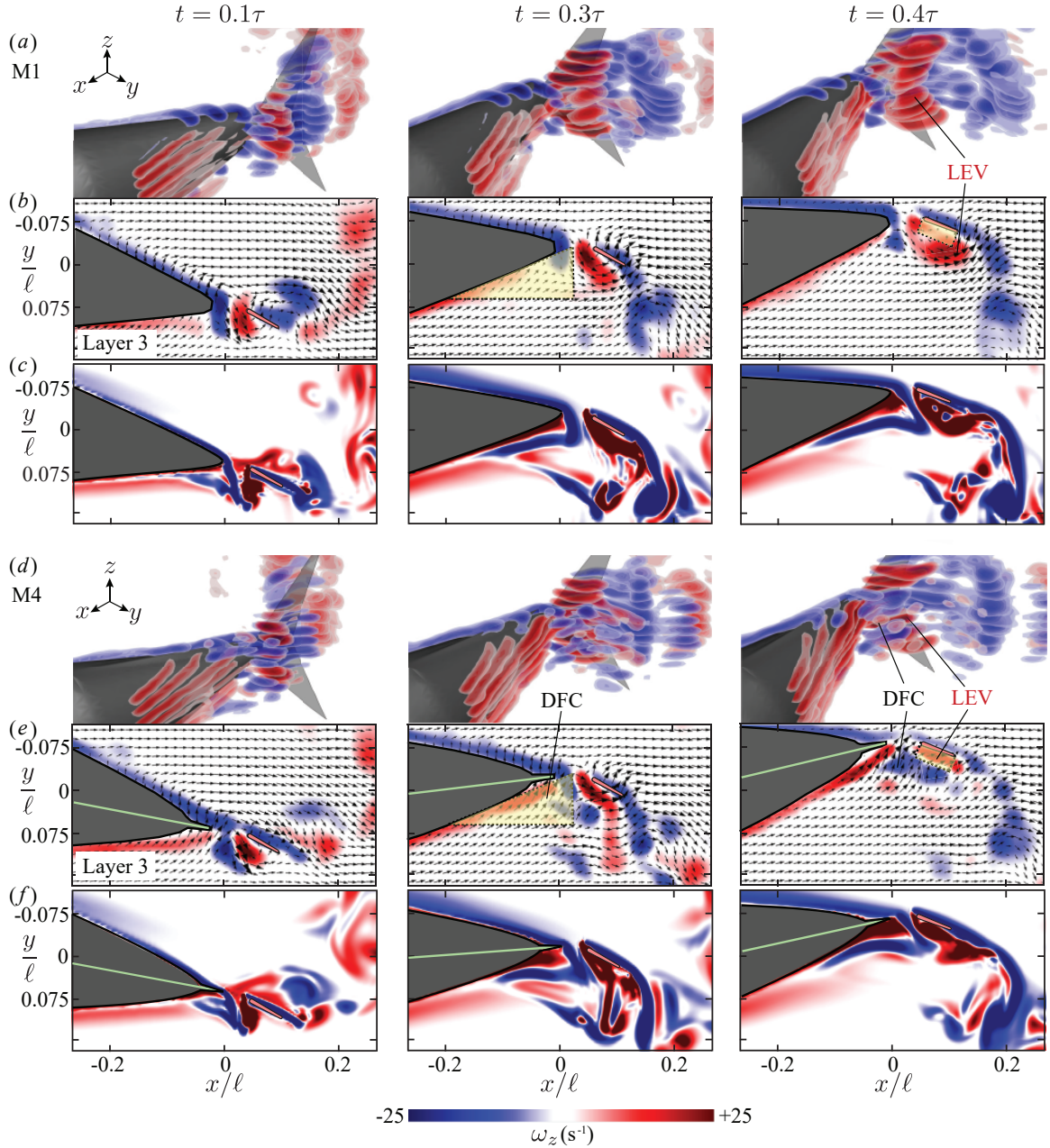


Figure 5.3: **Both PIV and simulations reveal a more stable Leading Edge Vortex (LEV) on the caudal fin. Results are shown at self-propelled swimming for M1 (a,b,c) and M4 (d,e,f) at three times in the flapping cycle  $T$ :  $t = 0.1T$ ,  $0.3T$ , and  $0.4T$ .** (a,d) Nine stacked layers of phase-averaged  $z$ -vorticity show how the LEV separates from the caudal fin around  $t = 0.3T$ . (b,e) The third vorticity contour from the top (Layer 3), shows the separation event in more detail. In the case of M4, the sharp dorsal fin induces a crossflow (DFC) which stabilizes the LEV on the caudal fin. The dotted triangular and rectangular regions are used for averaging flow speeds in Figure 4. (c,f) Simulated  $z$ -vorticity contours are shown at the same time steps. The simulations show a more stable flow on the caudal fin in M4, but the effect is less pronounced than in the experiments. See Appendix. A for PIV around M1\*.

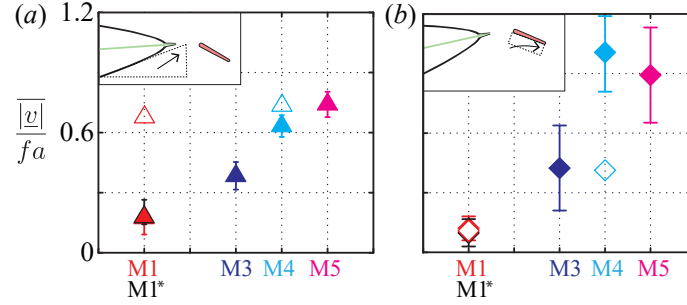


Figure 5.4: **Dorsal Fin-induced Crossflow (DFC) increases with fin sharpness, while flow attachment on the caudal fin peaks at M4.** (a) DFC is quantified by the average flow speed ( $|\underline{v}|$ ) in the triangular region in Figure 5.3 3b,e ( $t = 0.3T$ ). To facilitate a fair comparison across models, speed was normalized by  $fA$ . Filled symbols, PIV; empty symbols, simulations. (b) The stabilization of the flow on the caudal fin was quantified by the average flow speed in the rectangular region in Fig 3b,e ( $t = 0.4T$ ). Flow attachment increases from M1 to M4 but shows no further increase from M4 to M5.

how well the flow is attached to the caudal fin at  $t = 0.4T$  (Figure 5.3b,e). In each region, we calculated  $|\underline{v}|/(fA)$ , where  $|\underline{v}|$  is the average in-plane flow speed in the region. This ratio, which represents how fast the flow is moving relative to typical lateral speeds of the fish model ( $fA$ ), allows a fair comparison of flow speeds between the models. Because the frequency is similar across models when  $u = 170$  mm/s (M1,  $f = 1.81$  Hz; M3,  $f = 1.63$  Hz; M4,  $f = 1.57$  Hz; M5,  $f = 1.56$  Hz), the denominator of the ratio does not vary more than  $\pm 20\%$  across models. However, to ensure the scaling did not affect our conclusions, we also tested the M1 model at the flapping frequency of the M4 model and calculated  $|\underline{v}|/(fA)$  for both cases (notated as “M1” and “M1\*”).

Average flow speeds in Regions 1 and 2 reveal that the Dorsal-Fin-induced Crossflow increases with fin sharpness (M1 to M5), but that caudal fin flow attachment saturates beyond M4 (Figure 5.4). In the case of M1,  $|\underline{v}|/(fA)$  is less than 0.3 in both Regions 1 and 2, denoting slow crossflow and mostly stagnant flow adjacent to the caudal fin (Figure 5.4a,b). In Region 1,  $|\underline{v}|/(fA)$  increases monotonically with sharpness, showing that sharper dorsal fins induce more crossflow. In Region 2, however,  $|\underline{v}|/(fA)$  increases with sharpness up to  $\sigma = 0.75$  (M4), but shows no further increase beyond  $\sigma = 0.75$ . The similarities between the M1 and M1\* cases show that these differences are due to dorsal fin geometry,

not to the 13% difference between the self-propelled pitching frequencies of M1 and M4. The low  $Re$  simulations show similar trends but with a lower magnitude. Dorsal fin sharpness appears to increase swimming speed and economy by promoting flow attachment, but – beyond a critical sharpness – only cost more power without further improving the flow characteristics over the caudal fin. While the crossflow is clearly visible in 2D PIV slices (Figure 5.3e, 5.4a), the origins of the crossflow can only be seen with a 3D flow analysis.

### 5.2.3 Sharp dorsal fins create streamwise conical vortices

To explore the origins of the Dorsal Fin-induced Crossflow, we used the simulation results to map 3D streamlines. Streamlines seeded on the dorsal fin reveal long, thin, conical vortices (Figure 5.5b). These vortices are visible as patches of negative vorticity in the stacked PIV slices for M4 (Figure 5.3d). The two vortices narrow, strengthen, and move towards each other as they pass over the caudal fin. In contrast, the M1 case shows no such vortices (Figure 5.5a). Streamlines seeded upstream of the body reveal a key consequence of the tightly-packed vortices: the surrounding water is moved laterally toward the caudal fin, then along the fin in a spanwise flow. This lateral flow towards the caudal fin is consistent with the 2D PIV, where the crossflow towards the caudal fin was observed in the  $x$ - $y$  plane (Figure 5.3e).

One consequence of the vortex-driven mechanism in Figure 5.5 is that LEV-stabilization should be relatively insensitive to the phase lag between the dorsal and caudal fins. In the experiments, the phase lag follows from the passive mechanics of the caudal fin; in the simulations, phase lag is prescribed based on high speed video of the experiments. Therefore, to explore phase sensitivity, we re-ran the simulations with manually adjusted caudal fin phase. We considered four perturbations from the original phase lag (126): 72, 90, 108, and 144. To make a fair thrust comparison, we matched the Strouhal numbers to the original by tuning pitching amplitude  $\theta_0$ . The thrust increase between M1 and M4 was mostly positive over this range (72, +2.4%; 90, +6.3%; 108, +15%; 126, +13%, 144, -6.3%; see

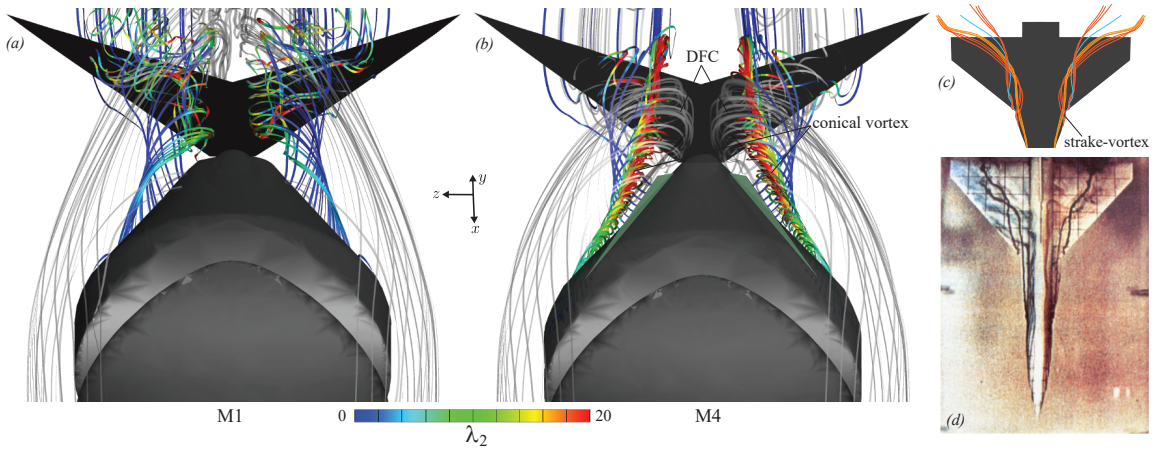


Figure 5.5: **Long, thin, conical vortices are shed from sharp dorsal fins, causing a lateral crossflow towards the caudal fin.** Flows were visualized by mapping streamlines from the simulation results on M1 (a) and M4 (b) at  $t = 0.4T$ . In M4, streamlines seeded on the dorsal side of the body (25 uniformly seeded on the dorsal fin), colored by the  $\lambda_2$  criterion, are wound into tightly-packed vortices that move downstream and over the caudal fin. Streamlines seeded upstream (50 seeded upstream of the head), colored in light gray, show how these vortices induce a flow toward and along the caudal fin in M4 but not in M1. (c) Wing strake vortices (orange) shown passing over the main wing (schematic adapted from [117]) (d) Dye injection reveals strake vortices promoting flow attachment over an F-16A model in a water channel. Angle of attack, 15. Reynolds number, 15,000. Reprinted with permission from [117].

Appendix. A). The mechanism is indeed robust to changes in phase up to around a quarter of the flapping cycle. Beyond that, the caudal fin's lateral velocity presumably becomes out of sync with the stabilizing crossflow provided by the dorsal fin.

### 5.3 Discussion

In our study, the Leading Edge Vortex (LEV) of the caudal fin starts stronger and stays attached longer in M4 compared to M1 (Figure 3e, 4b, 7), and M4 swims faster than M1 (Figure 2e). These observations are consistent with previous findings that LEVs can increase thrust when attached to the caudal fin (e.g. [118]). In heaving and pitching motions, LEVs are shed soon after formation [119, 120], causing a transient burst of high thrust. The stability of the LEV increases with rounder fin planforms, lower actuation frequencies, spanwise flow, and lower angles of attack [115]. Spanwise flows, for example,

prolong LEV attachment – and consequently transient forces – on caudal fins [118] and rotating wings [121, 122, 123]. Cycle-averaged thrust on fins can therefore be enhanced by strengthening LEVs, increasing LEV stability, or both.

The Dorsal Fin-induced Crossflow we observed affects the caudal fin’s angle of attack and creates spanwise flow along the caudal fin. Caudal fin shape is constant, and the pitching rates are similar (13% difference between M1 and M4; 0% between M1\* and M4), so those two LEV stabilization mechanisms are less relevant here. The effective angle of attack, however, will often be lowered by the crossflow, particularly at the center of the caudal fin as it moves laterally (e.g.  $t = 0.3T$  in Figure 5.3e). Through most of the pitching cycle, the effective angle of attack is lower for M4 than for M1 (e.g.  $9 \pm 6$  less at the mid-stroke,  $t = 0.5T$ , Appendix.A). In contrast, at stroke transition ( $t = 0.5T$ ), the angle of attack is  $16 \pm 6$  higher for M4 than for M1. This higher angle may account for the stronger LEV created in M4 at the beginning of next stroke ( $t = 0.1T$ , Figure 5.3e,b). We cannot measure spanwise flow quantitatively from the 2D PIV slices, but  $x$ - $y$  velocities along the caudal fin are nearly 10 times higher for M4 than for M1 (Figure 5.4b), and the simulated streamlines (Figure 5.5b) suggest spanwise velocities along the caudal fin are also higher. It appears that the crossflow alters angle of attack and spanwise flow to create a stronger and more stable LEV for M4, which helps to explain its higher swimming speeds in the context of the known behavior of LEVs [115].

We suspect that a helpful analogue of the flow considered here is the flow over wing strakes and Leading Edge Root eXtensions (LERX) upstream of airplanes wings. Strakes are long thin surfaces that – like elongated dorsal fins – extend just upstream of the main lifting device [124]. In aircraft design, “strake vortices”, which are shed from the elongated strakes, increase lift on the main wing during maneuvers by lowering the angle of attack and promoting spanwise flow (Figure 5.5c,d). High lift devices on large aircraft function at higher Reynolds numbers ( $\sim 10^6$  based on wing chord, compared to  $\sim 10^5$  here), but given the qualitative similarities we observed across a decade of Reynolds numbers (Figure 5.3),

it may be that similar mechanisms are at work here. In fact, strake vortex flow visualizations are sometimes conducted at Reynolds numbers closer to  $10^4$  (Figure 5.5c).

One key feature of the fin-fin interactions observed here is an insensitivity to the phase lag between dorsal and caudal fins. Our phase sensitivity tests reveal that the thrust boost in M4 persists over approximately a 70 range of phase lags. Phase lag may be more relevant at lower Reynolds numbers, where vortices remain more coherent. Phase-dependent wake-capture mechanisms were reported, for example, in simulations of jack fish (Liu *et al.* 2017,  $Re = 2100$ ). Phase lag may be especially important for isolated dorsal fins, like the main dorsal fin of the Bluefin tuna (Figure 5.1a). For isolated upstream fins, the thrust of the downstream fin is only enhanced for certain combinations of fin placement and Strouhal number (Boschitsch *et al.* 2014,  $Re = 4700$ ; Akhtar *et al.* 2007,  $Re = 20000$ ). At higher Reynolds numbers, disorganized, small-scale vortex structures reduce the possibility of constructive or destructive wake interactions (Daghooghi & Borazjani, 2015,  $Re \approx 50000$ ). Elongated dorsal fins – by inducing a phase-insensitive crossflow – may boost thrust over a wider range of conditions.

A phase-insensitive mechanism also lends evidence to theories about the role of finlets. Finlets are thought to enhance the vortex circulation on caudal fins, thereby increasing thrust [126]. They are also thought to serve as a fence that regulates crossflow [127, 128] and as a mechanism for redirecting flow and reducing separation along the caudal fin [129, 130]. Our results show that the latter mechanisms (flow redirection) persist even for the simple case of one elongated “finlet”. The resulting caudal fin thrust enhancement may be further tuned by the complex morphologies and kinematics of finlets, some of which can be individually actuated [126].

# Chapter 6

## Tuna-Inspired Platform: Real-time Adjustable Flexibility

In this chapter, we quantified the energetic benefits of tuning stiffness using a combination of modeling and experiments over a range of swimming speeds. In particular, we found that tuna-like robots must tension their tail joint with a force proportional to their speed squared. The mechanism is analogous to a continuously variable transmission (CVT), where a car improves its efficiency by tuning gear ratio with driving speed. Our model explains how fish can use the same efficient gait over a wide range of high speeds [131], and why robots with a fixed amount of flexibility will never surpass fish in terms of performance.

### 6.1 Experiment setup and Methods

#### 6.1.1 Tuna-tail stiffness test

To measure the tail joint (peduncle) stiffness of tuna tails, we simulated loads on vertically-mounted tuna tails ( $n = 6$ , Figure. B.1). For each tail, we dissected the peduncle to expose the lateral tendons, then hung weights from the tendons to prescribe the tendon tension ( $T_M$ ). For each tension, we used attached a second set of weights to the centerline distal

tip of the caudal fin to simulate a lateral force ( $F_C$ ). To account for fin asymmetries, we defined  $F_C = 0$  where there was no lateral displacement.

The torque applied to the tail fin was  $\ell_{\text{laser}}F_C$ , where  $\ell_{\text{laser}}$  was the perpendicular distance from the applied load to the axis on which the tail fin was mounted. For each combination of tendon tension and lateral force, we measured the displacement of the tail fin's centerline distal tip ( $\Delta d_{\text{tip}}$ ) using a laser distance sensor ( $\pm 0.01$  mm, Figure. B.1c). The corresponding approximated tail fin pitch angle was  $\theta_F = \tan^{-1}(\Delta d_{\text{tip}}/\ell_{\text{laser}})$ . Each test was repeat 3 times.

### **6.1.2 Tuna-inspired platform with tunable stiffness tail**

Our goal in designing the tuna-inspired platform was to build a platform for testing the performance of tail fins with tunable stiffness. We therefore wanted to recreate some key features of scombrid fish (tuna, mackerels, bonitos) while using a reduced-order approach to ensure repeatability.

The basic shape of our platform is based on videos of real tuna. The shell of the platform was taken from one of our previous studies [132], in which we created a 3D model based on videos of live yellowfin tuna. In that study, we imported bottom and side view videos to Maya to reconstruct a high-fidelity tuna model [133]. Then we simplified the surface shape and removed the keel, large dorsal fin, anal fin, pectoral fin, and finlets to isolate the effects of the tail fin. Our resulting reduced-order model is based on 11 critical measurements of the original high-fidelity tuna model and scaled to a whole-body length  $l$  of 350 mm (Figure. 6.1).

Our model was 3D-printed in multiple parts: a fixed head, a tail frame, a tail shell, a tail joint, a tail fin connector, and a tail fin (Figure. 6.1c). All parts except the tail joint were 3D-printed in nylon by a Selective Laser Sintering (SLS) printer. Nylon was chosen because it is naturally waterproof. To complete the platform waterproofing, we used silicone gel to seal the gap between the tail frame and the tail shell (Figure. 6.1c). The tail joint and tail

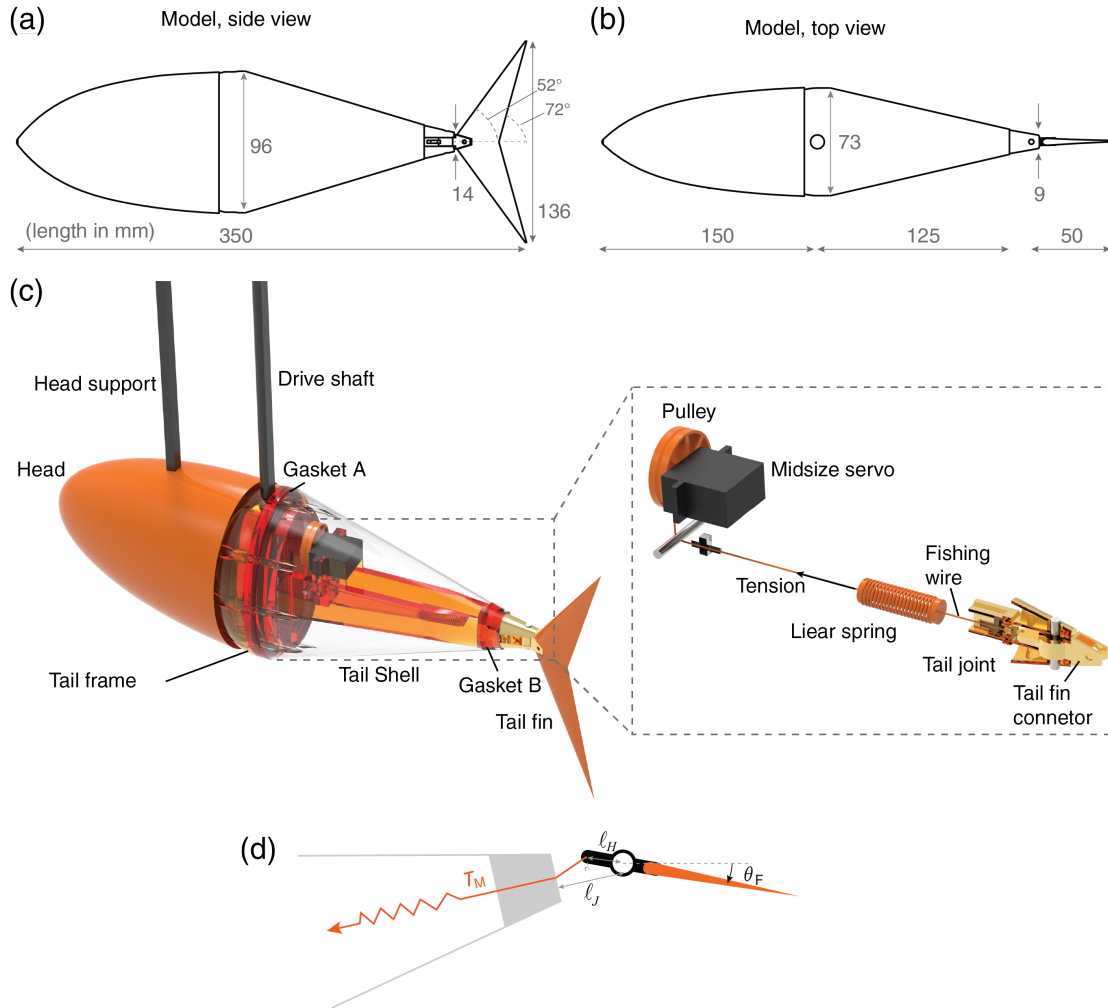


Figure 6.1: **Tuna-inspired reduced-order platform with adjustable stiffness tail joint.** (a,b) Side and top views of the reduced-order tuna-inspired platform (lengths in mm). (c) Rendering of the 3D model with the tail made transparent to reveal internal structures. The head is fixed by a carbon fiber shaft (6.35 mm diameter), and the tail is driven by a rotating carbon fiber drive shaft (12.7 mm diameter). Insert: a midsize servo installed inside the tail adjusts the effective torsional stiffness of the tail joint. (d) Diagram of tail joint that convert muscle tension to joint stiffness.  $\ell_H = 11.6$  mm ,  $\ell_J = 15$  mm.

fin connector were 3D-printed in stainless steel by a Direct Metal Laser Sintering (DMLS) printer. Stainless Steel was chosen due to the high cyclical stresses on the tail joint.

To control the stiffness of the peduncle in real-time, we installed a high torque digital servo (Hitech HS-7245MG) inside the tail frame. The servo pulled on a thin polyethylene line (Spectra, 20 lbs. max load), which pulled on a linear spring then pulled on the front end of the tail fin connector. Thus, the servo acted like an axial tendon that increased the effective torsional stiffness of the tail joint. While real tuna have skeletal structures that limit tail joint angles, we left off a mechanical stop in order to eliminate any imposed constraints on tail fin kinematics. Based on the geometry of the tail fin connector (Figure. 6.1*d*), we expect the torque/moment on the fin ( $M_T$ ) to depend on pitch angle ( $\theta_F$ ) and muscle/spring tension ( $T_M$ ):

$$M_T = \ell_J \sin \left( \tan^{-1} \frac{\ell_H \sin \theta_F}{\ell_J - \ell_H \cos \theta_F} \right) \left( T_M + ks \left( \sqrt{\ell_H^2 + \ell_J^2 - 2\ell_J \ell_H \cos \theta_F} - \ell_J + \ell_H \right) \right) \quad (\text{Eq. 6.1})$$

where  $ks$  is the spring coefficient, and  $\ell_H$  and  $\ell_J$  are dimensions of the tail fin connector (Figure. 6.1*d*). For small angles, Eq. 6.1 approximately reduces to

$$M_T = \zeta T_M \theta_F \quad (\text{Eq. 6.2})$$

where  $\zeta$  is a constant determined by the dimensions of the tail fin connector. When creating Figure. 6.3*e-f*, we applied four uniformly-spaced  $T_M$  values to Eqs.6.1 and 6.2, and we added an offset to  $T_M$  so that the caudal had finite torsional stiffness even when  $T_M = 0$ . The offset represents the internal tension due to muscle and skin tissues in the real tuna tails. Eqs.6.1 and 6.2 explain why our robotic joint and our model behave like tuned torsional springs (Figure. 6.3*e-f*). As pitch angle ( $\theta_F$ ) increases, so does the restoring torque/moment ( $M_T$ ), and the effective torsional stiffness coefficient is  $\zeta T_M$ , i.e. it increases with muscle tension.

### 6.1.3 Self-propelled swimming performance test

To test the swimming performance of the tuna-inspired platform, we built a custom-rig that suspended the platform into the  $380 \times 450 \times 1520$  mm ( $W \times H \times L$ ) test section of a closed-loop water channel (Rolling Hills 1520, 0-1 m/s). We used the rig for traditional force measurements, variable-speed semi-autonomous missions, and 3D Particle Image Velocimetry.

To determine the platform's *swimming speed*, we used a Newton-Raphson zero-finding scheme. Based on preliminary tests of the actuator, we chose steady swimming speeds ranging from 100 mm/s to 700 mm/s ( $0.29 \sim 2$  full body lengths/s) with 50 mm/s intervals. For each speed, we set the water channel to that speed, then sought the tailbeat frequency ( $f$ ) that caused net thrust ( $\overline{F_T}$ ) to be zero. The scheme repeated at each swimming speed, and each speed was repeated with 18 different spring tensions. Cases were omitted if the desired speed was unattainable at the maximum tailbeat frequency. Every combination of speed and tension was tested five times. The result is a function mapping frequency and stiffness to speed ( $u(f, T_M)$ , Figure.6.4a). Details of the Newton-Raphson zero-finding scheme can be found in section 2.4.

To determine the platform's *swimming efficiency*, we divided speed by the average mechanical power consumption of the motor:  $\xi \equiv u/\overline{p}_{\text{motor}}$ . This ratio gives a measure of the model's range, or distance traveled per unit energy. To estimate average mechanical power consumption, we derived an expression for motor power as a function of tail fin kinematics. To calculate the mechanical power of the DC motor, we followed the energy transfer from the motor to the fin. The motor exerts a moment on the pin of the eccentric wheel, and this moment is the cross product of a moment arm and a force:

$$\vec{M}_{\text{motor}} = \vec{r}_{\text{pin}} \times \vec{F}_{\text{pin}} \quad (\text{Eq. 6.3})$$

where  $\vec{F}_{\text{pin}}$  is the force on the pin and  $\vec{r}_{\text{pin}}$  is the vector from the motor's axis of rotation

to the pin (Figure. B.3). Because of the direction of the slot, the forces on the pin are always in the  $y$  direction and are zero when the tail fin's pitch angle is at its maxima. Thus, the moment on the pin varies sinusoidally through the tailbeat cycle, and its magnitude varies according to

$$|\vec{M}_{\text{motor}}| = |\vec{r}_{\text{pin}}| |\vec{F}_{\text{pin}}| |\sin(T)| \quad (\text{Eq. 6.4})$$

The magnitude of the moment arm ( $|\vec{r}_{\text{pin}}|$ ), is a constant determined by the amplitude module ( $d$ ), and the force on the pin ( $\vec{F}_{\text{pin}}$ ) is equal to the hydrodynamic z-axis moment on the fin ( $M_{z,\text{fin}}$ ) times the lever ratio  $1/\ell_P$ :

$$|\vec{M}_{\text{motor}}| = d \frac{|M_{z,\text{fin}}|}{\ell_P} |\sin(T)| \quad (\text{Eq. 6.5})$$

Eq. 6.5 is sensitive to the phase offset between  $|M_{z,\text{fin}}|$  and  $|\sin(T)|$ , so we used the measured pitch angle to calculate  $|\sin(T)|$  rather than using the commanded pitch angle. Because the pitch angle ( $\theta$ ) varies with cosine, we used the numerical derivative of pitch angle divided by its peak value ( $\dot{\theta}_{\text{max}}$ ):

$$|\vec{M}_{\text{motor}}| = d \frac{|M_{z,\text{fin}}|}{\ell_P} \frac{|\dot{\theta}|}{|\dot{\theta}_{\text{max}}|} \quad (\text{Eq. 6.6})$$

Instantaneous electrical power to the motor is  $IV$ , where  $I$  and  $V$  are the current and voltage to the motor. For a DC motor, the current and voltage can be estimated as

$$I = C_\tau |\vec{M}_{\text{motor}}| + I_0, \text{ and } V = C_V f, \quad (\text{Eq. 6.7})$$

where  $C_\tau$  is the torque-current constant (3.3 A/Nm for our motor),  $I_0$  is the no-load current (0.78 A for our motor), and  $C_V$  is the frequency-voltage constant (2.5 V/Hz for our motor). Substituting our expression for motor moment (Eq. 6.4) gives

$$p_{\text{motor}} = \left( C_\tau d \frac{|M_{z,\text{fin}}|}{\ell_P} \frac{|\dot{\theta}|}{|\dot{\theta}_{\text{max}}|} + I_0 \right) (C_V f) \quad (\text{Eq. 6.8})$$

which is an expression for power in terms of measured quantities ( $\dot{\theta}$ ,  $M_{z,\text{fin}}$ ), prescribed quantities ( $d$ ,  $f$ ) and experimental constants ( $C_\tau$ ,  $\ell_P$ ,  $I_0$ ,  $C_V$ ). For efficiency calculations, we used the power averaged over 20 pitching cycles. The result is a function mapping frequency and stiffness to efficiency ( $\xi(f, T_M)$ , Figure. 6.4b).

#### 6.1.4 Variable speed swimming mission test

To simulate more realistic missions (Figure. 6.6 and Figure. B.5), we used air bushings to allow the platform to move freely in the horizontal plane. The bushings glide along horizontal stainless steel rails while two laser distance sensors measure the carriage's  $x$  and  $y$  position (Figure. B.4a-b). Four independently-controlled linear actuators raise/lower each corner of the carriage support frame (1204 leadscrews with NEMA 57 stepper motors and braking clutches). We used the actuators to level the air bushing system to within  $\pm 0.001^\circ$  before each experiment. The bushings were present in the speed and efficiency measurements (Figure. 6.4), but they were turned off and therefore nonfunctional. Details of the two-axis air suspension system and data acquisition are described in section 2.1.2, and 2.1.6.

We used our air bushing setup to simulate four free-swimming missions. In each mission, the speed of the water channel increased from 0.1 m/s to 0.65 m/s in intervals of 0.025 m/s. At each speed, the platform swam 9 m, resulting in a total distance of 207 m (the longest mission possible on one compressed air tank). The platform kept up with the incoming flow by controlling its frequency with an on-board PD-controller ( $k_P = 0.05$  Hz/cm,  $k_D = 2.53$  Hz/cm $\cdot$ s $^{-1}$ ).

The four missions were designed to test the robustness of the stiffness-tuning strategy; each considered a different modification (Figure. B.5c):

- *Mission 1*: Streamwise (fore-aft) air bushings on. Platform free to move forward/backward. A PD controller maintained the platform's speed by modulating frequency.

- *Mission 2*: All air bushings on. Platform free to move forward/backward/left/right. A second PD controller ( $k_P = 1^\circ/\text{cm}$ ,  $k_D = 1.18^\circ/\text{cm}\cdot\text{s}^{-1}$ ) kept the platform centered in the channel by modulating pitch bias.
- *Mission 3*: All air bushings on. A second PD controller kept the platform on a serpentine route ( $y_{\text{goal}} = 10 \sin(0.1\pi t)$  cm) by modulating pitch bias.
- *Mission 4*: All air bushings on. Tailbeat amplitude 33% higher than Missions 1-3. A second PD controller kept the platform centered in the channel by modulating pitch bias.

If the platform was unable to keep up with the flow, the flow was coerced to the highest attainable speed. The “loose” stiffness case reached a max speed of 0.275 m/s; the “rigid” stiffness reached a max speed of 0.475 m/s; the “medium” stiffness reached the highest requested speed (0.650 m/s) (Figure. B.5c). Speed limits were pre-determined based on Fig 2A at 5.0 Hz so that unattainable speeds were not requested during the missions.

### 6.1.5 Modified Tunabot construction and experiment

To test our predictions on a fully autonomous platform, we used a modified version of the Tunabot (9). In place of rubber bands and a mechanical stop, we used a rectangular ( $4 \times 35$  mm) leaf spring to control tail stiffness (Figure. 6.2). Four different stiffness leaf springs were chosen to explore stiffness effects on the Tunabot’s performance.

We used as few light tethers as possible to create steady, straight swimming for the Tunabot. The Tunabot has negative buoyancy and no control surfaces, so we used two thin polyethylene (Spectra) lines to suspend the Tunabot in the water channel’s test section. The lines ensured level horizontal swimming. We used a third line connected to the Tunabot’s nose and the opposite wall to limit yaw motions. Two flexible ( $\sim 1$  mm diameter) wires entered the Tunabot at about 33% of the body length from the tip of the nose. These wires

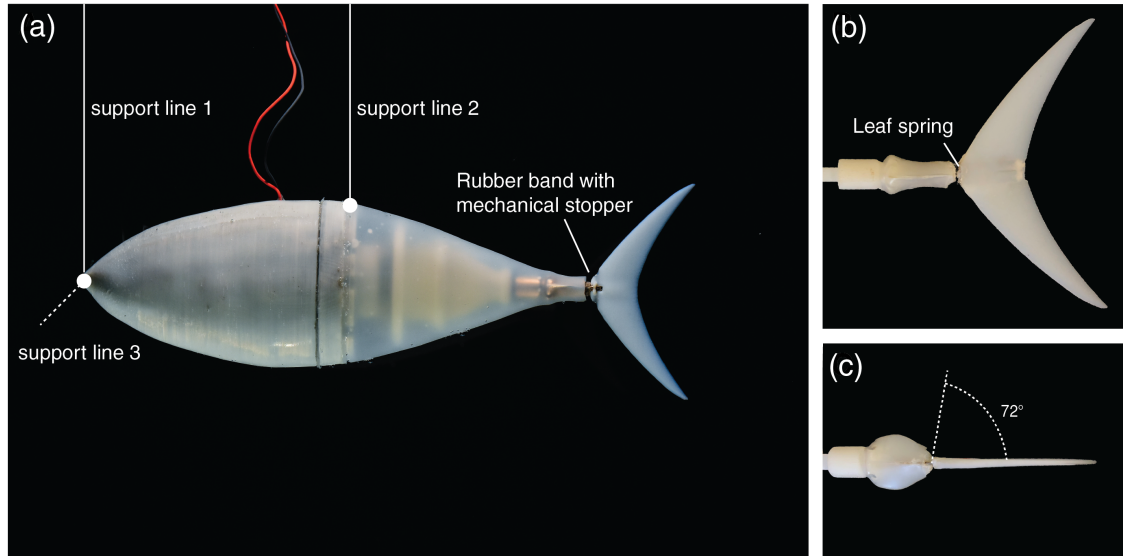


Figure 6.2: **Tunabot with modified tail joint design.** (a) Original Tunabot design. A pair of elastic bands gave a constant stiffness to the tail joint. The maximum tail fin pitch angle was constrained to  $\pm 15^\circ$  by a mechanical stop. (b) Our modified design uses a leaf spring to connect the tail joint to the tail fin. We changed the thickness of the leaf spring (1095 spring steel) to adjust the fixed stiffness of the joint. (c) The modified design had no mechanical stop (max tail fin pitch angle of  $\pm 72^\circ$ ).

coupled the controller to the internal DC motor to regulate the rotation speed (RPM). A similar setup was used in the first study using the Tunabot (9).

To measure the self-propelled speed and efficiency of the Tunabot, we tuned its frequency manually and measured electrical power consumption. A vertically-installed high-speed camera recorded the bottom view of the water channel and displayed on a PC in real time. We used the images to first mark the location of the Tunabot's nose viewed from the bottom of the water channel with no incoming flow. This location served as the reference zero position in subsequent images. The water channel's speed was then varied from 200 mm/s to 650 mm/s in 50 mm/s increments. When approaching the maximum speed of test case, the increment was reduced to get finer measurement resolution. For each flow speed, the frequency was adjusted until the nose returned to the zero position, indicating that the Tunabot was assumed to be self-propelled (no streamwise forces from the tethers). At the self-propelled condition, we recorded the flow speed and the voltage

and current going to the Tunabot. Multiplying the voltage and current gave an estimate of average power consumption, and the efficiency was estimated as speed divided by average power consumption. We computed the actual frequency by using 200 images captured with the bottom camera at 1000 Hz. We ran the tests in random sequence and repeated 3 times to prevent any effects of actuator deterioration. The average standard deviation of measurements are  $\sigma_f = 0.3$  Hz on frequency and  $\sigma_{\text{efficiency}} = 7.3$  m/kJ on efficiency.

## 6.2 Mathematical modeling of robot fish with tunable stiffness tail

### 6.2.1 Deriving the tail fin model

We modelled the tail fin as a rigid thin airfoil connected to the tail via a torsional spring. The pitching tail prescribes the lateral position of the tail fin's leading edge,  $h(t)$  and the spring causes a passive response in the tail fin's pitch angle,  $\theta_F(t)$  (Figure. 6.3). To determine the forces/moments on the tail fin, we used the Garrick model that estimates the hydrodynamic lift and moment per-unit-span on pitching/heaving airfoils.

The Garrick model (34) defines lift and torque phasors as

$$L_H^* = -\frac{\pi\rho c^2}{4} \left[ u\dot{\theta} + \ddot{h} + \frac{c}{2}\ddot{\theta}\pi + 4C_{\text{def}}\frac{u}{c} \left( \dot{h} + u\theta + \frac{3}{4}c\dot{\theta} \right) \right] \quad (\text{Eq. 6.9})$$

$$M_H^* = -\frac{\pi\rho c^2}{4} \left[ \frac{c}{2}\ddot{h} + \frac{3uc}{4}\dot{\theta} + \frac{9}{32}c^2\ddot{\theta} + C_{\text{def}}u \left( \dot{h} + u\theta + \frac{3}{4}c\dot{\theta} \right) \right] \quad (\text{Eq. 6.10})$$

where  $\rho$  is the density of the surrounding fluid,  $c$  is the chord length of the tail fin,  $u$  is the forward speed of the airfoil, dots denote time derivatives,  $C_{\text{def}}$  is the Theodorsen Lift Deficiency Function,  $\theta$  here is the pitch angle of airfoils which is the  $\theta_F$  in our case. The

Theodorsen Lift Deficiency Function is  $C_{\text{def}} \equiv F + iG$ , where  $F$  and  $G$  are defined as

$$F \equiv \frac{J_1(k)[J_1(k)+Y_0(k)]+Y_1(k)[Y_1(k)-J_0(k)]}{[J_1(k)+Y_0(k)]^2+[Y_1(k)-J_0(k)]^2} \text{ and } G \equiv \frac{Y_1(k)Y_0(k)+J_1(k)J_0(k)}{[J_1(k)+Y_0(k)]^2+[Y_1(k)-J_0(k)]^2} \quad (\text{Eq. 6.11})$$

with  $J_0$  and  $J_1$  being zeroth- and first-order Bessel functions of the first kind,  $Y_0$  and  $Y_1$  being zeroth- and first-order Bessel functions of the second kind, and  $k$  being the reduced frequency:  $\pi fc/u$  where  $f$  is frequency. In this formulation, the lift and moment phasors are complex, as are the heave and pitch angles. Real-valued lifts and moments can be evaluated by, for example, taking the real component of each:  $L_H = \text{Re}(L_H^*)$  and  $M_H = \text{Re}(M_H^*)$ . For the harmonic motions we consider here,  $h = h_0 e^{i(2\pi ft)}$  and  $\theta = \theta_0 e^{i(2\pi ft - \phi)}$ , where  $h_0$  and  $\theta_0$  are heave and pitch amplitudes and  $\phi$  is the heave-pitch phase-offset.

In our model, the tail fin experiences a tendon-driven moment,  $M_T$ , in addition to the hydrodynamic moment. Motivated by measurements on tuna tendons (Figure. 6.3a), we assumed that  $M_T = \zeta T_M (\theta_F - h/\ell_T)$ , where  $T_M$  is the tension in the tendon-inspired spring,  $\zeta$  is a constant that converts tendon tension to an effective torsional spring constant,  $\ell_T$  is the length of the tail (Figure. 6.3g),  $\theta_F$  is the passive pitching angle of the tail fin and  $h = \ell_T \theta_T$  which is prescribed by tail pitching motion  $\theta_T = \theta_0 e^{i(2\pi ft)}$ . We assumed that the moment of inertia of the tail fin itself was negligible compared to its added mass. To motivate this assumption, we considered that  $m \bar{\ell}_F^2 / (\rho s \bar{\ell}_F^4) \approx 0.01$ , where  $m$  is the mass of the tail fin (4.5 g),  $s$  is the span of the tail fin (136mm) and  $\bar{\ell}_F$  is the average tail fin length (50 mm). The equation governing the pitch angle of the tail fin is therefore  $0 = M_S + M_H$ . This equation can be written non-dimensionally as

$$0 = \tau^2 \left( \theta_F - \frac{H}{L_T} \right) - \pi^2 \left[ \frac{\pi \ddot{H}}{S^2} + \frac{3\dot{\theta}_F}{4S} + \frac{9\pi\ddot{\theta}_F}{16S^2} + C_{\text{def}} \left( \frac{\dot{H}}{S} + \frac{\theta_F}{2\pi} + \frac{3\dot{\theta}_F}{4S} \right) \right] \quad (\text{Eq. 6.12})$$

where the chord length  $c$  in the Garrick model was replaced with the average tail fin

length,  $\bar{\ell}_F$ , and non-dimensional parameters have been introduced as follows:

- Dots indicate dimensionless time derivatives, that is,  $\partial/\partial T$ , where  $T \equiv 2\pi ft$ .
- $H \equiv h/\bar{\ell}_F$  and  $L_T \equiv \ell_T/\bar{\ell}_F$  are the lateral position (heave) of the tail fin and the length of the tail scaled by the tail fin length. Note that for the harmonic heave motions we are considering,  $H = H_0 e^{iT} \equiv (h_0/\bar{\ell}_F) e^{iT}$ . When validating our model, we used the same heave amplitude as in the experiments:  $H_0 = 0.64$ .
- $\tau \equiv \sqrt{\zeta T_M / (\rho u^2 \bar{\ell}_F^3 / 2)}$  (or  $\gamma \sqrt{T_M} / u$  where the constant  $\gamma \equiv \sqrt{\zeta / (\rho \bar{\ell}_F^3 / 2)}$ ) is the “scaled muscle tension”; it represents a ratio of strengths between spring-driven torques and hydrodynamic torques. Note that  $\tau$  is a close cousin of the Cauchy number, which is a ratio of elastic forces and hydrodynamic forces.
- $S \equiv u/(f\ell)$  is the stride length; it represents the number of body-lengths traveled per tailbeat. Note that  $S$  is inversely proportional to the reduced frequency ( $S = \pi \bar{\ell}_F / (k\ell)$ , where  $k$  is reduced frequency).

Eq.6.12 can be rearranged to have the passive outputs on the left and the active inputs on the right, revealing that the pitch angle behaves like a damped oscillator:

$$\ddot{\theta}_F + \frac{16S^2}{9\pi^3} \left( \frac{\pi C_{\text{def}}}{2} + \tau^2 \right) \theta_F + \frac{4S}{3\pi} (1 + C_{\text{def}}) \dot{\theta}_F = \frac{16}{9} \left( \frac{\tau^2 S^2}{\pi^3} \frac{H}{L_T} - \frac{C_{\text{def}} S}{\pi} \dot{H} - \ddot{H} \right) \quad (\text{Eq. 6.13})$$

Such an oscillator has an exact solution for harmonic heave motions (see, e.g., [134]), which allows us to write the solution for pitch angle as

$$\theta_F = \theta_0 e^{i(T-\phi)},$$

where

$$\theta_0 = \frac{16H_0}{9} \sqrt{\frac{\frac{C_{\text{def}}^2 S^2}{\pi^2} + \left(1 + \frac{S^2 \tau}{\pi^3 L_T}\right)^2}{\frac{16(1+C_{\text{def}})^2 S^2}{9\pi^2} + \left[1 - \frac{8S^2(\pi C_{\text{def}} + 2\tau)}{9\pi^3}\right]^2}}$$

and

$$\phi = \text{ArcTan} \left[ \frac{12(1 + C_{\text{def}})\pi^2 S}{8S^2(2\tau + \pi C_{\text{def}}) - 9\pi^3} \right] + \text{ArcTan} \left[ \frac{C_{\text{def}}L_T\pi^2 S}{\pi^3 L_T + \tau S^2} \right] \quad (\text{Eq. 6.14})$$

Eq.6.14 was used to make the kinematic model predictions used in Figure. 6.5. The lateral position of the tail fin's trailing edge follows directly from the fin's heave ( $h$ ) and pitch ( $\theta_F$ ):

$y_{\text{TE}} = h + \bar{\ell}_F \sin \theta_F \approx h + \bar{\ell}_F \theta_F$ . Therefore, Eq.6.13 can be reformulated as an equation for  $y_{\text{TE}}$ :

$$\ddot{y}_{\text{TE}} + \frac{16S^2}{9\pi^3} \left( \frac{\pi C_{\text{def}}}{2} + \tau^2 \right) y_{\text{TE}} + \frac{4S}{3\pi} (1 + C_{\text{def}}) \dot{y}_{\text{TE}} = \bar{\ell}_F \left( \frac{16}{9} \left( \frac{\tau^2 S^2}{\pi^3} \frac{H}{L_T} - \frac{C_{\text{def}} S}{\pi} \dot{H} - \ddot{H} \right) + \frac{16S^2}{9\pi^3} \left( \frac{\pi C_{\text{def}}}{2} + \tau^2 \right) H \right) \quad (\text{Eq. 6.15})$$

If we assume complex forcing,  $H = H_0 e^{iT}$ , then all of the forcing on the right can be written as  $H_0 e^{iT} * \zeta$ , where  $\zeta$  is a complex function of  $C_{\text{def}}$ ,  $L_T$ ,  $\tau$  and  $S$ . We chose to highlight this feature by writing the right-hand side of Eq.6.15 as  $F(\theta_T(t))$  in the main manuscript; we felt that this best illustrated what we consider the key feature of Eq.6.15: that the lateral position of the tail fin's trailing edge behaves like a damped oscillator which can be tuned to resonance by adjusting  $\tau$ .

## 6.2.2 Model predictions for free-swimming

For a given stride length  $S$  and scaled muscle tension  $\tau$ , we can use Eq.6.15 to calculate the full kinematics of the tail fin. However, because the forward speed  $u$  is an output of tail fin kinematics,  $S$  and  $\tau$  (whose definitions both include  $u$ ) cannot be prescribed *a priori*. In fact, in free-swimming conditions, where the streamwise forces sum to zero,  $S$  and  $\tau$  are functions of each other. To discover this interdependence, we added an established model of net streamwise force,  $F_T$ , for heaving/pitching airfoils (75). We then set that force equal

to zero to represent free-swimming:

$$\overline{F}_T = \frac{1}{2}\rho u^2 \ell_F^2 \left[ C_T \left( \frac{f a_{TE}}{u} \right)^2 - C_D \left( \frac{\ell}{\ell_F} \right)^2 \right] = 0 \quad (\text{Eq. 6.16})$$

where  $C_T$  and  $C_D$  are constant thrust and drag coefficients ( $C_D \equiv \text{Drag}/(0.5\rho u^2 \ell^2)$ ,  $C_T \equiv \text{Thrust}/(0.5\rho u^2 \ell_F^2)$ ). and  $a_{TE}$  is the tip-to-tip amplitude of the tail fin's trailing edge. We calculated  $C_D$  of the non-thrust producing elements (head) to be 0.046 (Section S1.4), and we used the unknown thrust coefficient  $C_T$  as a fitting parameter. Because the tail fin kinematics are fully prescribed for a given  $S$  and  $\tau$ , so too is  $a_{TE}$  prescribed for a given  $S$  and  $\tau$ . Therefore, Eq.6.15 has two variables,  $S$  and  $\tau$ , and can be used to determine  $S$  for a given  $\tau$  or vice versa. Note: this argument does not rely on the specific thrust model used in Eq.6.16; the interdependence of  $S$  and  $\tau$  would be a consequence of any kinematics-dependent thrust model.

The specific  $S$ - $\tau$  dependence predicted by Eq.6.15 is supported by the experimental data (Figure. 6.4). When  $S$  is plotted against  $\tau$  for all free-swimming conditions tested, we find that as  $\tau$  increases,  $S$  rises sharply, experiences a local maximum, then tapers off slowly. Using a single parameter fit of Eq.6.16 ( $C_T = 2.4$  to minimize residuals), we found that the model could capture these trends well. The fitted model can be used, for example, to recreate speed and efficiency contour plots similar to those in Figure. 6.4a. We used this value for  $C_T$  to plot the model kinematics (Figure. 6.5b) and the model  $S$ - $\tau$  curve (Figure. 6.5a). A fit is expected to be necessary, because Equations 6.9 and 6.10 are derived for 2D airfoils. For finite-aspect-ratio wings/fins, the forces and moments are affected by 3D flows that attenuate pressure gradients across the fin. Our experiments showed that the qualitative trends were similar enough that a single parameter fit could capture the efficiency trends.

### 6.2.3 Model implications for efficiency

Our model predicts that a certain  $\tau$  value maximizes stride length, but is stride length necessarily correlated with swimming efficiency? To answer this question, we explored how stride length affects efficiency based on the model.

To calculate efficiency, we first estimated the power consumption of the drive motor based on the modeled forces on the tail fin. The procedure is the same as the procedure for estimating power consumption in the experiments (Section S1.3), except that instead of the measured torque on the driveshaft, we used the modeled hydrodynamic force on the fin. For completeness, we repeat the procedure here using the model notation.

The moment that motor exerts on the pin of the eccentric is given in Eq 6.4. In the model, the magnitude of the force on the pin ( $|\vec{F}_{\text{pin}}|$ ) is proportional to the hydrodynamic lift on the tail fin ( $L_H$ ). The proportionality constant is the lever ratio  $\ell_P/\ell_T$ , where  $\ell_P$  is the distance from the tail's axis of rotation to the Scotch yoke and  $\ell_T$  is the distance from the Scotch yoke to the tail fin's leading edge (Figure. B.3). The average moment on the pin is therefore

$$\overline{|\vec{M}_{\text{motor}}|} = \overline{|\vec{r}_{\text{pin}}| |\vec{F}_{\text{pin}}| |\sin(T)|} = d_{\text{pivot}} \frac{\ell_P}{\ell_T} |L_H^*| \frac{2}{\pi} \quad (\text{Eq. 6.17})$$

where  $L_H^*$  is given by Eq.6.9, and the average mechanical power exerted by the motor is

$$\overline{p_{\text{motor}}} = 2\pi f \overline{|\vec{M}_{\text{motor}}|} = 4f d_{\text{pivot}} \frac{\ell_P}{\ell_T} |L_H^*| \quad (\text{Eq. 6.18})$$

To consider how this power varies with stride length, we introduce  $L_H^*$  using Eq.6.9 and rearrange terms to isolate stride length:

$$\overline{p_{\text{motor}}} = 4f d_{\text{pivot}} \frac{\ell_P}{\ell_T} |L_H^*| = 2\pi^2 f \rho u^2 \bar{\ell}_F^2 d_{\text{pivot}} \frac{\ell_P}{\ell_T} \left| \frac{2\pi}{S^2} \dot{H} + \frac{1}{S} \dot{\theta} + \frac{\pi}{S^2} \ddot{\theta} - 2C_{\text{def}} \left( \frac{\theta}{\pi} + \frac{2}{S} \dot{H} + \frac{3}{2S} \dot{\theta} \right) \right| \quad (\text{Eq. 6.19})$$

The swimming efficiency based on mechanical power alone is

$$\xi = \frac{u}{\overline{p_{\text{motor}}}} = \frac{1}{2\pi^2 f \rho u \bar{\ell}_F^2 d_{\text{pivot}} \frac{\ell_P}{\ell_T} \left| \frac{2\pi}{S^2} \ddot{H} + \frac{1}{S} \dot{\theta} + \frac{\pi}{S^2} \ddot{\theta} - 2C_{\text{def}} \left( \frac{\theta}{\pi} + \frac{2}{S} \dot{H} + \frac{3}{2S} \dot{\theta} \right) \right|} \quad (\text{Eq. 6.20})$$

The efficiency goes to infinity as  $f$  and  $u$  go to zero.. Thus, to maximize hydrodynamic efficiency alone, the tuna should swim as slowly as possible. However, all real processes have background power consumption, which invalidates this argument. Fish, for example, have basal metabolic rates, and our tuna-inspired platform has a no-load current  $I_0$ . We propose that a better estimate of the motor power comes from using the current  $I$  and voltage  $V$  going to the motor:

$$\overline{p_{\text{motor}}} = (I)(V) = \left( C_\tau \overline{|\vec{M}_{\text{motor}}|} + I_0 \right) (C_V f) \quad (\text{Eq. 6.21})$$

where  $C_\tau$  is the torque-current constant for the motor and  $C_V$  is the frequency-voltage constant of the motor. Substituting our expression for motor moment (Eq.6.17) into this new formulation gives

$$\overline{p_{\text{motor}}} = \left( \frac{2}{\pi} C_\tau d_{\text{pivot}} \rho u \bar{\ell}_F^2 \frac{\ell_P}{\ell_T} \left| \frac{2\pi}{S^2} \ddot{H} + \frac{1}{S} \dot{\theta} + \frac{\pi}{S^2} \ddot{\theta} - 2C_{\text{def}} \left( \frac{\theta}{\pi} + \frac{2}{S} \dot{H} + \frac{3}{2S} \dot{\theta} \right) \right| + I_0 \right) C_V f \quad (\text{Eq. 6.22})$$

and the swimming efficiency is

$$\xi = S \left( \frac{2}{\pi} f u C_\tau C_V d_{\text{pivot}} \rho \bar{\ell}_F^2 \frac{\ell_P}{\ell_T} \left| \frac{2\pi}{S} \ddot{H} + \dot{\theta} + \frac{\pi}{S} \ddot{\theta} - 2C_{\text{def}} \left( \frac{\theta S}{\pi} + 2\dot{H} + \frac{3}{2} \dot{\theta} \right) \right| + \frac{I_0 C_V}{\bar{\ell}_F} \right)^{-1} \quad (\text{Eq. 6.23})$$

The role of stride length is now clearer. In general, efficiency increases directly with stride length. Only one term in Eq.6.23 shows an inverse relationship between efficiency

and stride length, but this term represents quasi steady lift on the tail fin and is dwarfed by the other terms in this  $O(1)$  Strouhal number flow. All other terms show efficiency increasing monotonically with stride length. Note that with the addition of the no-load current, the efficiency remains finite as  $f$  and  $u$  go to zero:

$$\lim_{f,u \rightarrow 0} \xi = S \frac{\bar{\ell}_F}{I_0 C_V}$$

The prediction that efficiency scales with stride length is supported by the experiments. When coloring each point by its efficiency, we found that higher stride lengths corresponded to higher efficiencies (Figure. 6.4).

## 6.3 Results

### 6.3.1 Tuna tails inspire theory and experiments with tunable stiffness

We chose tuna (family Scombridae) for our model organism, because they are high-speed, high-efficiency apex predators [14, 15]. Tuna have paired lateral tendons that pass from anterior muscles through the tail joint (peduncle) and onto tail/caudal fin rays [135] (Figure. 6.3*a*). As the sum force on these tendons increases, so too does the effective stiffness of the tail (Figure. 6.3*b*). Muscles and tendons often exhibit strut- or spring-like behaviors [136, 137], and we speculated that a simple mechanical model could explain stiffness tuning in tuna-like swimming as it pertains to performance.

Our biomechanical model recreates the basic stiffening response of real tensioned tuna tails. The model treats the tuna as two parts: a “head” that generates drag and a “tail” that generates thrust (Figure. 6.3*c*). The front of the tail pitches back and forth and drives the lateral heaving motions of the tail joint, and the tail joint supports a passive fin that is

tensioned by a muscle-inspired spring. In our model, increasing the force on the spring ( $T_M$ ) increases the effective torsional spring coefficient of the tail joint (Figure. 6.3d).

To test our theoretical model, we built a tuna-like platform that tunes its own tail stiffness using a motor-driven “muscle” (spring) (Figure. 6.3e). As with the biological and theoretical tail joint, pulling harder on the spring increases the torsional stiffness of the tail (Figure. 6.3f). To test the platform over the wide range of kinematics seen in real tuna, we built a custom actuator that pitches our robotic tail at high frequencies (up to 6 Hz) while also tuning amplitude (0–35°) and pitch bias (0–20°) (Figure. 6.3g). While real fish muscles both tune stiffness and actuate fins [72, 63], our platform uses two separate systems (Figure. 6.3e,g), which allows us to decouple active stiffness control from locomotion.

### 6.3.2 Maintaining high speed and efficiency with tunable stiffness

To predict swimming speed and efficiency, we combined our biomechanical model with thin airfoil theory (Joseph Katz and Plotkin 2001), which gives the forces and torques on heaving/pitching hydrofoils. We treated the tail fin as a hydrofoil whose heave was prescribed by our actuator and whose pitch angle responded passively based on hydrodynamic forces and the spring tension ( $T_M$ ). To test the model predictions, we tested our tuna-like platform over a grid of tailbeat frequencies and spring tensions (841 total trials) as it self-propelled (Thrust = Drag) in a water channel (Figure. 6.3h).

We found that swimming speed and efficiency (speed / input power) are highly dependent on tail stiffness. At low frequencies, swimming speed ( $u$ ) rises linearly with frequency ( $f$ ) (Figure. 6.4a), as it does in real fish [39]. A linear frequency-speed relation implies a constant “stride length”, i.e. body-lengths traveled per tailbeat, or  $u/(f\ell)$  where  $\ell$  is body length. If stiffness stays constant and frequency rises further, stride length and efficiency begin to decline (Figure. 6.4a, insert). To maintain high efficiency, stiffness must increase with swimming speed. A fish or robot could keep a look-up table of optimal stiffnesses, but such a black-box strategy would have limited scope. We used our model to seek a more

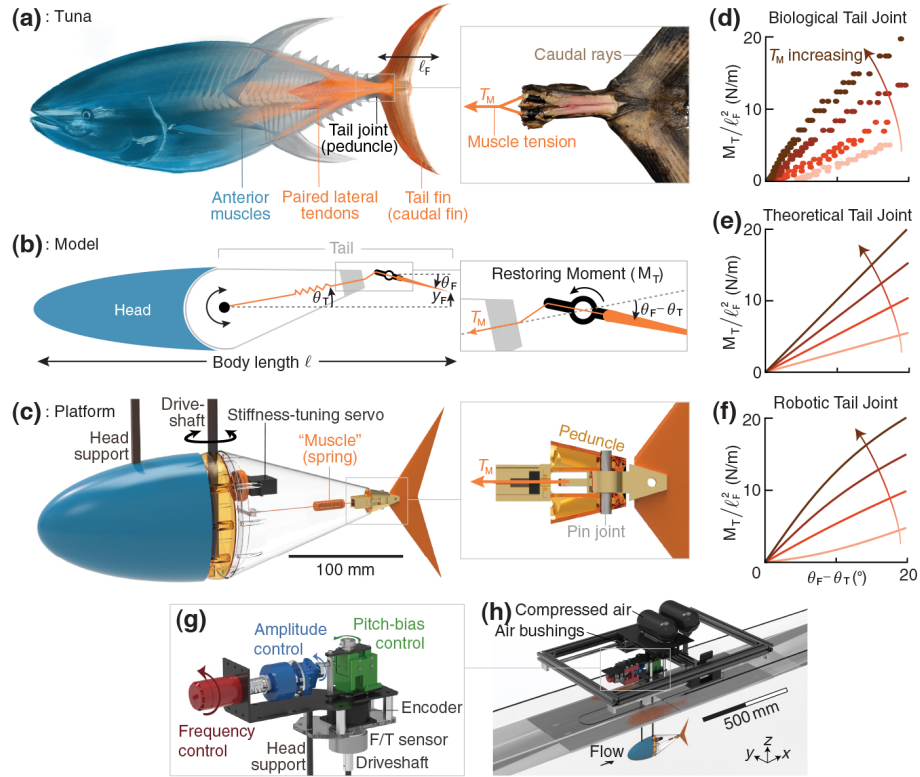


Figure 6.3: **A tail with tunable stiffness was modeled after tuna.**(a) In tuna tails, paired lateral tendons connect anterior body muscles to rays of the caudal fin. (b) Simplified model: The tail is pitched back and forth at an angle  $\theta_T$ , and the tail fin responds passively. (c) In our platform, a servo tightened a spring to adjust tail stiffness. The robot's head was fixed while its tail was pitched by a driveshaft. (d) A dissected tuna tail (see Supp. Figure. B.1 for other tails,  $N = 6$ ) exhibited behaviors of a tuned torsional spring. When a force ( $T_M$ ) was applied to the lateral tendons, the restoring torque of the peduncle rose faster with fin pitch angle ( $\theta_F$ ). (e-f) The model and robotic tail also behave like tuned springs (1-parameter fit to match tuna tail see section 6.1.2). (g) A Scotch-yoke mechanism adjusted the frequency, amplitude, and pitch-bias of the driveshaft. An absolute encoder and a torque sensor recorded mechanical power input. (h) The platform was suspended in a recirculating water channel ( $W: 380 \text{ mm} \times H: 450 \text{ mm} \times L: 1520 \text{ mm}$ ) and could float in a horizontal plane due to a two-axis air bushing system.

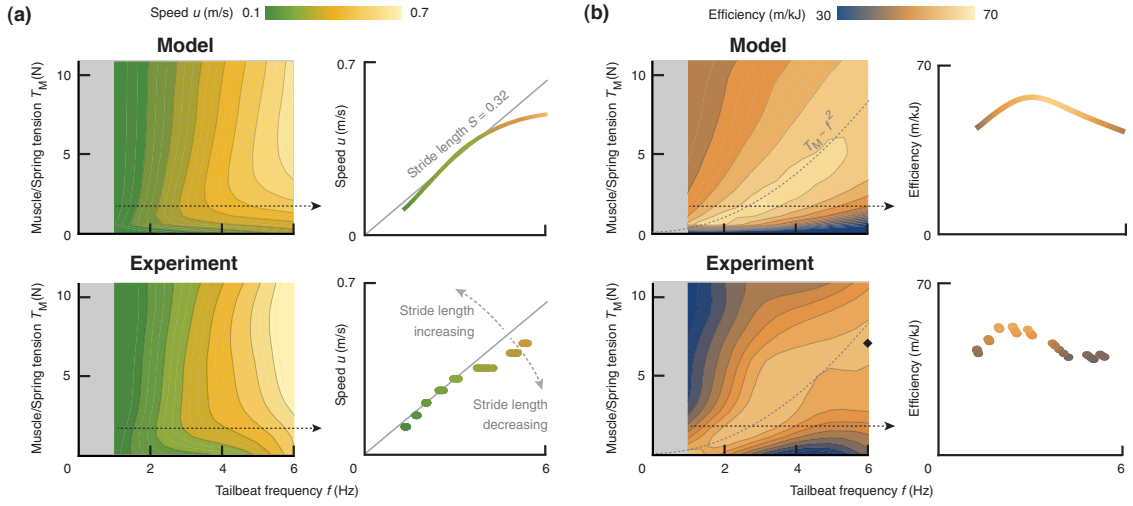


Figure 6.4: **Swimming speed and efficiency depend on muscle tension and tailbeat frequency.** (a) Speed is maximized when both frequency and muscle tension are high (contour plot interpolated from 841 points). Insert: if muscle tension stays constant ( $T_M = 1.9$  N), stride length declines at high frequencies. Model is matched to experiment with a 1-parameter fit for tail fin thrust coefficient ( $C_T = 2.4$ ; see section 6.2.1). (b) Efficiency is maximized when muscle tension is tuned for a specific frequency. Ideal tension at  $f = 6$  Hz: 8.7 N (Model),  $7 \pm 0.3$  N (Experiment,  $\blacklozenge$ ) Insert: if muscle tension stays constant, efficiency peaks at an intermediate frequency.

physics-driven strategy—one that could be used to explore biological variation and design new generations of robots.

### 6.3.3 Muscle/spring tension scale with swimming speed

To understand the patterns in efficiency that we observed (Figure. 6.4b), we considered what dimensionless ratios appear in our model. The amplitude of the tail fin is known to correlate with thrust [138]. In our model, the lateral position of the tail fin's trailing/distal edge ( $y_F$ ) behaves like a damped oscillator driven by the prescribed motions ( $\theta_T(t)$ ):

$$\ddot{y}_F = -\frac{16S^2}{9\pi^3} \left( \frac{\pi C_{\text{def}}}{2} + \tau^2 \right) y_F - \frac{4S}{3\pi} (1 + C_{\text{def}}) \dot{y}_F + F(\theta_T(t)) \quad (\text{Eq. 6.24})$$

where  $C_{\text{def}}$  is the Theodorsen wake deficiency function [105],  $F$  is a complex function

of the prescribed motions,  $S$  is stride length, and  $\tau$  is a ratio relating muscle tension and swimming speed ( $\tau \equiv \gamma\sqrt{T_M/(\bar{\ell}_F^3 u^2)}$ ; where  $\gamma$  is a constant and  $\bar{\ell}_F$  is tail fin length).

The “scaled muscle tension”  $\tau$  is related to the Cauchy number, which relates elastic forces to hydrodynamic forces [139]. The appearance of  $\tau$  in 6.24 highlights its importance in the dynamics of the tail fin. Adjusting  $\tau$  tunes the damped oscillator by changing the spring-like term (first term on the right hand side) and therefore the resonant frequency of the system. Fish have previously been modeled as driven oscillators [137], but here we offer a uniquely direct link between a controllable stiffness parameter ( $T_M$ ) and swimming performance (e.g. efficiency).

Our model predicts that stride length ( $S$ ) is a function of scaled muscle tension ( $\tau$ ) and peaks at an intermediate  $\tau$  value (Figure. 6.5a). Free-swimming data from our rig corroborate this prediction: the data cluster around a single  $S(\tau)$  curve with a local maximum near  $\tau = 2.5$  (Figure. 6.5a). At this optimal condition, the oscillator in Eq. 6.24 is at resonance (maximal tail amplitude), the stride length and efficiency are maximized, and the tail fin’s pitch angle lags its heave by  $\approx 90^\circ$  (Figure. 6.5b). These results are consistent with previous work: swimming at resonance maximizes stride length in—for example—robotic lampreys [140], and an optimal phase lag of  $90^\circ$  has been observed in hydrofoils with fully prescribed motions [141, 142].

According to our model, an efficient swimmer should tune its stiffness in order to stay at the optimal  $\tau$  value. To stay at one value of  $\tau$  ( $\gamma\sqrt{T_M/(\bar{\ell}_F^3 u^2)}$ ), the muscle/spring tension must increase with swimming speed squared ( $T_M \sim u^2$ ). Within this optimal condition, stride length is constant, so tension must also increase with frequency squared. This result explains why the ridge of peak efficiencies exists near a curve where  $T_M \sim f^2$  (Figure. 6.4b). In classic elasticity theory, resonant frequencies scale with the square root of stiffness [134]. In our model, the swimming speed and the resonant frequency are coupled, causing a speed-dependent optimal muscle/spring tension.

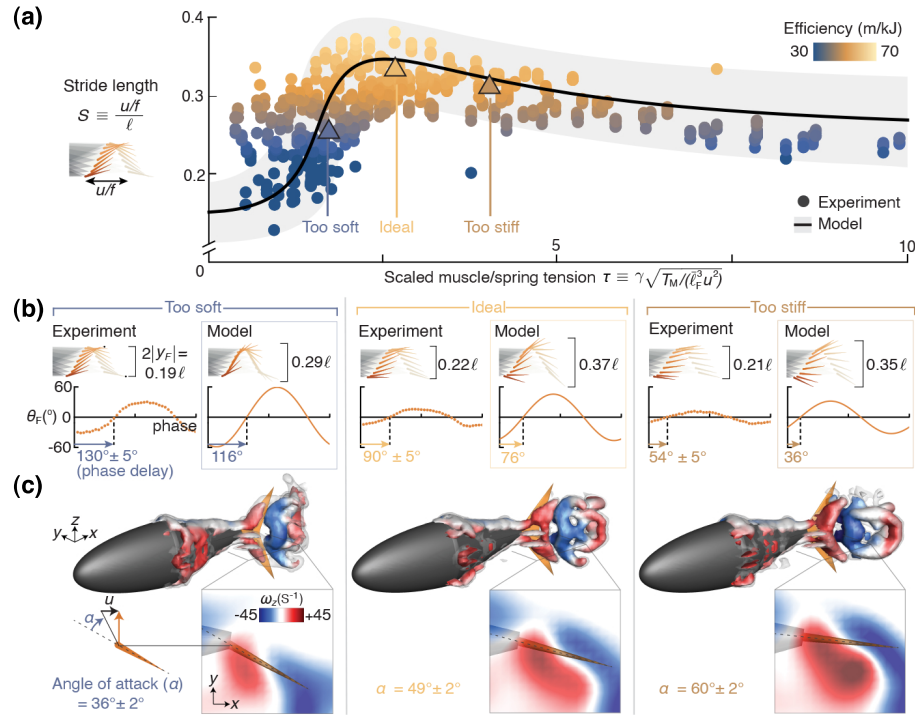


Figure 6.5: **Dimensional analysis and flow visualization reveal dynamics that govern optimal muscle/spring tension.** (a) Our model (black line) predicts that the scaled muscle tension ( $\tau$ ) determines the stride length ( $S$ ) and thus the efficiency (see section 6.2.2). Experimental data (colored circles) support these predictions. Model is matched to experiment with a 1-parameter fit for thrust coefficient ( $C_T = 2.4$ ; see section 6.2.1). Shaded gray band shows the sensitivity of the fit ( $C_T \pm 50\%$ ). (b) Three values of  $\tau$  highlight differences in kinematics: “too soft” ( $\tau = 1.88$ ), “ideal” ( $\tau = 2.68$ ), and “too stiff” ( $\tau = 3.96$ ) ( $f = 5$  Hz;  $T_M = 1.6, 5.3,$  and  $10.6$  N). Tail fin traces illustrate how the phase relationships maximize amplitude in the ideal case. (c) Increasing stiffness leads to higher angles of attack and a stronger, more detached Leading-Edge Vortex (LEV).  $Q$ -criterion isosurfaces are colored by dorsoventral vorticity ( $\omega_z$ ). Inserts: top view of one slice at the tail fin’s quarter span.

### 6.3.4 Nonlinear wakes at high stiffnesses

At high frequencies ( $f > \approx 4$  Hz), the model begins to overpredict the optimal muscle/spring tension (by  $24 \pm 5\%$  at 6 Hz, Figure. 6.4*b*). To understand why, we used Particle Image Velocimetry (PIV) to map the 3D flow around our robotic tail (28 stitched layers of cycle-averaged Stereo-PIV). Based on our efficiency measurements, we considered three cases of scaled muscle tension ( $\tau$ ): one below peak efficiency (“too soft”,  $\tau = 1.88$ ), one at peak efficiency (“ideal”,  $\tau = 2.68$ ), and one above peak efficiency (“too stiff”,  $\tau = 3.96$ ) (Figure. 6.5*a*).

As stiffness increases, more vorticity sheds into the wake of the robot’s tail fin. As the “muscle” pulls harder, the maximum angle of attack increases and the Leading Edge Vortex (LEV) becomes stronger and more detached from the tail fin (Figure. 6.5*c*). LEVs are prone to detachment at high angles of attack [143], like those present when the tail fin is over-stiffened. Attached LEVs can cause transient bursts of thrust [144], but detached LEVs can decrease efficiency [145, 146]. In the “too stiff” case, the W-shaped LEV detaches fully and morphs into a ring (Figure. 6.5*c*). These wake structures contain lateral kinetic energy that could otherwise have been spent on thrust. Such severe detachment was not present at low frequencies (Supp. Figure.B.6). Despite these wake effects, which slightly shift the optimal muscle/spring tension at high frequencies, the physics-driven tuning strategy ( $T_M \sim u^2$ ) still leads to near-optimal efficiencies (within 5% of global optimum at 6 Hz; Figure. 6.4*b*).

### 6.3.5 Real-time stiffness tuning in variable speed swimming missions.

To quantify the energetic advantages of stiffness tuning, we tested our platform’s ability to carry out multi-speed missions. We hung the platform from air bushings so it could move forward and backward (Figure. 6.3*h*), then had it maintain its position against the flow using

a PD controller to modulate tailbeat frequency. The flow was ramped up from 0.1 m/s to 0.65 m/s (0.3–2  $\ell/s$ ) over 15 min, simulating a 200-m multi-speed mission (Figure. 6.6a). To test the robustness of stiffness tuning, we also added a left-right axis of air bushings so that the platform would recoil laterally (Mission 2), programmed the platform to maneuver in a serpentine route (Mission 3), and increased its tailbeat amplitude by 33% (Mission 4). While swimming, the robotic tail tuned its muscle tension based on what was estimated to optimize efficiency (Figure. 6.4b). For comparison cases, we fully de-tensioned the spring ( $T_M$  effectively zero; “loose”), bolted the tail fin to the tail joint ( $T_M$  effectively infinite; “rigid”), and imposed a fixed spring tension chosen for its high efficiency ( $T_M = 5.5$  N; “medium”).

In all cases, swimming was more efficient when stiffness was tunable rather than fixed. In the “loose” and “rigid” cases, the platform could not even reach the high speeds later in the mission (Figure. 6.6b). The “medium” case led to high efficiency by the end of the mission, but low efficiency earlier in the mission (Figure. 6.6c). Only by tuning stiffness could the robot maintain an ideal  $\tau$  (Figure. 6.6a) and capture the benefits of flexibility over the full range of speeds. Tuning stiffness saved 16%, 41%, and 55% energy compared to the “medium”, “rigid”, and “loose” cases, respectively. Savings were comparable in the more complex missions (Figure. 6.6d). While our model assumes a uniform incoming flow and small angles, it captures the basic trends of Missions 3 and 4, where the platform maneuvered laterally and its tip-to-tip tail fin amplitude was  $36^\circ$ .

### 6.3.6 Tuning stiffness for high frequency fish and robots

Motivated by the energy savings we observed, we wondered how these savings scale with frequency and size according to our model. We considered fishes/robots with a maximum tailbeat frequency  $f_{\max}$  and a tail fin length  $\bar{l}_F$ . Then we calculated the average efficiency for frequencies ranging from 0 to  $f_{\max}$ —first assuming the best possible fixed stiffness, then assuming tunable stiffness. We capped muscle tension at 240 N based on the elastic

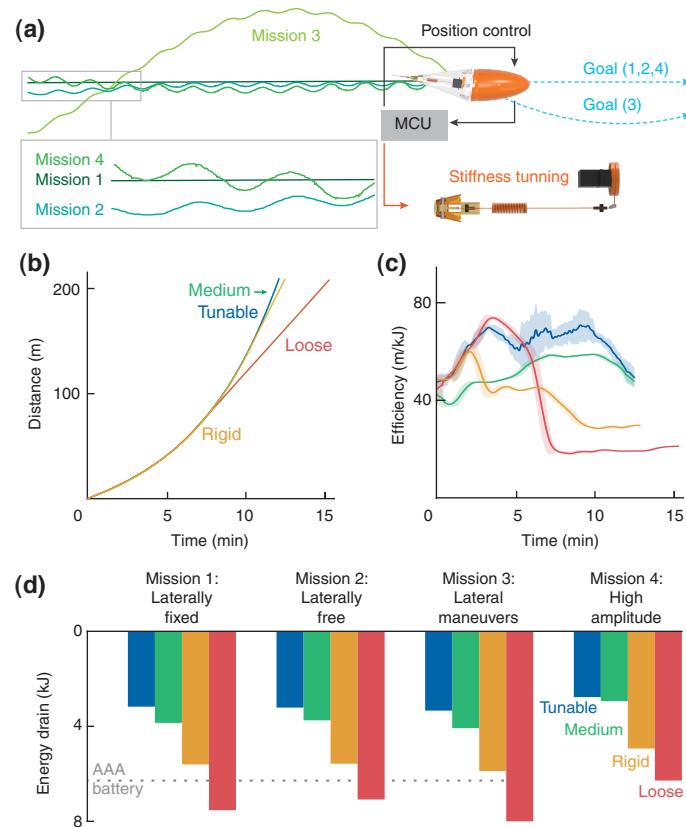


Figure 6.6: **Tuning stiffness saved energy across all missions.** (a) The platform used closed-loop control to stay on its goal path (on-board PD controller in a Micro Controller Unit (MCU)). (b) Tuning stiffness let the platform finish its mission faster. In the loose and rigid cases, speed plateaus during the mission. (c) Fixing stiffness led to inefficient mission segments. Only by tuning stiffness could the robotic tail maximize efficiency throughout the mission. (d) Tuning stiffness led to less energy drain in all four missions. Storage capacity of a AAA battery ( $\approx 6$  kJ) shown for reference.

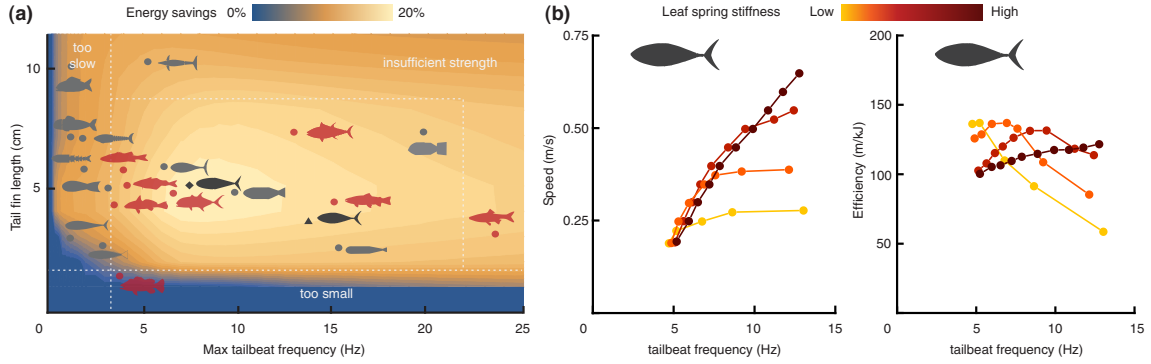


Figure 6.7: **Tunable stiffness is most beneficial for high frequency fish and robots.** (a) Our model predicts that the benefits of tuning stiffness increase with frequency range, so long as muscles are strong enough to reach the optimal stiffnesses. Existing fish-like robots (●) are clustered at low servo-limited frequencies. In high-frequency fish (●), platforms like ours (◆), or robots like the Tunabot (▲), tuning stiffness improves efficiency by closer to 20%. Avatar descriptions in Table.B.2 (b) With fixed stiffness, the Tunabot shows nonlinear speed-frequency and efficiency-frequency dependences that are similar to those of our platform (Figure. 6.4a-b).

range of tuna tendons [3]. We found that for small, slow-moving tails, tuning stiffness offers only marginal benefits due to the narrow range of optimal tensions (Figure. 6.7a). As tail fin size and frequency increase, fish have more to gain from tuning stiffness (energy savings rise to 20% as  $f_{\max}$  rises to 10 Hz). Beyond some critical size and frequency, savings taper off as muscle strength becomes insufficient for creating the high tensions that optimize efficiency.

To corroborate our predictions of energy savings, we added fixed stiffness tail fins to the autonomous Tunabot [4] and tested it in our water channel. Despite measuring the efficiency differently (via the electrical power going to the Tunabot), we found similar speed and efficiency trends to those observed on our platform (Figure. 6.4a-b; Figure. 6.7b), and the estimated energy savings of tuning stiffness were comparable to those predicted by our model ( $17 \pm 5\%$  vs. 16%).

## 6.4 Discussion

Our model and experimental data corroborate the same prediction: if stiffness does not increase with swimming speed squared, stride length and efficiency decrease. While our robotic tests cannot prove whether fish use a particular tuning strategy, they offer a parsimonious explanation for trends observed in nature. In longnose gar, artificially reducing stiffness caused fish to lower their tail-beat frequency [73]. In pumpkinseed sunfish, reducing stiffness led to lower swimming speeds at the same tail-beat frequency [147]. Only by tuning stiffness could our platform and the Tunabot maintain a linear frequency-speed relation and a plateaued frequency-efficiency relation using a single gait (Figure. 6.4, 6.7*b*)—features that are commonplace across several fish taxa [39, 148, 131, 149, 150, 151].

Many aquatic vertebrates have analogous caudal tendon arrangements as tuna [135]. Even sharks, distant relatives of tuna, are thought to stiffen their tail at high frequencies using their radialis muscle [152]. Tuning stiffness may therefore be a widespread constraint for aquatic animals, who produce similar flexion ratios across a wide range of scales and speeds (e.g. clownfish up to humpback whales [153]). Tuning is probably less important for small, low-frequency fins, where even a fixed stiffness can be near-optimal according to our model (Figure. 6.7*a*). Very large fins may also have limited use for tuning if the optimal stiffnesses are unattainable based on available muscle strength (Figure. 6.7*a*). While our savings estimates were based on tuna, this size constraint is likely more general, because the required tensions outpace strength as size scales up (modelled optimal tension scales with  $\ell^3$ ; muscle force scales with  $\ell^2$  [154]).

While our stiffness tuning model was inspired by tail fins, it could offer design insights to other fins or fluid-embedded devices. If the tendon were modeled on the side of the propulsor, rather than the leading edge, the model could potentially approximate the pectoral fins of ray/skate-inspired robots, where the relative importance of active and

passive control is an open question [155, 2]. Cantilever-based energy harvesters are also known to benefit from tunable stiffness, especially in dynamic flow environments [156, 157]. Because our model is derived from thin airfoil theory, it may be particularly relevant to harvesters that harness the aeroelastic vibrations of passive wings [158] or fluttering flags [159]. In general, models that link stiffness tuning with performance can be used to produce known optimal kinematics [64, 65, 66, 67, 68] with existing stiffness tuning mechanisms [82, 80, 78, 81, 3, 79].

Regardless of how well our results apply to other systems, their implications for tuna-inspired robots are clear: tuning flexibility is critical for efficient, multi-speed operation. The latest tuna-inspired robots have huge frequency ranges: 0–15 Hz for the Tunabot [4], 0–20 Hz for the iSplash [69]. These vehicles may need to cruise for miles from a coastal outpost or ship, then slow down to navigate a coral reef or a narrow corridor. For these multi-frequency, multi-speed swimmers to maintain high efficiency, tuning flexibility may be as important as flexibility itself.

# Chapter 7

## Concluding Remarks and Future Work

### 7.1 Boundary Interactions

When swimming near the ground, pitching foils generate asymmetric lift force and change signs and amplitudes with the distance from the ground. Therefore, freely swimming pitching foils converge to stable equilibrium altitudes, and these equilibrium altitudes are insensitive to initial altitude. Furthermore, the equilibria are dependent on swimming kinematics: equilibrium altitudes increase with increasing Strouhal number or decreasing reduced frequency. When very close to the ground, the asymmetric lift drops from positive to negative within a small distance, leading to another unstable equilibrium altitude. Unlike the stable equilibria, foils are hard to stable at these unstable equilibria.

Based on the results of finite aspect ratio foils, we found that the unsteady ground effect is weaker for lower aspect ratio hydrofoils. Lower aspect ratio foil produces less thrust enhancement and smaller equilibrium altitudes (Figure. 3.6). The equilibrium for the  $\mathcal{R} = 1$  foil was not even detectable at low enough Strouhal numbers. These results are consistent with the near-ground wakes we observed, where the ground had a smaller effect on the wake of the  $\mathcal{R} = 1$  foil.

When considering the asymmetric lift and thrust boost together, we found that low-

aspect-ratio swimmers may be able to leverage ground effects more easily. High-aspect-ratio foils experience a considerable thrust boost near the ground (Fig. 3.6*a,b*; 3.10*a*). However, the thrust boost at the stable equilibrium point was negligible (Figure. 3.6*b,f*; 3.10*a*), so to access higher thrust, high-aspect-ratio foils would need to actively offset lift asymmetries—perhaps using asymmetric kinematics or negative buoyancy. Active control would be especially necessary to access the high-thrust region very close to the wall. As  $d/c$  drops below  $\approx 0.5$ , thrust can nearly double, but lift asymmetries are high, and the nearby unstable equilibrium could risk a sudden surge toward the ground. In contrast, near-ground low-aspect-ratio hydrofoils see relatively smaller thrust and efficiency boosts, but also much weaker lift asymmetries, allowing freer movement into near-ground regions that maximize performance (Figure. 3.10).

Because aspect ratio has such pronounced effects on near-ground performance, it is apparently a key design parameter for near-boundary swimmers and fliers. Fish that evolve to live near the substrate show “highly predictable changes in body form”, including widened or elongated bodies [160]. The changes are typically linked with feeding ecology [161, 162]; our results suggest that body-ground interactions could also influence an animal’s aspect ratio. While kinematics and flexibility are also key pelagic-benthic differentiators (e.g. undulatory vs. oscillatory kinematics in rays and skates; Rosenberger, 2001), we show that aspect ratio is at least one of the critical factors affecting near-ground swimmers.

By comparing experiments and potential flow simulations, we found that unsteady ground effects are primarily inviscid phenomena over the conditions we tested. For  $\mathcal{R} \geq 1.3$ , our results suggest that viscosity plays only a minor role in determining equilibrium altitude, which extends previous findings on 2D hydrofoils [83]. It is worth noting that in potential flow theory, a hydrofoil at distance  $d$  from a boundary is identical to a hydrofoil at distance  $2d$  from a second hydrofoil pitching  $180^\circ$  out-of-phase with the first. Thrust, for example, is known to scale similarly for hydrofoils that are near a boundary and hydrofoils that are side-by-side and out-of-phase [58]. The inviscid nature of our results, therefore,

suggests that stable and unstable equilibria may also exist for side-by-side swimmers. Indeed, hydrodynamic effects are known to play a key role in the collective behavior of fish [163].

## 7.2 Fish-inspired Maneuvers

When accelerating in the streamwise direction, we found that at the same Strouhal number, a frequency-driven maneuver six times as much acceleration as an amplitude-driven maneuver. This result could help explain why natural swimmers prefer to modulate their tail-beat frequency to adjust swimming speed [9]. Increasing frequency also led to less lateral recoil, which suggests greater lateral stability while accelerating. Because our hydrofoil has a fixed average yaw angle, our rig cannot confirm lateral instabilities. Still, real fish that modulate tail-beat amplitude during accelerations do show greater lateral recoil [37]. While our results suggest that frequency modulation is a better acceleration strategy, amplitude modulation has benefits. First, it could further increase the Strouhal number in cases where the frequency was already maximized, leading to even faster accelerations.

When maneuvering in the lateral direction, adding pitch bias (spatial asymmetry) created smooth, quasi-steady lateral maneuvers. The fact that lateral displacement scaled linearly with pitch bias suggests that those lateral maneuvers were driven by the quasi-steady lift term of thin airfoil theory [105]. Modulating stroke speed ratio (temporal asymmetry) created lateral maneuvers that were more complex: the lateral asymmetry caused streamwise acceleration due to the higher mid-cycle lateral tail speeds. It introduced temporal asymmetry led to a paired vortex wake and a burst of asymmetric yaw torque.

While we have focused on “maneuvers”, asymmetries are also relevant to slight corrections during steady swimming. Fish tend to be passively unstable in both yaw [164] and roll [165], so maintaining a stable attitude requires asymmetric kinematics even during normal swimming. Our results, therefore, offer a framework for streamwise/lateral corrections

more generally. Whether a fish/robot intends to change trajectory, or maintain the same trajectory, they can use a combination of streamwise and lateral modulations to achieve their goal.

### 7.3 Multi-fin Interactions

Sharp, elongated dorsal/anal fins shed long, thin vortices that induce lateral crossflow and stabilize the caudal fin's Leading Edge Vortex (LEV). This mechanism places dorsal-caudal fin interactions into a classical family of flows where crossflows promote flow attachment on a lifting surface. At low Reynolds numbers, for example, laminar boundary layers are thinner, more stable, and less prone to detachment when there is wall suction [166, 167]. The flow in our case is unsteady, and the magnitude of crossflow is much higher ( $\approx 0.5u$  compared to  $< 0.01u$  in [167]), but this general principle is empirically known to extend to high Reynolds numbers as well. For instance, active blown flaps and passive slats promote crossflows that stabilize the flow over wings during fighter jet maneuvers [168]. Leading-edge slats can be modeled as a simple vortex placed at the slat, inducing a crossflow and promoting flow attachment on the main wing [169]. We propose that elongated dorsal/anal fin geometries may be especially similar to strakes and Leading Edge Root eXtensions, where thin fins on the fuselage create long, thin strake vortices that reduce the angle of attack and promote spanwise flow (Figure 5.5*c,d*).

Dorsal-caudal fin interactions also offer new insights into the morphologies of fish and fish-inspired vehicles. By inhibiting flow separation on the caudal fin, the dorsal/anal fins increase swimming speed and economy, even if the laterally-projected area is unchanged. The fins need not be razor-thin, because, beyond a critical sharpness, the fins draw more power while having no noticeable effect on the flow along the caudal fin. Flow separation could also be inhibited by reducing tailbeat amplitude or frequency but at the cost of reduced thrust. Not only does the mechanism observed here work at high thrust, it is rel-

atively insensitive to phase lag. The Reynolds and Strouhal number ranges of our study (41000-98400 and 0.62-0.76) represent slow swimming compared to typical tuna cruise speeds, so the mechanism we observed may be most relevant at low speeds. However, given that the mechanism became more pronounced at higher Reynolds numbers, it may persist or even be stronger at higher speeds, where the fast-oscillating flow on the caudal fin is more prone to detachment. Either way, the mechanism provides a phase-insensitive, passive solution for improving the flow characteristics over oscillating propulsors, thereby offering design strategies for multi-fin, bio-inspired vehicles.

## **7.4 Real-time Adjustable Flexibility**

As for the stiffness effects on swimming performance, our model and experimental data corroborate the same prediction: if stiffness does not increase with swimming speed squared, stride length and efficiency decrease. While our robotic tests cannot prove whether fish use a particular tuning strategy, they offer a parsimonious explanation for trends observed in nature. In longnose gar, artificially reducing stiffness caused fish to lower their tail-beat frequency [73]. In pumpkinseed sunfish, reducing stiffness led to lower swimming speeds at the same tail-beat frequency [147]. Only by tuning stiffness could our platform and the Tunabot maintain a linear frequency-speed relation and a plateaued frequency-efficiency relation using a single gait (Figure. 6.4, 6.7*b*)—features that are commonplace across several fish taxa [39, 148, 131, 149, 150, 151].

Many aquatic vertebrates have analogous caudal tendon arrangements as tuna [135]. Even sharks, distant relatives of tuna, are thought to stiffen their tails at high frequencies using their radialis muscle [152]. Tuning stiffness may therefore be a widespread constraint for aquatic animals, who produce similar flexion ratios across a wide range of scales and speeds (e.g. clownfish up to humpback whales [153]). Tuning is probably less important for small, low-frequency fins, where even a fixed stiffness can be near-optimal according to

our model (Figure. 6.7a). Very large fins may also have limited use for tuning if the optimal stiffnesses are unattainable based on available muscle strength (Figure. 6.7a). While our savings estimates were based on tuna, this size constraint is likely more general because the required tensions outpace strength as size scales up (modelled optimal tension scales with  $\ell^3$ ; muscle force scales with  $\ell^2$  [154]).

Regardless of how well our results apply to other systems, their implications for tuna-inspired robots are clear: tuning flexibility is critical for efficient, multi-speed operation. The latest tuna-inspired robots have huge frequency ranges: 0–15 Hz for the Tunabot [4], 0–20 Hz for the iSplash [69]. These vehicles may need to cruise for miles from a coastal outpost or ship, then slow down to navigate a coral reef or a narrow corridor. For these multi-frequency, multi-speed swimmers to maintain high efficiency, tuning flexibility may be as important as flexibility itself.

## 7.5 Future Work

In the chapter 3 , we explored the unsteady ground effect with hydrofoils pitching symmetrically. It could be interesting to further investigate the unsteady ground effect with more complex oscillation motions. Natural swimmers, like rays, flap their wings asymmetrically with large amplitude when near the ground [29]. It is not clear why rays have such asymmetric motion, presumably intend to manipulate the unsteady ground effect or just to avoid collision with the ground. Several parameters could be introduced to generate more complex fish-like oscillation motions, like pitch bias, stroke velocity ratio (see chapter 4), or heaving motion. Besides the oscillation motion, the weight of the swimmer could affect the stable and unstable equilibrium altitudes. Controlling the weight of the swimmer could shift the lift generation curve (see figure 3.10) up and down, thus adjust the altitude of stable and unstable equilibrias. For a free-swimming swimmer, the weight of the swimmer could affect the magnitude of lateral recoil, therefore lead to a different effective tail peak

to peak amplitude. This phenomena was observed in the test process of studies in the chapter 3, but more comprehensive tests are required to understand the underlying mechanism. Because of the inviscid nature of unsteady ground effect, our results indicated the stable and unstable equilibrium altitudes might also exist for side-by-side out of phase swimmers, and this has been observed by two-dimensional experimental and simulation studies [170, 171]. However, it is not clear whether this interaction does exist in robot and real fishes schooling. Wake interaction might mainly exist on robot/fishes high aspect ratio tail fin ( $\mathcal{R} \geq 1$ ), or become more complicated due to their ultra-low aspect ratio oscillating body ( $\mathcal{R} \leq 0.5$ ).

In the chapter 4, we proposed a maneuver equation and investigated fish-inspired maneuver with a free to move pitching foil. Based on current results, future work could focus on taking more data to propose a scaling law on maneuver motion that could apply to maneuver control of the fish-inspired robots. Due to the design limit of the pitching actuator, our rig does not have a passive degree of freedom on the yaw axis of the swimmer. Therefore our rig cannot produce passive yaw turning like a real fish. This discrepancy on passive yaw motion might be negligible on small maneuver motion, like high-speed lateral shifting, but cannot capture the feature of low-speed sharp maneuvers, like "C-start" or rapid-turning [47, 104, 107]. To further evaluate the difference between a spatial and temporal asymmetric motion for rapid turning, it is necessary to compare those two motions in a free-swimming autonomous robot. Moreover, because the current study cannot capture the body curvature of the fish due to the rigid, single degree of freedom foil design, future work with a multi-joint fish-inspired tail could be helpful to better understand fish-like maneuver.

As for the three-dimensional feature of the fish-inspired platform, the chapter 5 offered a practical design to improve swimming performance with multi-fin interaction. This elongated sharp dorsal fin design was tested on the two degrees of freedom reduced-order platform, therefore it is not clear whether a similar mechanism still exists on more complex

fish robots. For example, a multi-joint tail platform will lead to a phase difference between the front and end edge of the dorsal fin, thus might generate a different stroke vortex. Moreover, for some of the high-frequency fishes, like tuna, which have independent fin arrays—finlets instead of a one-piece elongate dorsal fin. Function of these passive pitching finlets were investigated by a recent study [172] with low  $Re$  simulation, but it is not clear how this unique design could affect the performance in a more realistic condition, especially at high frequency and high speed.

When exploring the adjustable stiffness with the reduced-order platform in the chapter 6, we mainly considered the free-swimming condition. Therefore the stiffness tuning law was proposed for steady free swimming. Although the stiffness tuning law was proved robust enough to handle more complex missions, like the side-by-side maneuver, further studies are required to take full advantage of adjustable stiffness for more complex motions. When accelerating in streamwise direction with the reduced-order platform, how to tune the stiffness with variable frequency and pitch amplitude is required to gain maximum acceleration performance. Besides tuning stiffness across pitching cycles, the tail stiffness could be tuned within one pitching cycle. For example, when performing lateral maneuver with temporal asymmetry motion, one could use higher stiffness for fast stroke and lower stiffness for slow stroke to maximize the asymmetric lateral force. Since our stiffness tuning strategy was developed on experiment and modeling of the two-joint reduced-order platform, it might not apply to more complicated robots/swimmers. Therefore, future work could also focus on developing a universal stiffness tuning model and more advanced controllable stiffness platforms. More importantly, future work should also focus on developing a stiffness tuning mechanism. To successfully deploy the stiffness tuning technique on marine applications, how to effectively tune the stiffness with minimum energy cost may be as important as maintaining high swimming performance with tunable stiffness itself.

# Bibliography

- [1] M. S. Triantafyllou and G. S. Triantafyllou, “An efficient swimming machine,” *Scientific american*, vol. 272, no. 3, pp. 64–70, 1995.
- [2] F. Fish, C. Schreiber, K. Moored, G. Liu, H. Dong, and H. Bart-Smith, “Hydrodynamic Performance of Aquatic Flapping: Efficiency of Underwater Flight in the Manta,” *Aerospace*, vol. 3, no. 3, p. 20, 2016.
- [3] J. Yu, Z. Su, Z. Wu, and M. Tan, “Development of a Fast-Swimming Dolphin Robot Capable of Leaping,” *IEEE/ASME Transactions on Mechatronics*, vol. 21, no. 5, pp. 2307–2316, 2016.
- [4] J. Zhu, C. White, D. K. Wainwright, V. Di Santo, G. V. Lauder, and H. Bart-Smith, “Tuna robotics: A high-frequency experimental platform exploring the performance space of swimming fishes,” *Science Robotics*, vol. 4, no. 34, 2019.
- [5] J. M. ANDERSON, K. STREITLIEN, D. S. BARRETT, and M. S. TRIANTAFYLLOU, “Oscillating foils of high propulsive efficiency,” *Journal of Fluid Mechanics*, vol. 360, S0022112097008392, 1998.
- [6] T. Schnipper, A. Andersen, and T. Bohr, “Vortex wakes of a flapping foil,” *Journal of Fluid Mechanics*, vol. 633, pp. 411–423, 2009.
- [7] D. Floryan, T. Van Buren, C. W. Rowley, and A. J. Smits, “Scaling the propulsive performance of heaving and pitching foils,” *Journal of Fluid Mechanics*, vol. 822, pp. 386–397, 2017. arXiv: arXiv:1704.07478v1.
- [8] R. Blake, *Fish locomotion*. 1983.
- [9] O. Akanyeti, J. Putney, Y. R. Yanagitsuru, G. V. Lauder, W. J. Stewart, and J. C. Liao, “Accelerating fishes increase propulsive efficiency by modulating vortex ring geometry,” *Proceedings of the National Academy of Sciences of the United States of America*, vol. 114, no. 52, pp. 13 828–13 833, 2017.
- [10] E. D. Tytell, “Median fin function in bluegill sunfish *Lepomis macrochirus*: stream-wise vortex structure during steady swimming,” *Journal of Experimental Biology*, vol. 209, no. 8, pp. 1516–1534, 2006.
- [11] J. C. Nauen and G. V. Lauder, “Locomotion in scombrid fishes: Morphology and kinematics of the finlets of the chub mackerel *scomber japonicus*,” *Journal of Experimental Biology*, vol. 203, no. 15, pp. 2247–2259, 2000.
- [12] J. C. Liao, *A review of fish swimming mechanics and behaviour in altered flows*, 2007.

- [13] E. D. Tytell, C.-Y. Hsu, T. L. Williams, A. H. Cohen, and L. J. Fauci, “Interactions between internal forces, body stiffness, and fluid environment in a neuromechanical model of lamprey swimming,” *Proceedings of the National Academy of Sciences of the United States of America*, vol. 107, no. 46, pp. 19 832–7, 2010.
- [14] R. E. Shadwick and D. A. Syme, “Thunniform swimming: Muscle dynamics and mechanical power production of aerobic fibres in yellowfin tuna (*Thunnus albacares*),” *Journal of Experimental Biology*, vol. 211, no. 10, pp. 1603–1611, 2008.
- [15] D. K. Wainwright and G. V. Lauder, “Tunas as a high-performance fish platform for inspiring the next generation of autonomous underwater vehicles,” *Bioinspiration & Biomimetics*, vol. 15, no. 3, p. 35 007, 2020.
- [16] R. V. Baudinette and K Schmidt-Nielsen, “Energy cost of gliding flight in herring gulls,” *Nature*, vol. 248, no. 5443, p. 83, 1974.
- [17] F. R. Hainsworth, “Induced drag savings from ground effect and formation flight in brown pelicans,” *Journal of experimental biology*, vol. 135, no. 1, pp. 431–444, 1988.
- [18] R. W. Blake, “The energetics of hovering in the mandarin fish (*Synchropus picturatus*),” *J. Exp. Biol.*, vol. 82, pp. 25–33, 1979.
- [19] P. W. Webb, “The effect of solid and porous channel walls on steady swimming of steelhead trout *Oncorhynchus mykiss*,” *Journal of Experimental Biology*, vol. 178, no. 1, pp. 97–108, 1993.
- [20] D. B. Quinn, G. V. Lauder, and A. J. Smits, “Flexible propulsors in ground effect,” *Bioinspiration and Biomimetics*, vol. 9, no. 3, p. 8, 2014.
- [21] A. Mivehchi, J. Dahl, and S. Licht, “Heaving and pitching oscillating foil propulsion in ground effect,” *Journal of Fluids and Structures*, vol. 63, pp. 174–187, 2016.
- [22] D. B. Quinn, K. W. Moored, P. A. Dewey, and A. J. Smits, “Unsteady propulsion near a solid boundary,” *J. Fluid Mech*, vol. 742, pp. 152–170, 2014.
- [23] R. Fernández-Prats, V. Raspa, B. Thiria, F. Huera-Huarte, and R. Godoy-Diana, “Large-amplitude undulatory swimming near a wall,” *Bioinspiration and Biomimetics*, vol. 10, no. 1, p. 16 003, 2015. arXiv: 1412.2932.
- [24] S. G. Park, B. Kim, and H. J. Sunga, “Hydrodynamics of a self-propelled flexible fin near the ground,” *Physics of Fluids*, vol. 29, no. 5, p. 051 902, 2017.
- [25] C. Zhang, H. Huang, and X. Y. Lu, “Free locomotion of a flexible plate near the ground,” *Physics of Fluids*, vol. 29, no. 4, p. 041 903, 2017.
- [26] L. Dai, G. He, and X. Zhang, “Self-propelled swimming of a flexible plunging foil near a solid wall,” *Bioinspiration and Biomimetics*, vol. 11, no. 4, p. 046 005, 2016.
- [27] C. Tang, H. Huang, P. Gao, and X.-Y. Lu, “Self-propulsion of a flapping flexible plate near the ground,” *PHYSICAL REVIEW E*, vol. 94, p. 33 113, 2016.
- [28] D. B. Quinn, K. W. Moored, P. A. Dewey, and A. J. Smits, “Unsteady propulsion near a solid boundary,” *Journal of Fluid Mechanics*, vol. 742, pp. 152–170, 2014.

- [29] L. J. Rosenberger, “Pectoral fin locomotion in batoid fishes,” Tech. Rep., 2001.
- [30] W. J. Cooper, C. B. Carter, A. J. Conith, A. N. Rice, and M. W. Westneat, “The evolution of jaw protrusion mechanics is tightly coupled to benthic-pelagic divergence in damselfishes (Pomacentridae),” *Journal of Experimental Biology*, vol. 220, no. 4, pp. 652–666, 2017.
- [31] P. R. Bandyopadhyay, “Maneuvering hydrodynamics of fish and small underwater vehicles,” *Integrative and Comparative Biology*, vol. 42, no. 1, pp. 102–117, 2002.
- [32] F. E. Fish, “Advantages of aquatic animals as models for bio-inspired drones over present AUV technology,” *Bioinspiration & Biomimetics*, vol. 15, no. 2, p. 25 001, 2020.
- [33] —, “Performance constraints on the maneuverability of flexible and rigid biological systems,” in *International Symposium on Unmanned Untethered Submersible Technology*, 1999, pp. 394–406.
- [34] F. E. Fish and G. V. Lauder, “Control surfaces of aquatic vertebrates: active and passive design and function,” *Journal of Experimental Biology*, vol. 220, no. 23, pp. 4351–4363, 2017.
- [35] D. Weihs, “The mechanism of rapid starting of slender fish,” *Biorheology*, vol. 10, no. 3, pp. 343–350, 1973.
- [36] D. Weihs, “A hydrodynamical analysis of fish turning manoeuvres,” *Proceedings of the Royal Society of London. Series B. Biological Sciences*, vol. 182, no. 1066, pp. 59–72, 1972.
- [37] T. N. Wise, M. A. Schwalbe, and E. D. Tytell, “Hydrodynamics of linear acceleration in bluegill sunfish, *Lepomis macrochirus*,” *Journal of Experimental Biology*, vol. 221, no. 23, 2018.
- [38] K. T. Du Clos, J. O. Dabiri, J. H. Costello, S. P. Colin, J. R. Morgan, S. M. Fogerson, and B. J. Gemmell, “Thrust generation during steady swimming and acceleration from rest in anguilliform swimmers,” *Journal of Experimental Biology*, vol. 222, no. 22, 2019.
- [39] R. Bainbridge, “The speed of swimming of fish as related to size and to the frequency and amplitude of the tail beat,” *Journal of experimental biology*, vol. 35, no. 1, pp. 109–133, 1958.
- [40] J. C. Liao, D. N. Beal, G. V. Lauder, and M. S. Triantafyllou, “The Kármán gait: Novel body kinematics of rainbow trout swimming in a vortex street,” *Journal of Experimental Biology*, vol. 206, no. 6, pp. 1059–1073, 2003.
- [41] P. W. Webb, “Kinematics of plaice, pleuronectes platessa, and cod, *gadus morhua*, swimming near the bottom,” *Journal of Experimental Biology*, vol. 205, no. 14, pp. 2125–2134, 2002.
- [42] Z. Wu, J. Yu, M. Tan, and J. Zhang, “Kinematic comparison of forward and backward swimming and maneuvering in a self-propelled sub-carangiform robotic fish,” *Journal of Bionic Engineering*, vol. 11, no. 2, pp. 199–212, 2014.

- [43] J. M. Anderson and N. K. Chhabra, “Maneuvering and stability performance of a robotic tuna,” in *Integrative and Comparative Biology*, vol. 42, Society for Integrative and Comparative Biology, 2002, pp. 118–126.
- [44] J. Conte, Y. Modarres-Sadeghi, M. N. Watts, F. S. Hover, and M. S. Triantafyllou, “A fast-starting mechanical fish that accelerates at 40 m s<sup>-2</sup>,” *Bioinspiration and Biomimetics*, vol. 5, no. 3, 2010.
- [45] T. Currier and Y. Modarres-Sadeghi, “An experimental model with passively variable stiffness to investigate the effect of body stiffness on the fish fast-start maneuver,” *Experiments in Fluids*, vol. 60, no. 9, pp. 147–148, 2019.
- [46] L. Wen, Z. Ren, V. Di Santo, K. Hu, T. Yuan, T. Wang, and G. V. Lauder, “Understanding fish linear acceleration using an undulatory biorobotic model with soft fluidic elastomer actuated morphing median fins,” *Soft Robotics*, vol. 5, no. 4, pp. 375–388, 2018.
- [47] W. C. Witt, L. Wen, and G. V. Lauder, “Hydrodynamics of C-Start Escape Responses of Fish as Studied with Simple Physical Models,” *Integrative and Comparative Biology*, vol. 55, no. 4, pp. 728–739, 2015.
- [48] B. A. Free and D. Paley, “Model-based observer and feedback control design for a rigid Joukowski foil in a Kármán vortex street,” *Bioinspiration & Biomimetics*, 2018.
- [49] D. A. Read, F. S. Hover, and M. S. Triantafyllou, “Forces on oscillating foils for propulsion and maneuvering,” *Journal of Fluids and Structures*, vol. 17, no. 1, pp. 163–183, 2003.
- [50] G. V. Lauder and P. G. Madden, “Advances in comparative physiology from high-speed imaging of animal and fluid motion,” *Annu. Rev. Physiol.*, vol. 70, pp. 143–163, 2008.
- [51] F. E. Fish, K. T. Goetz, D. J. Rugh, and L. V. Brattström, “Hydrodynamic patterns associated with echelon formation swimming by feeding bowhead whales (*balaena mysticetus*),” *Marine Mammal Science*, vol. 29, no. 4, E498–E507, 2013.
- [52] M Saadat, F. E. Fish, A. Domel, V Di Santo, G. Lauder, and H Haj-Hariri, “On the rules for aquatic locomotion,” *Physical Review Fluids*, vol. 2, no. 8, p. 083 102, 2017.
- [53] E. G. Drucker and G. V. Lauder, “Locomotor function of the dorsal fin in teleost fishes: Experimental analysis of wake forces in sunfish,” *Journal of Experimental Biology*, vol. 204, no. 17, pp. 2943–2958, 2001.
- [54] E. Standen and G. V. Lauder, “Hydrodynamic function of dorsal and anal fins in brook trout (*salvelinus fontinalis*),” *Journal of Experimental Biology*, vol. 210, no. 2, pp. 325–339, 2007.
- [55] E. D. Tytell, “Median fin function in bluegill sunfish *lepomis macrochirus*: Stream-wise vortex structure during steady swimming,” *Journal of Experimental Biology*, vol. 209, no. 8, pp. 1516–1534, 2006.

- [56] I. Akhtar, R. Mittal, G. V. Lauder, and E. Drucker, “Hydrodynamics of a biologically inspired tandem flapping foil configuration,” *Theoretical and Computational Fluid Dynamics*, vol. 21, no. 3, pp. 155–170, 2007.
- [57] B. M. Boschitsch, P. A. Dewey, and A. J. Smits, “Propulsive performance of unsteady tandem hydrofoils in an in-line configuration,” *Physics of Fluids*, vol. 26, no. 5, p. 051 901, 2014.
- [58] P. A. Dewey, D. B. Quinn, B. M. Boschitsch, and A. J. Smits, “Propulsive performance of unsteady tandem hydrofoils in a side-by-side configuration,” *Physics of Fluids*, vol. 26, no. 4, p. 041 903, 2014.
- [59] G. Liu, Y. Ren, H. Dong, O. Akanyeti, J. C. Liao, and G. V. Lauder, “Computational analysis of vortex dynamics and performance enhancement due to body–fin and fin–fin interactions in fish-like locomotion,” *Journal of Fluid Mechanics*, vol. 829, pp. 65–88, 2017.
- [60] B. B. Collette, C. E. Nauen, *et al.*, *FAO species catalogue. Volume 2. Scombrids of the world. An annotated and illustrated catalogue of tunas, mackerels, bonitos and related species known to date.* 125. 1983.
- [61] Q. Zhu, M. Wolfgang, D. Yue, and M. Triantafyllou, “Three-dimensional flow structures and vorticity control in fish-like swimming,” *Journal of Fluid Mechanics*, vol. 468, pp. 1–28, 2002.
- [62] G. V. Lauder, P. G. A. Madden, J. L. Tangorra, E. Anderson, and T. V. Baker, “Bioinspiration from fish for smart material design and function,” *Smart Materials and Structures*, vol. 20, no. 9, p. 94 014, 2011.
- [63] J. H. Long, “Muscles, Elastic Energy, and the Dynamics of Body Stiffness in Swimming Eels,” *American Zoologist*, vol. 38, no. 4, pp. 771–792, 1998.
- [64] C. J. Esposito, J. L. Tangorra, B. E. Flammang, and G. V. Lauder, “A robotic fish caudal fin: effects of stiffness and motor program on locomotor performance,” *Journal of Experimental Biology*, vol. 215, no. 1, pp. 56–67, 2012.
- [65] S. Heathcote and I. Gursul, “Flexible Flapping Airfoil Propulsion at Low Reynolds Numbers,” *AIAA Journal*, vol. 45, no. 5, pp. 1066–1079, 2007.
- [66] J. Katz and D. Weihs, “Hydrodynamic propulsion by large amplitude oscillation of an airfoil with chordwise flexibility,” *Journal of Fluid Mechanics*, vol. 88, no. 03, p. 485, 1978.
- [67] J. L. Tangorra, G. V. Lauder, I. W. Hunter, R. Mittal, P. G. A. Madden, and M. Bozkurtas, “The effect of fin ray flexural rigidity on the propulsive forces generated by a biorobotic fish pectoral fin,” *Journal of Experimental Biology*, vol. 213, no. 23, pp. 4043–4054, 2010.
- [68] T. Y.-T. Wu, “Hydromechanics of swimming propulsion. Part 1. Swimming of a two-dimensional flexible plate at variable forward speeds in an inviscid fluid,” *Journal of Fluid Mechanics*, vol. 46, no. 02, p. 337, 1971.

- [69] R. J. Clapham and H. Hu, “iSplash: realizing fast Carangiform swimming to outperform a real fish,” *Springer Tracts in Mechanical Engineering*, vol. 12, no. Iros, pp. 193–218, 2015.
- [70] R. K. Katzschmann, J. DelPreto, R. MacCurdy, and D. Rus, “Exploration of underwater life with an acoustically controlled soft robotic fish,” *Science Robotics*, vol. 3, no. 16, eaar3449, 2018.
- [71] A. R. Blight, “The muscular control of vertebrate swimming movements,” *Biological Reviews*, vol. 52, no. 2, pp. 181–218, 1977.
- [72] B. E. Flammang and G. V. Lauder, “Speed-dependent intrinsic caudal fin muscle recruitment during steady swimming in bluegill sunfish, *Lepomis macrochirus*,” *Journal of Experimental Biology*, vol. 211, no. 4, pp. 587–598, 2008.
- [73] J. H. Long and K. S. Nipper, “The importance of body stiffness in undulatory propulsion1,” *American Zoologist*, vol. 36, no. 6, pp. 678–694, 1996.
- [74] J. H. Long, B. Adcock, and R. G. Root, “Force transmission via axial tendons in undulating fish: a dynamic analysis,” *Comparative Biochemistry and Physiology Part A: Molecular & Integrative Physiology*, vol. 133, no. 4, pp. 911–929, 2002.
- [75] K. Nguyen, N. Yu, M. M. Bandi, M. Venkadesan, and S. Mandre, “Curvature-induced stiffening of a fish fin,” *Journal of The Royal Society Interface*, vol. 14, no. 130, p. 20170247, 2017.
- [76] J. H. Long, T. J. Koob, K. Irving, K. Combie, V. Engel, N. Livingston, A. Lamert, and J. Schumacher, “Biomimetic evolutionary analysis: testing the adaptive value of vertebrate tail stiffness in autonomous swimming robots,” *Journal of Experimental Biology*, vol. 209, no. 23, pp. 4732–4746, 2006. arXiv: arXiv:1011.1669v3.
- [77] M Nakashima, K Tokuo, K Kaminaga, K Ono, and Others, “Experimental study of a self-propelled two-joint dolphin robot,” in *The Ninth International Offshore and Polar Engineering Conference*, 1999.
- [78] M. Nakabayashi, R. Kobayashi, S. Kobayashi, and H. Morikawa, “Bioinspired propulsion mechanism using a fin with a dynamic variable-effective-length spring: Evaluation of thrust characteristics and flow around a fin in a uniform flow,” *Journal of Biomechanical Science and Engineering*, vol. 4, no. 1, pp. 82–93, 2009.
- [79] M. Ziegler, M. Hoffmann, J. P. Carbajal, and R. Pfeifer, “Varying body stiffness for aquatic locomotion,” *Proceedings - IEEE International Conference on Robotics and Automation*, pp. 2705–2712, 2011.
- [80] A. Jusufi, D. M. Vogt, R. J. Wood, and G. V. Lauder, “Undulatory Swimming Performance and Body Stiffness Modulation in a Soft Robotic Fish-Inspired Physical Model,” *Soft robotics*, vol. 4, no. 3, pp. 202–210, 2017.
- [81] Y. J. Park, T. M. Huh, D. Park, and K. J. Cho, “Design of a variable-stiffness flapping mechanism for maximizing the thrust of a bio-inspired underwater robot,” *Bioinspiration and Biomimetics*, vol. 9, no. 3, 2014.

- [82] S. B. Behbahani and X. Tan, “Design and dynamic modeling of electrorheological fluid-based variable-stiffness fin for robotic fish,” *Smart Materials and Structures*, vol. 26, no. 8, p. 085 014, 2017.
- [83] M. Kurt, J. Cochran-Carney, Q. Zhong, A. Mivehchi, D. B. Quinn, and K. W. Moored, “Swimming freely near the ground leads to flow-mediated equilibrium altitudes,” *Journal of Fluid Mechanics*, vol. 875, R1, 2019.
- [84] F. Ayancik, Q. Zhong, D. B. Quinn, A. Brandes, H. Bart-Smith, and K. W. Moored, “Scaling laws for the propulsive performance of three-dimensional pitching propulsors,” *Journal of Fluid Mechanics*, vol. 871, pp. 1117–1138, 2019. arXiv: 1810.11170.
- [85] E. Blevins and G. V. Lauder, “Swimming near the substrate: A simple robotic model of stingray locomotion,” *Bioinspiration and Biomimetics*, vol. 8, no. 1, p. 016 005, 2013.
- [86] J. Katz, “Calculation of the Aerodynamic Forces on Automotive Lifting Surfaces.,” *Journal of Fluids Engineering, Transactions of the ASME*, vol. 107, no. 4, pp. 438–443, 1985.
- [87] K. W. Moored, “Unsteady three-dimensional boundary element method for self-propelled bio-inspired locomotion,” *Computers and Fluids*, vol. 167, pp. 324–340, 2018.
- [88] R. Krasny, “Desingularization of periodic vortex sheet roll-up,” *Journal of Computational Physics*, vol. 65, no. 2, pp. 292–313, 1986.
- [89] Q. Zhu, M. J. Wolfgang, D. K. Yue, and M. S. Triantafyllou, “Three-dimensional flow structures and vorticity control in fish-like swimming,” *Journal of Fluid Mechanics*, vol. 468, pp. 1–28, 2002.
- [90] A. Mivehchi, Q. Zhang, M. Kurt, D. B. Quinn, and K. W. Moored, “Scaling laws for the propulsive performance of a purely pitching foil in ground effect,” *arXiv preprint arXiv:2011.11792*, 2020.
- [91] X.-m. Shao, D.-y. Pan, J. Deng, and Z.-s. Yu, “Numerical studies on the propulsion and wake structures of finite-span flapping wings with different aspect ratios,” *Journal of Hydrodynamics*, vol. 22, no. 2, pp. 147–154, 2010.
- [92] J. T. King, R. Kumar, and M. A. Green, “Experimental observations of the three-dimensional wake structures and dynamics generated by a rigid, bioinspired pitching panel,” *Physical Review Fluids*, vol. 3, p. 34 701, 2018.
- [93] K. D. Von Ellenrieder, K. Parker, and J. Soria, “Flow structures behind a heaving and pitching finite-span wing,” *Journal of Fluid Mechanics*, vol. 490, p. 129, 2003.
- [94] J. H. Buchholz and A. J. Smits, “The wake structure and thrust performance of a rigid low-aspect-ratio pitching panel,” *Journal of Fluid Mechanics*, vol. 603, pp. 331–365, 2008.
- [95] H. Dong, R. Mittal, and F. M. Najjar, *Wake topology and hydrodynamic performance of low-aspect-ratio flapping foils*. 2006, vol. 566, pp. 309–343, ISBN: 0022112006.

- [96] K. V. Rozhdestvensky, “Wing-in-ground effect vehicles,” *Progress in Aerospace Sciences*, vol. 42, no. 3, pp. 211–283, 2006.
- [97] V Raspa, S Ramanarivo, B Thiria, and R Godoy-Diana, “Vortex-induced drag and the role of aspect ratio in undulatory swimmers,” *Physics of Fluids*, vol. 26, no. 4, p. 041 701, 2014.
- [98] C. Brennen, “A review of added mass and fluid inertial forces.,” 1982.
- [99] L. Prandtl, “Theory of lifting surfaces,” 1920.
- [100] K. Yano, F. Sato, and T. Takahashi, “Observations of mating behavior of the manta ray, *manta birostris*, at the ogasawara islands, japan,” *Ichthyological Research*, vol. 46, no. 3, pp. 289–296, 1999.
- [101] M. M. KOOCHEFAHANI, “Vortical patterns in the wake of an oscillating airfoil,” *AIAA Journal*, vol. 27, no. 9, pp. 1200–1205, 1989. arXiv: arXiv:1011.1669v3.
- [102] D. J. Cleaver, Z. Wang, and I. Gursul, “Bifurcating flows of plunging aerofoils at high Strouhal numbers,” *Journal of Fluid Mechanics*, vol. 708, pp. 349–376, 2012.
- [103] C. Liang, K. Ou, S. Premasathan, A. Jameson, and Z. J. Wang, “High-order accurate simulations of unsteady flow past plunging and pitching airfoils,” *Computers and Fluids*, vol. 40, no. 1, pp. 236–248, 2011.
- [104] V. Mwaffo, P. Zhang, S. R. Cruz, and M. Porfiri, “Zebrafish swimming in the flow: A particle image velocimetry study,” *PeerJ*, vol. 2017, no. 11, e4041, 2017.
- [105] I. E. Garrick, “Propulsion of a flapping and oscillating airfoil,” *Report National Advisory Committee for Aeronautics, NACA Report*, no. 567, pp. 419–427, 1936.
- [106] R. Mason and J. W. Burdick, “Experiments in Carangiform Robotic Fish Locomotion,” Tech. Rep., 2000.
- [107] R. Thandiackal and G. V. Lauder, “How zebrafish turn: analysis of pressure force dynamics and mechanical work,” *The Journal of experimental biology*, vol. 223, no. 16, 2020.
- [108] A. T. Bode-Oke, S. Zeyghami, and H. Dong, “Aerodynamics and flow features of a damselfly in takeoff flight,” *Bioinspiration & biomimetics*, vol. 12, no. 5, p. 056 006, 2017.
- [109] K. Nashimoto, “The Swimming Speed of Fish in Relation to Fish Size and Frequency of Tail Beating,” *NIPPON SUISAN GAKKAISHI*, vol. 46, no. 3, pp. 307–312, 1980.
- [110] F. E. Rohr, J. J., Fish, “Strouhal numbers and optimization of swimming by odontocete cetaceans,” *Journal of Experimental Biology*, vol. 207, no. 10, pp. 1633–1642, 2004. arXiv: arXiv:1011.1669v3.
- [111] R. Fernández-Prats, V. Raspa, B. Thiria, F. Huera-Huarte, and R. Godoy-Diana, “Large-amplitude undulatory swimming near a wall,” *Bioinspiration & biomimetics*, vol. 10, no. 1, p. 016 003, 2015.

- [112] S. Zeyghami, Q. Zhong, G. Liu, and H. Dong, “Passive pitching of a flapping wing in turning flight,” *AIAA Journal*, pp. 1–9, 2018.
- [113] Q. Zhong, G. Liu, Y. Ren, and H. Dong, “On the passive pitching mechanism in turning flapping flights using a torsional spring model,” in *47th AIAA Fluid Dynamics Conference*, 2017, p. 3817.
- [114] R. Bainbridge, “The speed of swimming of fish as related to size and to the frequency and amplitude of the tail beat,” *Journal of experimental biology*, vol. 35, no. 1, pp. 109–133, 1958.
- [115] J. D. Eldredge and A. R. Jones, “Leading-edge vortices: Mechanics and modeling,” *Annual Review of Fluid Mechanics*, vol. 51, pp. 75–104, 2019.
- [116] I. Borazjani and F. Sotiropoulos, “On the role of form and kinematics on the hydrodynamics of self-propelled body/caudal fin swimming,” *Journal of Experimental Biology*, vol. 213, no. 1, pp. 89–107, 2010.
- [117] S. G. Reznick and J. Flores, “Strake-generated vortex interactions for a fighter-like configuration,” *Journal of Aircraft*, vol. 26, no. 4, pp. 289–294, 1989.
- [118] I. Borazjani and M. Daghooghi, “The fish tail motion forms an attached leading edge vortex,” *Proceedings of the Royal Society B: Biological Sciences*, vol. 280, no. 1756, p. 20 122 071, 2013.
- [119] P. Mancini, F. Manar, K. Granlund, M. V. Ol, and A. R. Jones, “Unsteady aerodynamic characteristics of a translating rigid wing at low reynolds number,” *Physics of Fluids*, vol. 27, no. 12, p. 123 102, 2015.
- [120] F. Manar, P. Mancini, D. Mayo, and A. R. Jones, “Comparison of rotating and translating wings: Force production and vortex characteristics,” *AIAA Journal*, vol. 54, no. 2, pp. 519–530, 2015.
- [121] D. Lentink and M. H. Dickinson, “Rotational accelerations stabilize leading edge vortices on revolving fly wings,” *Journal of Experimental Biology*, vol. 212, no. 16, pp. 2705–2719, 2009.
- [122] D. Garmann and M. Visbal, “Dynamics of revolving wings for various aspect ratios,” *Journal of Fluid Mechanics*, vol. 748, pp. 932–956, 2014.
- [123] T. Jardin, “Coriolis effect and the attachment of the leading edge vortex,” *Journal of Fluid Mechanics*, vol. 820, pp. 312–340, 2017.
- [124] G. Shah, “Wind tunnel investigation of aerodynamic and tail buffet characteristics of leading-edge extension modifications to the f/a-18,” in *18th Atmospheric Flight Mechanics Conference*, 1991, p. 2889.
- [125] M. Daghooghi and I. Borazjani, “The hydrodynamic advantages of synchronized swimming in a rectangular pattern,” *Bioinspiration & biomimetics*, vol. 10, no. 5, p. 056 018, 2015.
- [126] J. C. Nauen and G. V. Lauder, “Hydrodynamics of caudal fin locomotion by chub mackerel, scomber japonicus (scombridae),” *Journal of Experimental Biology*, vol. 205, no. 12, pp. 1709–1724, 2002.

- [127] J. J. Magnuson, “Hydrostatic equilibrium of euthynnus affinis, a pelagic teleost without a gas bladder,” *Copeia*, pp. 56–85, 1970.
- [128] I. Aleev, “Function and gross morphology in fish,” *Function and gross morphology in fish*, 1969.
- [129] V. Walters, “Body form and swimming performance in the scombroid fishes,” *American Zoologist*, pp. 143–149, 1962.
- [130] C. Lindsey, “Form, function and locomotory habits in fish,” *Locomotion*, 1978.
- [131] F. Fish and G. Lauder, “PASSIVE AND ACTIVE FLOW CONTROL BY SWIMMING FISHES AND MAMMALS,” *Annual Review of Fluid Mechanics*, vol. 38, no. 1, pp. 193–224, 2006.
- [132] Q. Zhong, H. Dong, and D. B. Quinn, “How dorsal fin sharpness affects swimming speed and economy,” *Journal of Fluid Mechanics*, vol. 878, pp. 370–385, 2019.
- [133] G. Liu, Y. Ren, H. Dong, O. Akanyeti, J. C. Liao, and G. V. Lauder, “Computational analysis of vortex dynamics and performance enhancement due to body–fin and fin–fin interactions in fish-like locomotion,” *Journal of Fluid Mechanics*, vol. 829, pp. 65–88, 2017.
- [134] W. Weaver Jr, S. P. Timoshenko, and D. H. Young, *Vibration problems in engineering*. John Wiley & Sons, 1990.
- [135] R. E. Shadwick, H. S. Rapoport, and J. M. Fenger, “Structure and function of tuna tail tendons,” *Comparative Biochemistry and Physiology - A Molecular and Integrative Physiology*, vol. 133, no. 4, pp. 1109–1125, 2002.
- [136] M. H. Dickinson, C. T. Farley, R. J. Full, M. A. R. Koehl, R. Kram, and S. Lehman, “How animals move: an integrative view,” *science*, vol. 288, no. 5463, pp. 100–106, 2000.
- [137] D. A. Pabst, “Springs in swimming animals,” *American Zoologist*, vol. 36, no. 6, pp. 723–735, 1996.
- [138] M. J. Lighthill, “Aquatic animal propulsion of high hydromechanical efficiency,” *Journal of Fluid Mechanics*, vol. 44, no. 02, p. 265, 1970.
- [139] L. I. Sedov, *Similarity and dimensional methods in mechanics*. CRC press, 1993.
- [140] E. D. Tytell, M. C. Leftwich, C.-Y. Hsu, B. E. Griffith, A. H. Cohen, A. J. Smits, C. Hamlet, and L. J. Fauci, “Role of body stiffness in undulatory swimming: insights from robotic and computational models,” *Physical Review Fluids*, vol. 1, no. 7, p. 73 202, 2016.
- [141] T. Van Buren, D. Floryan, and A. J. Smits, “Scaling and Performance of Simultaneously Heaving and Pitching Foils,” *AIAA Journal*, vol. 57, no. 9, pp. 3666–3677, 2019.
- [142] D. B. Quinn, G. V. Lauder, and A. J. Smits, “Maximizing the efficiency of a flexible propulsor using experimental optimization,” *J. Fluid Mech*, vol. 767, pp. 430–448, 2015.

- [143] J. D. Eldredge and A. R. Jones, “Leading-Edge Vortices : Mechanics and Modeling,” no. August 2018, pp. 75–104, 2019.
- [144] I. Borazjani and M. Daghooghi, “The fish tail motion forms an attached leading edge vortex,” 2013.
- [145] G. C. Lewin and H. Haj-Hariri, “Modelling thrust generation of a two-dimensional heaving airfoil in a viscous flow,” *Journal of Fluid Mechanics*, vol. 492, pp. 339–362, 2003.
- [146] Z. J. WANG, “Vortex shedding and frequency selection in flapping flight,” *Journal of Fluid Mechanics*, vol. 410, S0022112099008071, 2000.
- [147] Long, Mchenry, and Boetticher, “Undulatory Swimming: How Traveling Waves Are Produced and Modulated in Sunfish (*Lepomis Gibbosus*),” *The Journal of experimental biology*, vol. 192, no. 1, pp. 129–45, 1994.
- [148] J. M. Blank, C. J. Farwell, J. M. Morrisette, R. J. Schallert, and B. A. Block, “Influence of Swimming Speed on Metabolic Rates of Juvenile Pacific Bluefin Tuna and Yellowfin Tuna,” Tech. Rep. 2, 2007, pp. 167–177.
- [149] J. R. Hunter, “Sustained speed of jack mackerel, *Trachurus symmetricus*,” *Fishery Bulletin*, vol. 69, no. 2, pp. 267–271, 1971.
- [150] V. Di Santo, E. L. Blevins, and G. V. Lauder, “Batoid locomotion: Effects of speed on pectoral fin deformation in the little skate, *Leucoraja erinacea*,” *Journal of Experimental Biology*, vol. 220, no. 4, pp. 705–712, 2017.
- [151] R. E. Shadwick and S. Gemballa, “Structure, Kinematics, And Muscle Dynamics In Undulatory Swimming,” *Fish Physiology*, vol. 23, no. C, pp. 241–280, 2005.
- [152] B. E. Flammang, “Functional morphology of the radialis muscle in shark tails,” *Journal of Morphology*, vol. 271, no. 3, pp. 340–352, 2010.
- [153] K. N. Lucas, N. Johnson, W. T. Beaulieu, E. Cathcart, G. Tirrell, S. P. Colin, B. J. Gemmell, J. O. Dabiri, and J. H. Costello, “Bending rules for animal propulsion,” *Nature Communications*, 2014.
- [154] T. A. McMahon, *Muscles, reflexes, and locomotion*. Princeton University Press, 1984.
- [155] Y. Cai, S. Bi, and L. Zheng, “Design optimization of a bionic fish with multi-joint fin rays,” *Advanced Robotics*, vol. 26, no. 1-2, pp. 177–196, 2012.
- [156] V. R. Challa, M. G. Prasad, Y. Shi, and F. T. Fisher, “A vibration energy harvesting device with bidirectional resonance frequency tunability,” *Smart Materials and Structures*, vol. 17, no. 1, 2008.
- [157] T. W. Secord and M. C. Audi, “A Tunable Resonance Cantilever for Cardiac Energy Harvesting,” *Cardiovascular Engineering and Technology*, vol. 10, no. 2, pp. 380–393, 2019.
- [158] Y. Zhu, Y. Su, and K. Breuer, “Nonlinear flow-induced instability of an elastically mounted pitching wing,” *Journal of Fluid Mechanics*, vol. 899, 2020.

- [159] K. Shoele and R. Mittal, “Energy harvesting by flow-induced flutter in a simple model of an inverted piezoelectric flag,” *Journal of Fluid Mechanics*, vol. 790, pp. 582–606, 2016.
- [160] S. Friedman, S. Price, K. Corn, O Larouche, C. Martinez, and P. Wainwright, “Body shape diversification along the benthic–pelagic axis in marine fishes,” *Proceedings of the Royal Society B*, vol. 287, no. 1931, p. 20 201 053, 2020.
- [161] J. Tavera, A. Acero, and P. C. Wainwright, “Multilocus phylogeny, divergence times, and a major role for the benthic-to-pelagic axis in the diversification of grunts (haemulidae),” *Molecular Phylogenetics and Evolution*, vol. 121, pp. 212–223, 2018.
- [162] B. W. Robinson and D. S. Wilson, “Character release and displacement in fishes: A neglected literature,” *The American Naturalist*, vol. 144, no. 4, pp. 596–627, 1994.
- [163] A. Filella, F. Nadal, C. Sire, E. Kanso, and C. Eloy, “Model of collective fish behavior with hydrodynamic interactions,” *Physical review letters*, vol. 120, no. 19, p. 198 101, 2018.
- [164] P. W. Webb, “Control of posture, depth, and swimming trajectories of fishes,” *Integrative and Comparative Biology*, vol. 42, no. 1, pp. 94–101, 2002.
- [165] P. B. Moyle and J. J. Cech, *Fishes: An Introduction to Ichthyology*, 597 MOY. 2004.
- [166] F. M. White and I. Corfield, *Viscous fluid flow*. McGraw-Hill New York, 2006, vol. 3.
- [167] R. Iglisch, “Exact calculation of laminar boundary layer in longitudinal flow over a flat plate with homogeneous suction,” 1949.
- [168] P. K. Rudolph, “High-lift systems on commercial subsonic airliners,” 1996.
- [169] A. Smith, “High-lift aerodynamics,” *Journal of Aircraft*, vol. 12, no. 6, pp. 501–530, 1975.
- [170] P. A. Dewey, B. M. Boschitsch, K. W. Moored, H. A. Stone, and A. J. Smits, “Scaling laws for the thrust production of flexible pitching panels,” *Journal of Fluid Mechanics*, vol. 732, pp. 29–46, 2013.
- [171] X. Lin, J. Wu, T. Zhang, and L. Yang, “Flow-mediated organization of two freely flapping swimmers,” *Journal of Fluid Mechanics*, vol. 912, 2021.
- [172] J. Wang, D. K. Wainwright, R. E. Lindengren, G. V. Lauder, and H. Dong, “Tuna locomotion: A computational hydrodynamic analysis of finlet function,” *Journal of the Royal Society Interface*, vol. 17, no. 165, p. 20 190 590, 2020.

# Appendix A

## Supplemental Data and figure of Multi-fin Interaction

### A.1 Dorsal fin stiffness scaling

Based on linear beam theory, dorsal fin deflection under a uniform load should be approximately  $\gamma h^3 / (6EI)$ , where  $\gamma$  is force per length on the fin,  $h$  is fin height,  $E$  is fin's elastic modulus ( $\approx 2$  GPa for ABS), and  $I$  is the area moment of inertia of the fin's cross section ( $ld^3/12$  for a rectangular cross section, where  $l$  is fin length and  $d$  is fin thickness). We can estimate the worst-case deflection using the highest lateral instantaneous force we recorded (3.1 N) and the thinnest dorsal fin (147 mm long, 7.6 mm high, and 1 mm thick). If the center of pressure on the model were at the weakest part of the dorsal fin, we would expect the full 3.1 N to be applied over the 35 mm body span at that weakest point (2\*OD in Figure 5.1c), resulting in a deflection of

$$\frac{\gamma h^3}{6EI} = \frac{2\left(\frac{3.1\text{ N}}{35\text{ mm}}\right)(7.6\text{ mm})^3}{(2\text{ GPa})(147\text{ mm})(1\text{ mm})^3} \approx 0.3\text{ mm}$$

Over the majority of trials, we expect much smaller deflections, because the lateral force goes with frequency squared, and the moment of inertia with fin thickness cubed. We also

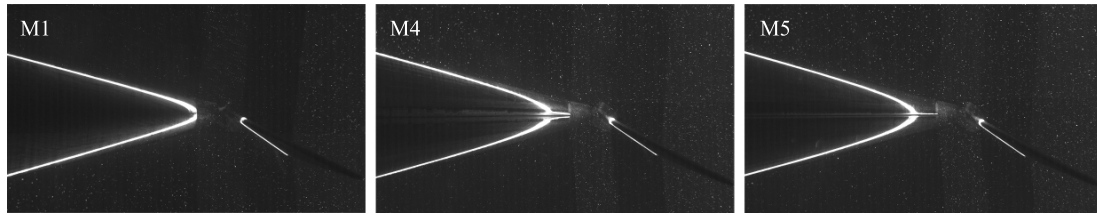


Figure A.1: **Dorsal fin deflection is not measurably different between M1, M4, and M5.** High speed images taken at the same time ( $t = 0.25\tau$ ) and the same frequency ( $f = 1.57$  Hz) show no observable differences in dorsal fin bending.

used a conservative estimate for  $I$  by assuming a rectangular fin, whereas the actual dorsal fin is triangular. Therefore, we don't anticipate measurably different output kinematics for the same excitation, which we verified with high speed camera images (Figure A.1).

## A.2 Supplemental Figures

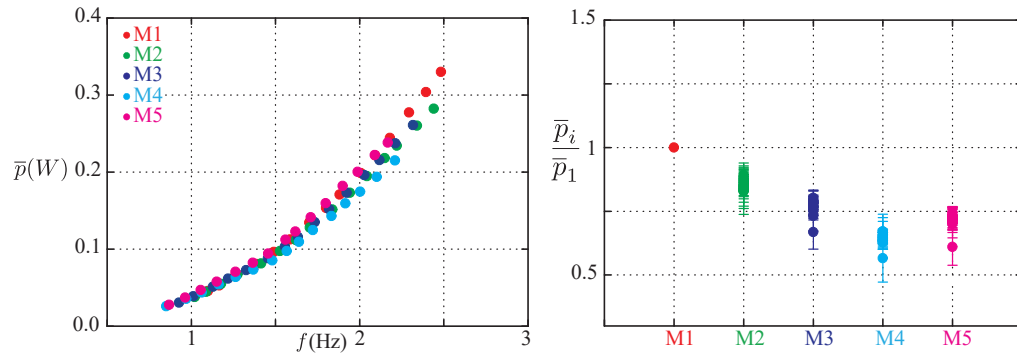


Figure A.2: **For self-propelled swimming, cycle-averaged power consumption decreases with sharpness until M4.** (a) Cycle-averaged power consumption increases with frequency for each model. (b) Compared to M1, cycle-averaged power consumption decreases from M1 to M4, then slightly increases from M4 to M5.

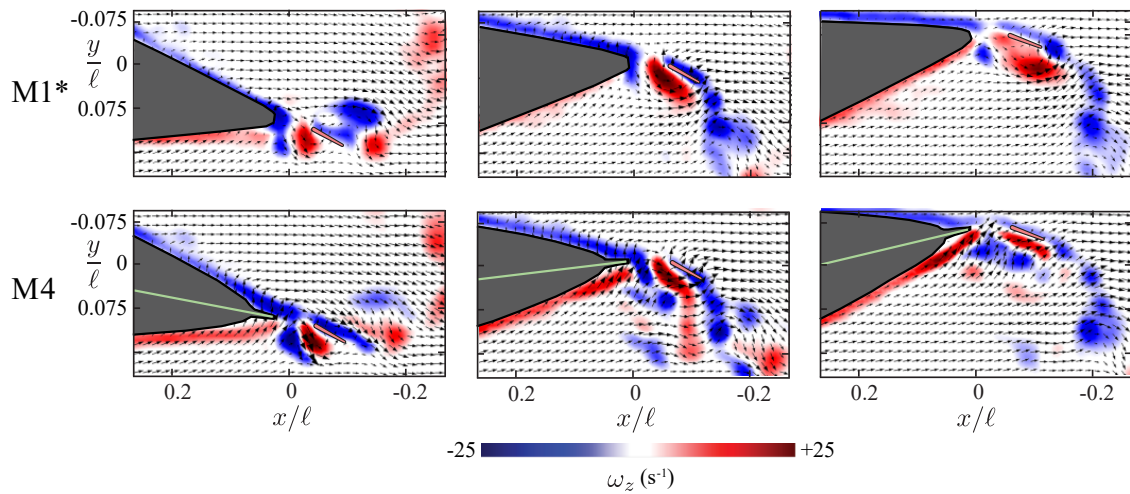


Figure A.3: **PIV around M1\* shows similar wake structures as PIV around M1 (Figure 5.3a,b).**

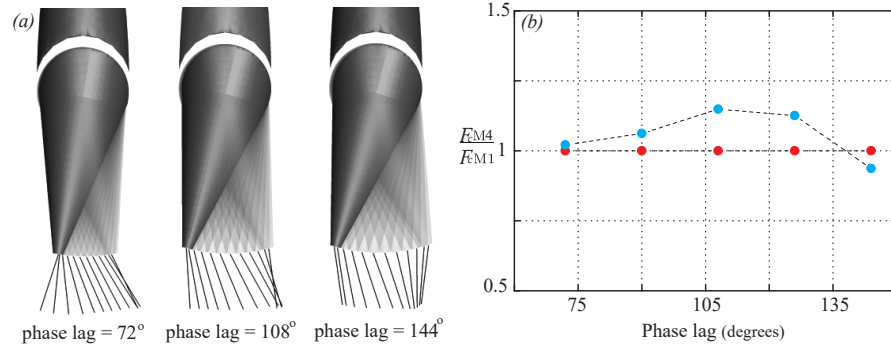


Figure A.4: **Dorsal-caudal fin interaction is phase insensitive.** (a) Top view of half-cycle time-lapsed kinematics of three phase lags considered (72,108,144). (b) The ratio of M4 thrust to M1 thrust ( $\overline{F}_cM4/\overline{F}_cM1$ ) is mostly greater than 1 over the range of phase lags tested. Decreasing the phase from its natural value (126) would require a stiffer tail joint; increasing the phase would require an actively controlled tail joint.

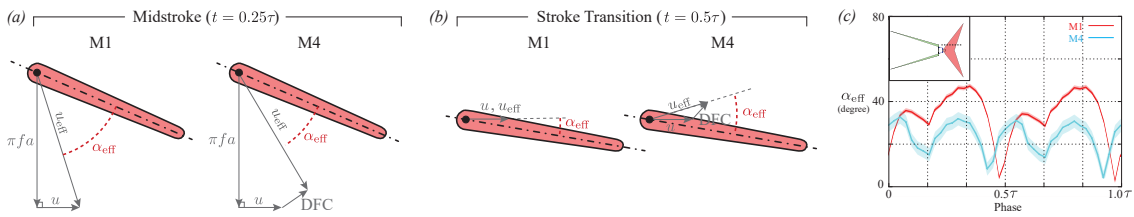


Figure A.5: **The effective angle of attack of the caudal fin is lower in M4 than in M1 for most of the pitching cycle.** (a,b) Dorsal Fin-induced Crossflow (DFC) decreases the effective angle of attack of the caudal fin at the midstroke and increases the effective angle of attack at stroke transition. (c) The effective angle of attack for M1 and M4 is shown through the full pitching cycle. Layer 3 (Figure 5.3b,e) was chosen to approximate the effective angle of attack of the caudal fin. The average speed of crossflow was computed based on Region 1 (Figure 5.3b,e) translated with the body. Angle uncertainty was estimated based on variability in the PIV vectors of Region 1. The geometric angle of attack was calculated using high speed video. Effective angle of attack was calculated as the angle of the effective incoming flow velocity ( $u_{eff}$ ), which was calculated using vector addition as follows. (a). M1 midstroke:  $\alpha_{eff} = \tan^{-1}(\pi fa)/u - (25 \pm 2) = 41 \pm 2$ . M4 midstroke:  $\alpha_{eff} = \tan^{-1}((\pi fa - (0.63 \pm 0.08)fa \sin(55 \pm 5))/(u + (0.63 \pm 0.08)fa \cos(55 \pm 5))) - (25 \pm 2) = 32 \pm 4$ . (b). M1 at stroke transition:  $\alpha_{eff} = 12 \pm 2$ . M4 at stroke transition:  $\alpha_{eff} = \tan^{-1}((0.6 \pm 0.07)fa \sin(56 \pm 4)/(u + (0.6 \pm 0.07)fa \cos(56 \pm 4))) + (12 \pm 2) = 28 \pm 4$ .

## Appendix B

# Supplemental Data and figure of Real-time Adjustable Flexibility

Table B.1: Tuna stiffness test specifications

	Tail 1	Tail 2	Tail 3	Tail 4	Tail 5	Tail 6
$T_M(\text{N})$	0~29.4	0~29.4	0~29.4	0~29.4	0~29.4	0~29.4
$F_C(\text{N})$	0~7.8	0~10.6	0~10.6	0~3.9	0~3.9	0~3.9
$\bar{\ell}_F(\text{mm})$	25	27	16	22	19.5	13.5
Span(mm)	50	52	32	21	24.6	27.2

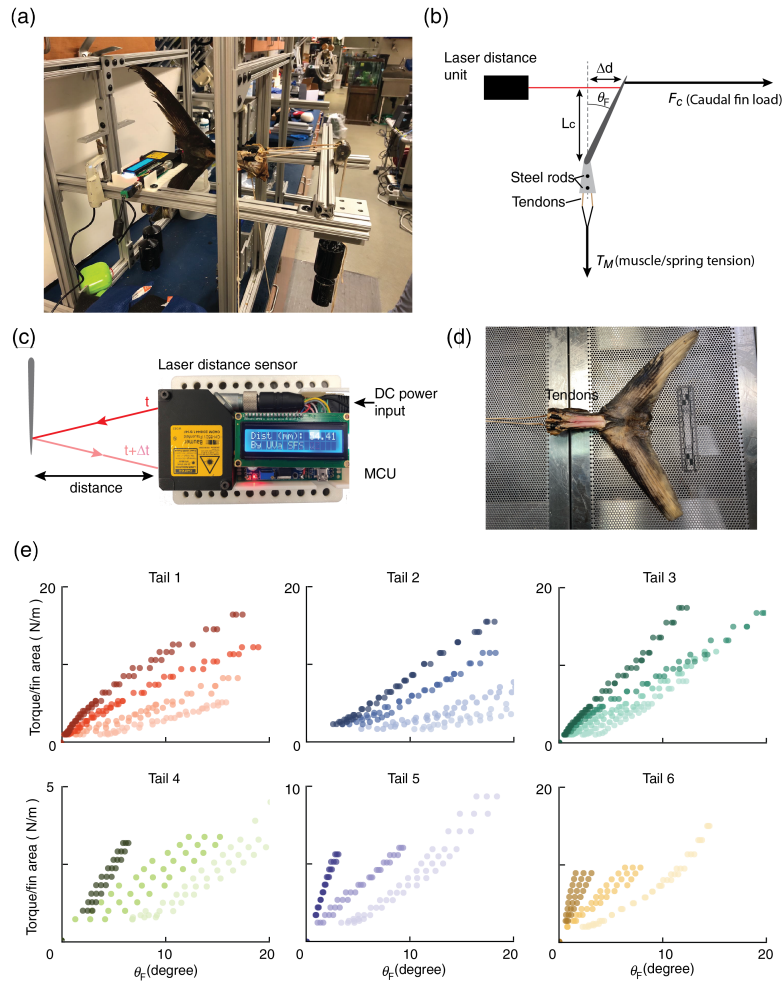


Figure B.1: **Tuna tail joint stiffness measurement.**(a) Tuna tails were installed on the test rig. Two sets of weights applied the force on the tendons ( $T_M$ ) and the simulated tail fin load ( $F_C$ ). (b) A laser distance sensor measured the deflection ( $d$ ) of the tail fin under various loads. (c) The custom laser distance unit consisted of a laser distance sensor (Baumer CH-8501 OADM 20L6441/S14F), an onboard Micro Controller Unit (MCU), a DC power input, and a LED display. (d) The peduncle area of the tuna tails was dissected to expose the axial tendons on which loads were applied. (e) Six different tails showed similar trend: the applied torque / area and the pitch angle showed a monotonic relation, and the slope of the relation increased with increasing tendon tension. See Tab. S1 for details.

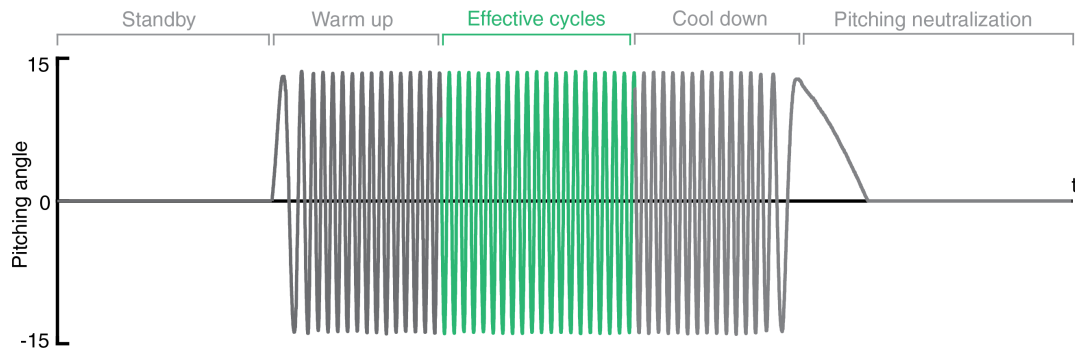


Figure B.2: **Test trial structure.** Each test trial consists of five procedures: 10 s of standby, 5 s of warm-up cycles, 20 cycles of data acquisition, 5 of cool down cycles, then a slow return to the neutral pitching position.

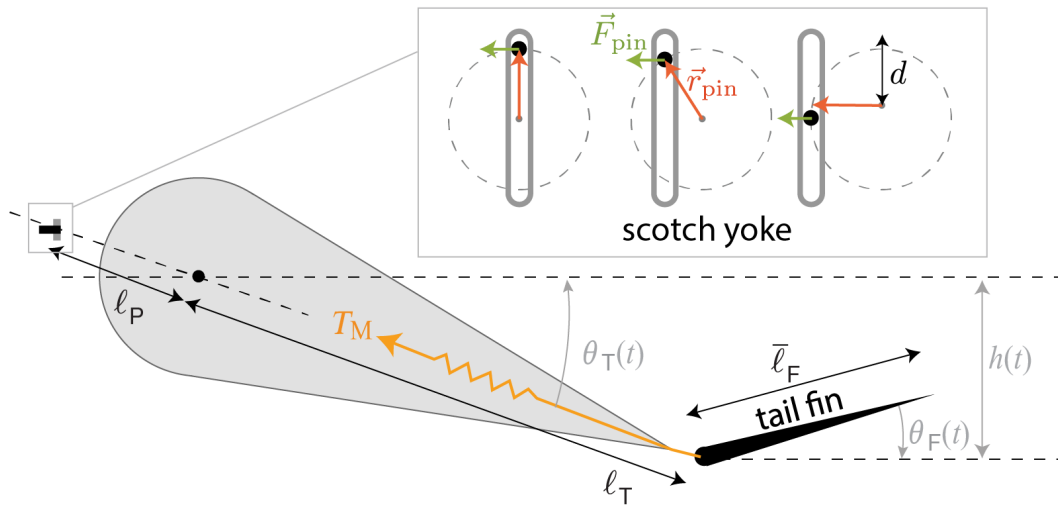


Figure B.3: **Test trial structure.** Variable definitions for estimating power delivered by the scotch yoke mechanism.

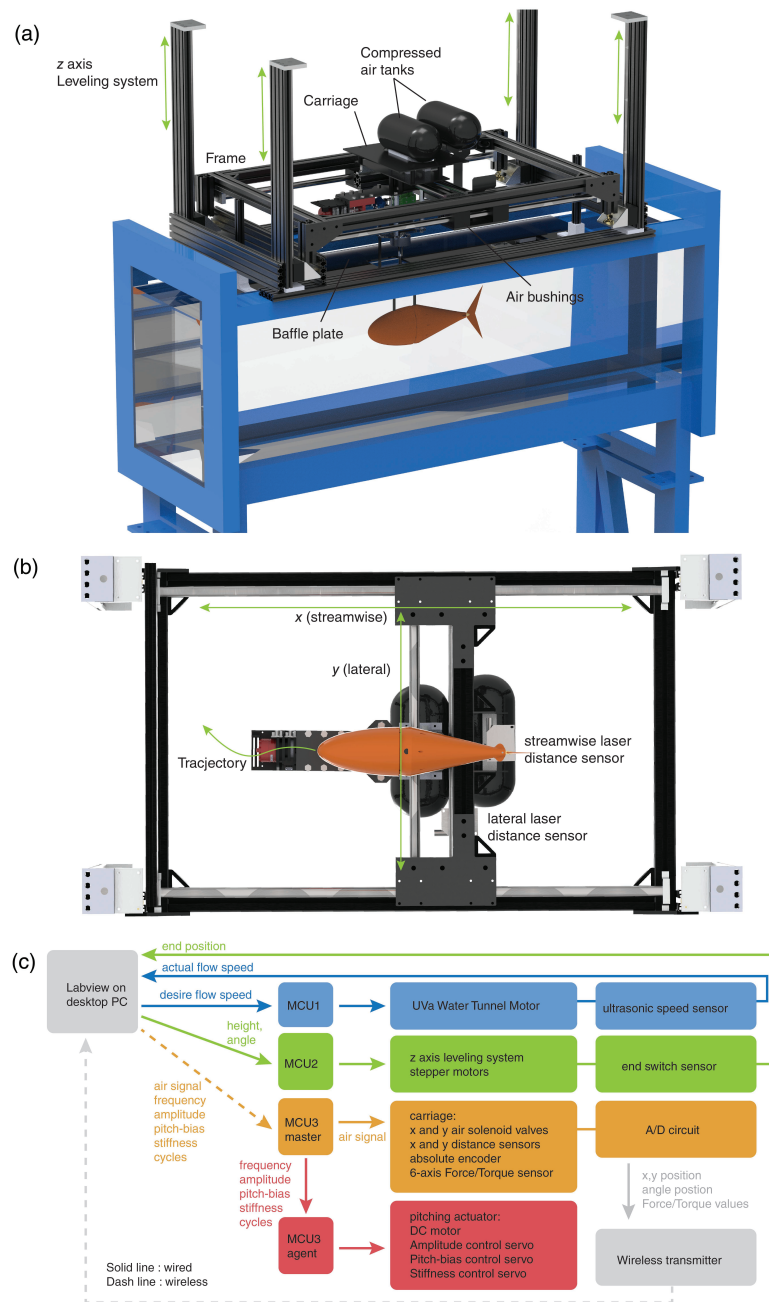


Figure B.4: **Overview of the experimental rig and system layout** (a) Our water channel rig consists of a pitching actuator, inner carriage, an outer frame, and a z-axis leveling system. The pitching actuator (Figure.2.3) is installed on the bottom of the inner carriage, which rides on a two-axis air-bushing system supporting by the outer frame. A baffle plate on the water surface minimizes water waves. (b) Air bushings allow the inner carriage to float in a horizontal plane. The x (streamwise) and y (lateral) position of the inner carriage were recorded by laser distance sensors. (c) System layout. The dashed line means wireless communication and the solid line means wired communication.

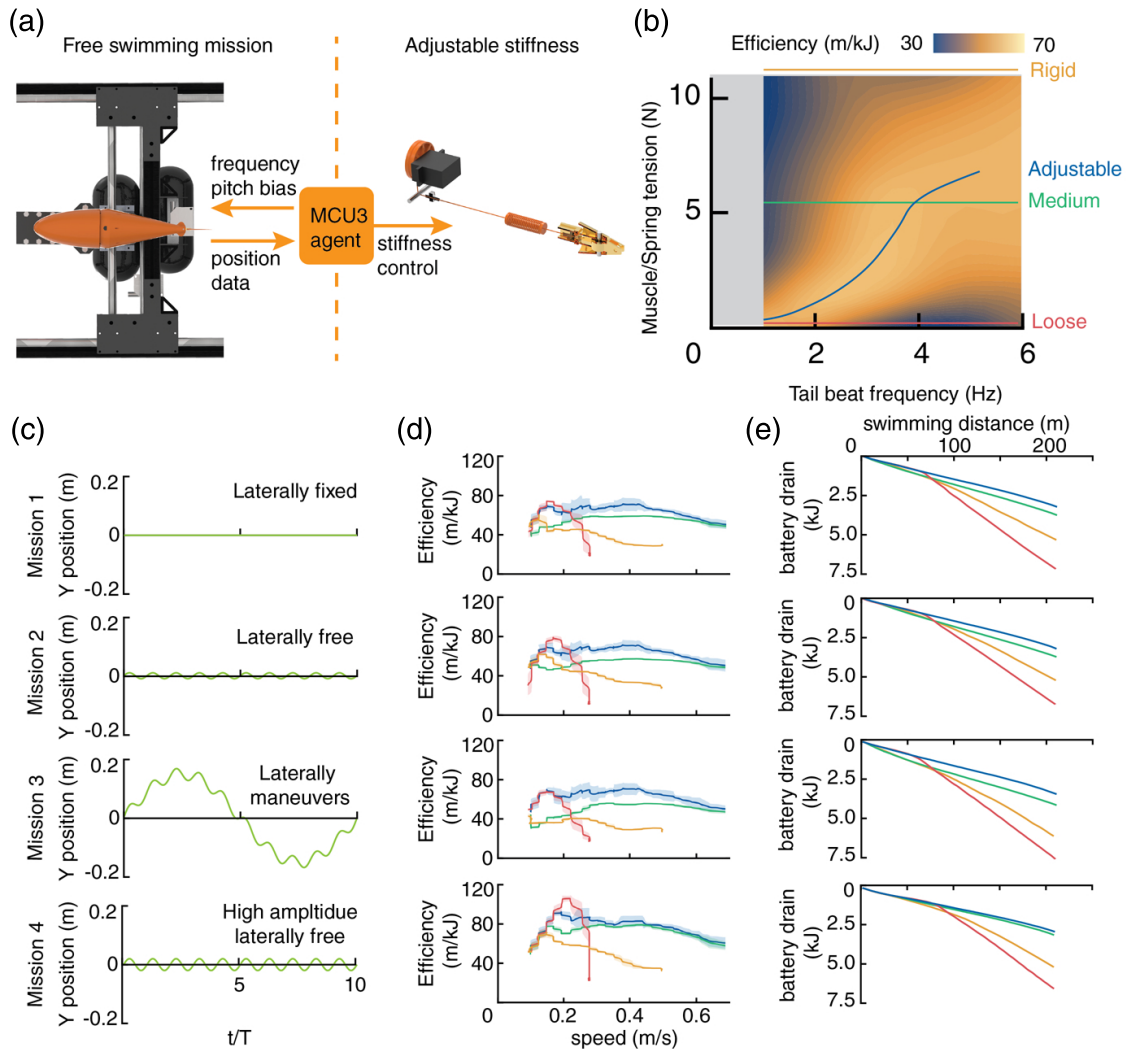


Figure B.5: **Variable-speed untethered missions.** (a) A microcontroller (MCU3) tuned tail stiffness and maintained speed by modulating frequency with a PD controller. (b) Stiffness was either tuned based on frequency (following the blue curve) or fixed at “low”, “medium”, and “high” values. (c) Speed profiles during the Missions. The low and medium stiffness cases are unable to reach the maximum speed (d) Partial trajectories of the lateral position versus pitching cycles for the four Missions. (e) Efficiency versus swimming speed for the four Missions and four stiffness cases. In general, tuning stiffness led to the highest efficiency. The differences became smaller when the amplitude was increased in mission 4. (f) Simulated battery drain versus swimming distance.

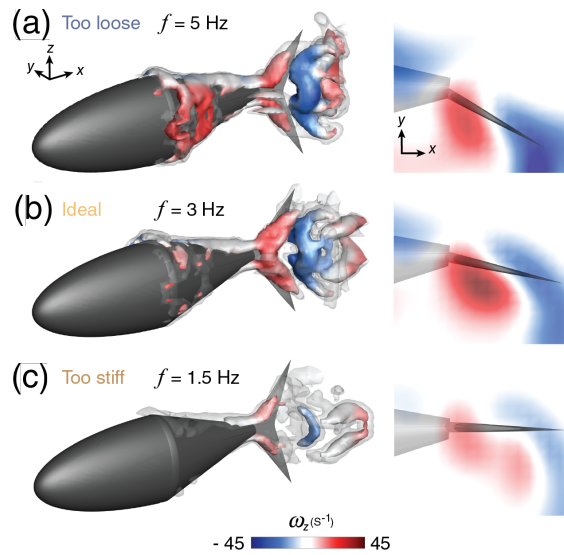


Figure B.6: **Wake structures at low frequencies.** Stiffness value remains constant while the frequency decreases from A to C. (a) Too loose case at high frequency ( $f = 5.0$  Hz). (b) Ideal stiffness at low frequency ( $f = 3$  Hz) leads to similar wake structure to ideal case at high frequency in Figure. 6.5 (c) Too stiff case at low frequency ( $f = 1.5$  Hz).

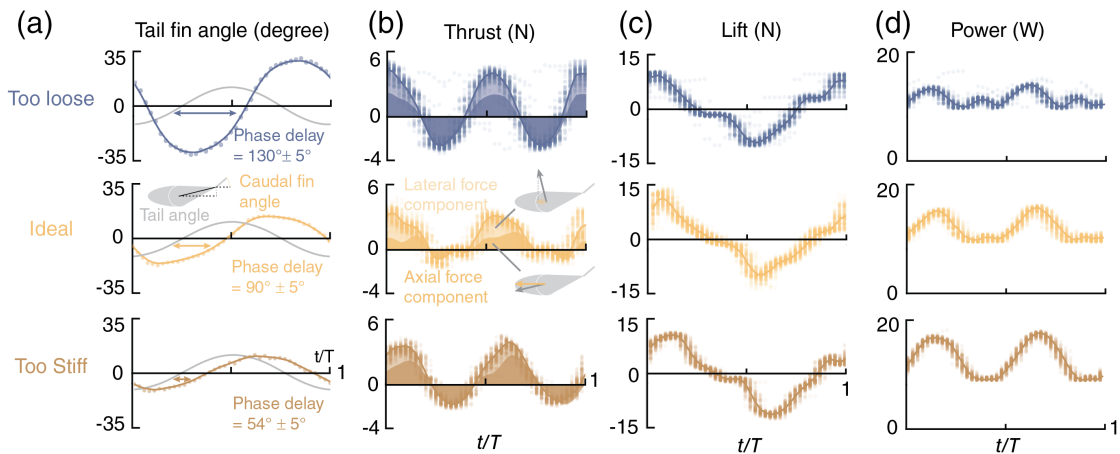


Figure B.7: **Measured force and power of PIV cases at high frequency.** (a) Ideal stiffness results in favorable phase offset ( $90^\circ \pm 5^\circ$ ), while sufficient stiffness increases phase offset and over stiffness decreases offset. (b) Thrust changes were mainly dominated by axial force component, while suitable phase offset minimized the drag (negative thrust). (c) The magnitude of lift force stays at similar scale, but the phase of lift peak delays as stiffness increases. (d) The magnitude of power increases as stiffness increases.

Table B.2: Avatar definitions from Fig. 5

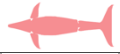
Avatar	Name / Species	Length (cm)	Max Tail-beat Frequency (Hz)	Speed (cm/s)	Strouhal Number	Stride Length	Cost of transport (J/m)	Source
	Dace <i>Leuciscus leuciscu</i>	24.0	14.5	161	N/A	0.37 - 0.83	N/A	Bainbridge, R. (1958) (32)
	Trout <i>Salmo irideus</i>	29.3	15.3	276.1	N/A	0.27 - 0.75	N/A	
	Sea Bass <i>D. labrax</i>	30.5	3.7	71.1	N/A	0.38 - 0.65	N/A	Herskin, J., & Steffensen, J. F. (1998) (68)
	Saithe <i>P. virens</i>	34.6	3.8	86.5	N/A	0.5 - 0.83	0.74 - 1.96	Steinhausen, M. F., Steffensen, J. F., & Andersen, N. G. (2005) (69)
	Whiting <i>Merlangius merlangus</i>	30.5	2.86	53.4	N/A	0.2 - 0.62	0.36 - 1	
	Yellow Fin Tuna <i>Thunnus albacares</i>	51.8	13.1	520.5	N/A	0.5 - 0.21	N/A	Heeny S.H. Yuen (1966) (70)
	Green Jack <i>Caranx caballus</i>	20	5.5	95	N/A	0.35 - 1	N/A	Dickson, K. A., Donley, J. M., Hansen, M. W., & Peters, J. A. (2012) (71)
	Cichlids <i>Cichla ocellaris</i>	10	3.6	29	N/A	0.42 - 1.05	N/A	Feilich, K. L. (2017) (72)
		40	2	32	N/A	0.4	N/A	Yu, J., Tan, M., Wang, S., & Chen, E. (2004) (73)
	Essex G9 robotic fish	52	1.3	53	0.79	0.77	N/A	Liu, J., & Hu, H. (2010) (74)
		72	4.65	205	N/A	0.61	45.6	Yu, J., Su, Z., Wu, Z., & Tan, M. (2016) (24)
	iSplash-II	32	20	370	0.68	0.58	32.4	Clapham, R. J., & Hu, H. (2015) (11)
		15	2.5	10	N/A	0.26	N/A	Kopman, V., Laut, J., Acquaviva, F., Rizzo, A., & Porfiri, M. (2014) (61)
	SoFi	47	1.4	23.5	N/A	0.35	N/A	Katzschmann, R. K., Del-Preto, J., MacCurdy, R., & Rus, D. (2018) (10)
		34.5	16	58	0.2 - 0.41	0.2	110	Fujiwara, S., & Yamaguchi, S. (2017) (62)
		55.5	1.5	36.5	1.5	0.66	N/A	Zhong, Y., Li, Z., & Du, R. (2013) (63)
		15	3	3.75	1.5	0.03	N/A	Shintake, J., Cacucciolo, V., Shea, H., & Floreano, D. (2018) (64)
		41	5.5	85	0.39 - 0.65	0.375	N/A	S. C. van den Berg. (2019) (67)
	UC-Ika 1	66	1.5	29	0.72	0.29	N/A	Farideddin Masoomi, S., Gutschmidt, S., Chen, X., & Sellier, M. (2015) (65)
		37	9	115	0.47	0.33	N/A	Yu, J., Zhang, C., & Liu, L. (2016) (66)
	UVATunabot	25.5	14	100	0.4 - 1.1	0.14 - 0.32	4.4 - 9	Zhu, J., White, C., Wainwright, D. K., Di Santo, V., Lauder, G. V., & Bart-Smith, H. (2019) (9)
	Current-study	35	6	70	0.48 - 1.56	0.13 - 0.42	14.2 - 33.3	

Table B.3: Stiffness values used in Fig.3, Fig.4 and Fig.5

Fig.	Test device	Test name	Mechanism	Freq.	Stiffness cases			
Fig. 3	Tuna-inspired Platform	Tethered kinematics/flow analysis	Tendon-Inspired actuator	5hz	“Too soft”: $T_M = 1.6 \text{ N}$	“Ideal”: $T_M = 5.3 \text{ N}$	“Too stiff”: $T_M = 10.6 \text{ N}$	
Fig. 4	Tuna-inspired Platform	Untethered multi-speed missions	Tendon-Inspired actuator	Var.	“Loose”: $T_M \approx 0 \text{ N}$	“Medium”: $T_M = 5.5 \text{ N}$	“Rigid”: Fixed	“Tunable”
Fig. 5	Tunabot	Autonomous swimming	Leaf Spring	Var.	$EI = 2.3 \times 10^{-4} \text{ N m}^2$	$EI = 1.0 \times 10^{-3} \text{ N m}^2$	$EI = 4.3 \times 10^{-3} \text{ N m}^2$	$EI = 1.4 \times 10^{-2} \text{ N m}^2$